Diffusion MRI tractography branched out

Document Version:
Publisher's PDF, also known as Version of Record (includes final page, issue and volume numbers)

Please check the document version of this publication:

• A submitted manuscript is the version of the article upon submission and before peer-review. There can be
important differences between the submitted version and the official published version of record. People
interested in the research are advised to contact the author for the final version of the publication, or visit the
DOI to the publisher's website.
• The final author version and the galley proof are versions of the publication after peer review.
• The final published version features the final layout of the paper including the volume, issue and page
numbers.

[Link to publication](#)

Diffusion MRI tractography branched out

Andrey Zhylka

Diffusion MRI tractography branched out

PROEFSCHRIFT

ter verkrijging van de graad van doctor aan de Technische Universiteit Eindhoven, op gezag van de rector magnificus prof.dr. S.K. Lenaerts, voor een commissie aangewezen door het College voor Promoties in het openbaar te verdedigen op vrijdag 8 september 2023 om 11.00 uur

door

Andrey Zhylka

geboren te Minsk, Belarus

Dit proefschrift is goedgekeurd door de promotoren en de samenstelling van de promotiecommissie is als volgt:

Voorzitter:	prof.dr. M. Merkx
Promotoren:	prof.dr. J.P.W. Pluim
	prof.dr.ir. M. Breeuwer
Copromotor:	dr. A. De Luca (UMC Utrecht)
Leden:	dr.ir. R. Duits
	prof.dr. P.A.J.M. Boon
	prof.dr. J.P. Thiran (École Polytechnique Fédérale de Lausanne)
Adviseur:	Dr. dr.h.c.mult A.L.G. Leemans (UMC Utrecht)

Contents

Introduction

1.1 Neurosurgery planning and fiber tractography

Neurosurgical intervention is one of the common procedures of brain tumor treatment, particularly for aggressive tumors, such as glioma. In glioma cases, the extent of brain resection plays a crucial role in prolonged survival [1,2]. However, in an attempt to achieve maximum resection, the surgery itself may lead to functional impairment due to unnecessary damage of brain structures surrounding the tumor. Thus, it is of great importance to achieve a balance: removing as much of the tumor as possible while avoiding dramatic quality-of-life degradation.

Achieving the aforementioned balance is one of the goals of neurosurgery planning. At this stage a number of critical decisions has to be made, such as determining the optimal entry point and resection trajectory, minimal safety margins. Furthermore, modern surgical planning includes the virtual dissection of eloquent white matter tracts, brain structures that need to be spared during surgery in order to preserve key brain functions. Patient-specific structural organization of the nerve fiber bundles as well as information on tissue properties that might reflect tumor-induced changes can be obtained using diffusion magnetic resonance imaging (dMRI).

DMRI is a technique based on the motion of water molecules. MRI experiments are performed with different combinations of acquisition parameters. This, in combination with appropriate signal modelling, allows to reconstruct the orientation of white matter tracts in the brain, a process also known as fiber tractography [3]. When this process is combined with anatomical knowledge of the brain or virtual dissection, the resulting fiber tractogram can aid during neurosurgery planning. Tractography allows surgeons and neuroradiologists to perform virtual dissection delineating target fiber bundles. Fiber-pathway reconstruction can also be based on certain regions of interest, such as functional mapping using navigation transcranial magnetic stimulation (nTMS) [4]. Given the knowledge of the nerve locations and certain tissue properties, safety margins around essential healthy fiber bundles can be estimated.

1.2   On to hospitals

Currently, despite the variety of tractography algorithms and diffusion models, clinicians tend to resort to conventional approaches. The most established approach is diffusion tensor imaging (DTI), a method which suffers from limitations that are well-established [5], such as low sensitivity related to inability to resolve complex fiber configurations (e.g., crossing, kissing). Although DTI-based tractography produces results that tend to contain few false-positive fiber pathways [6], it commonly results in incomplete fiber-bundle reconstructions, directly influencing neurosurgery planning. While neuroradiologists and surgeons are able to compensate for missing tracts (false negatives) using their neuroanatomical knowledge, it remains particularly challenging to understand whether a tract is not reconstructed because of tumor-related infiltration, or due to technical limitations of fiber tractography. Examples hereof include the presence of edema or a tumor-induced mass effect (brain tissue compression due to tumor growth) leading to early tract termination and consequently to an inadequate extent of reconstruction.

One of the possible ways to counter such challenges is to employ more advanced diffusion models combined with more sophisticated tractography algorithms. Unfortunately, such methods are not commonly applicable in most clinical sites. One of the reasons is that the requried acquisition is often considered time-consuming in existing clinical routines. Another reason is the occasional lack of trust among neurosurgeons and neuroradiologists for new techniques. This can be attributed to higher result uncertainty as well as a higher rate of falsely reconstructed pathways [6].

In this thesis we propose a tractography framework that reduces overall result uncertainty by providing an extent comparable to state-of-the-art probabilistic algorithms while using a deterministic implementation. Next, we showed proof-of-concept of the potential of the technique for clinical application in brain tumors. We aim to strengthen the results by also including function-based reference to validate tractography reconstructions. By performing a clinical evaluation we also try to bridge the gap between fundamental research and clinical translation of new techniques.

1.3   Summary of the thesis

In Chapter 2, a novel multi-level fiber tractography algorithm is proposed. As mentioned above, dMRI can assist surgery planning via fiber bundle reconstruction. However, certain fiber bundles, such as the corticospinal tract (CST), appear to pose a challenge to existing tractography methods. That is due to a number of fiber bundles partially overlapping and aligning towards the same orientation, creating a bottleneck [7]. Consequently, during reconstruction tractography algorithms may favor diffusion orientations that would lead to false pathways after passing

the bottleneck. The proposed tractography algorithm attempts to iteratively extend the reconstruction exploiting previously unused fiber orientations along the potential pathways. This way we aim to provide an opportunity to account for both high-angular deviation as well as potential fiber branching.

In Chapter 3, with the aim of clinical translation in mind, we evaluated the proposed fiber tractography algorithm at reconstructing the CST bundles on a dataset consisting of patients with motor-eloquent high-grade glioma. The outcomes were compared with more conventional algorithms, including clinically used DTI tractography. Radial coverage of the motor cortex was used as an evaluation metric in this comparison. Analysis of the results revealed dependence of the reconstruction extent and deformation on the presence of a mid-line shift as well as a tumor location.

In Chapter 4, to retrospectively evaluate the use of the proposed algorithm as part of an existing clinical routine, we have extended the previous study with functional data using navigated TMS mapping of the motor cortex. Functional mapping allows evaluating the algorithm performance in the most relevant areas and provides a reference to the region that is expected to be covered by the fiber reconstruction.

In Chapter 5, we venture into the brain gray matter. While gray matter is not a focus of current surgery planning routines, it is a key area to accurately map fiber bundles, as the majority originates from (or ends in) the gray matter. Mapping gray-matter structure may improve the accuracy of fiber tractography in the vicinity of the gray-white matter interface as well as the accuracy of functional mapping. However, most of the tractography developments are focused on the white matter. Thus, we investigated whether state-of-the-art spherical-deconvolution models that are conventionally used in the white matter are applicable to the gray matter. The study revealed consistent local diffusion orientation and intracortical-connectivity patterns that agree with known myelo-architecture across all the models.

CHAPTER 2

Anatomically informed multi-level fiber tractography for targeted virtual dissection

Abstract

Diffusion-weighted MRI can assist preoperative planning by reconstructing the trajectory of eloquent fiber pathways, such as the corticospinal tract (CST). However, accurate reconstruction of the full extent of the CST remains challenging with existing tractography methods. We suggest a novel tractography algorithm exploiting unused fiber orientations to produce more complete and reliable results.

Our novel approach, referred to as multi-level fiber tractography (MLFT), reconstructs fiber pathways by progressively considering previously unused fiber orientations at multiple levels of tract propagation. Anatomical priors are used to minimize the number of false-positive pathways. The MLFT method was evaluated on synthetic data and in vivo data by reconstructing the CST while compared to conventional tractography approaches.

The radial extent of MLFT reconstructions is comparable to that of probabilistic reconstruction: $p = 0.21$ for the left and $p = 0.53$ for the right hemisphere according to Wilcoxon test, while achieving significantly higher topography preservation compared to probabilistic tractography: $p < 0.01$.

MLFT provides a novel way to reconstruct fiber pathways by adding the capability of including branching pathways in fiber tractography. Thanks to its robustness, feasible reconstruction extent and topography preservation, our approach may assist in clinical practice as well as in virtual dissection studies.

2.1   Introduction

Diffusion MRI fiber tractography provides an opportunity to estimate fiber orientations through the Brownian motion of water molecules. This imaging technique allows for exploring brain connectivity in-vivo and non-invasively [8,9] as well as performing virtual dissection [10–13], aiding presurgical planning [14] and serving as a reference during surgery [15]. In case of neurosurgery planning, the extent of resected tissue may need to be limited in order to limit function deficit, despite maximal tumor resection being one of the key factors for prolonged survival [1,16]. Consequently, fiber bundle reconstructions need to have adequate extent to enable clinicians to estimate a safe resection margin. Despite its promising results, fiber tractography remains challenging, as the results of existing methods have been shown to perform satisfactory on either sensitivity or specificity, but not both [6,17,18].

For the purposes of surgery planning and virtual dissection, the sensitivity of tractography plays a key role, as the correct prediction of the extent of resection is essential to avoid functional impairment. The corticospinal tract (CST) is one of the bundles which neurosurgeons and neuroradiologists focus on during surgery planning to prevent motor function degradation [19]. However, the reconstruction of the corticospinal tracts and other pathways are often limited by intrinsic flaws of existing tractography algorithms, which by design makes it challenging to reconstruct branching configurations, leading to an increased false-negative rate [20].

Multiple approaches have been proposed to reconstruct the organization of fiber pathways from the diffusion signal, with the most common being the estimation of the fiber orientation distribution (FOD) with spherical deconvolution techniques [21–23]. Based on the way tractography methods use the information provided by the FOD, they can be categorized as either deterministic or probabilistic. Deterministic approaches follow either the dominant diffusion (or fiber) direction [24] or one of the main directions that is the least deviating from the orientation of a previous step [21,25]. On the other hand, probabilistic approaches typically sample and propagate orientations based on the FOD in the voxel [26]. Probabilistic methods can potentially reconstruct branching-like configurations and have been shown able to reconstruct more true-positive pathways than deterministic methods, but also tend to have a higher false-positive rate [6] that complicates their application in pre-surgical settings. For instance, given that directions are sampled from orientation distribution, each step introduces a bias in relation to the peaks of the distribution. Consequently, during propagation the bias may be accumulated to the extent that the reconstructed bundle does not follow known internal topographic organization [27–31] or accumulates the volume of plausibly looking pathways that will influence the safety margin estimation during tumor resection. In contrast, deterministic methods cannot reconstruct branching configurations and are prone to generating false-negative results, but their results

are reproducible by definition and straightforward to interpret. Another approach that has the potential of resolving the tractography issues related to bundle extent is global tractography (GT). GT reconstructs all white-matter fiber bundles at once by optimizing an energy function based on the diffusion data. This group of approaches aims at resolving local fiber orientations by modeling pathways as a chain of connected segments and maintaining or changing the connectivity of the segments based on the underlying data. Despite the issue of being computationally expensive and suffering from fiber pathways that sometimes do not reach the cortex, GT can show improved performance in some cases [32].

As it was already briefly mentioned, certain fiber bundles, such as the optic radiation bundle and the CST, appear to have specific topographic organization [27–31] which assigns function duties to parts of these bundles. Maintaining such internal organization appears to be a challenge for probabilistic tractography unless it is specifically taken into account [27]. This creates potential issues in cases when functional data is used for the placement of either a seed region or simply a region of interest, for instance, when direct electric or transcranial magnetic stimulation is performed, further complicating the interpretation of the tractography results. In such cases streamline representation becomes more important given an additional constraint on sub-bundles visiting finer white-matter and cortical landmarks.

Incorporating anatomical prior knowledge in the tractography might offer a viable solution to improve the quality of the CST fiber tractography, given that anatomical landmarks are well defined for this tract [13, 33, 34]. For instance, the bundle-specific approach MAGNET [35] has been previously shown to enhance the reconstruction of the optical pathways by enforcing a specific direction for tract propagation using user-defined regions of interest (ROI). A similar guidance of the fiber tracking can be achieved also using transcranial magnetic stimulation to find the brain regions responsible for specific functionality for the purpose of filtering fiber bundles related to those regions [36].

Most anatomy-aware approaches attempt thus to either improve the streamline propagation or to enhance the FOD estimation. However, the aforementioned methods do not exploit all information available in the FOD. For one, the possibility of incorporating branching configurations with high angular deviations along fiber trajectories is not taken into account by most existing approaches. This problem has been first investigated by introducing the concept of pathway splitting [37], but the proposed framework may suffer from a high false-positive rate due to complications of the splitting procedure.

In this work, we propose a novel approach to fiber tractography that adds branches to fiber pathways in a hierarchical multi-level approach (Figure 2.1). By defining target and seed regions based on anatomical priors, the algorithm imposes additional constraints on the reconstructed streamlines, limiting the number of false-positive reconstructions that might be introduced either by the algorithm or via branching. Additionally, to differentiate crossing and branching configurations, only if a pathway does not reach the target, the peaks of the corresponding FODs

may be considered as branches. This concept can be integrated into a wide range of tractography algorithms, e.g., any algorithm based on an FOD both probabilistic and deterministic. In this work we focus on the proposed multi-level strategy in combination with deterministic constrained spherical deconvolution (CSD) based tractography [25].
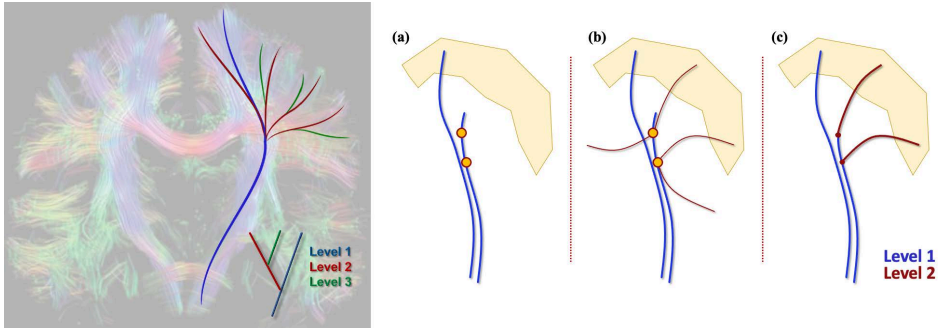
Figure 2.1: (Left) Current fiber tractography methods such as deterministic FOD-based tractography reconstruct only a subset of the pathways (blue). However, by propagating along the FOD orientations that were not used by a conventional tractography algorithm, the reconstruction can be iteratively extended by adding new sets of branches per iteration (red and green) leading to a final tractography result consisting of multiple levels. (Right) The pipeline of the algorithm. (a) The tract produced by the deterministic CSD-based tractography includes points with multiple FOD peaks, some of which are ignored. (b) Using these points as seeds with the unused peaks as initial locations, another iteration of CSD-based tracking is performed to obtain a new level of the result. (c) In the last stage only the tracts that enter the predefined target region are retained. The background picture on the left of the whole-brain fiber tractography result is taken from [38] with permission.

2.2 Methods

2.2.1 Multi-level fiber tractography

The core of our algorithm is a multi-level fiber tractography (MLFT) strategy that is compatible with a wide range of fiber tractography methods to take potential branching configurations into account. It is an iterative procedure that is capable of generating multiple spurious pathways and, consequently, requires user-defined starting and target regions as well as stopping criteria in order to control false-positive rate. MLFT can be combined with both deterministic and probabilistic

methods. In name of clarity, in this first work we choose to focus on combining our tractography strategy with deterministic CSD-based streamline tracking [25].

Our algorithm iteratively expands the reconstruction by branching from the pathways not reaching the target region. The set of streamlines visiting target region and added at one iteration can be considered one level of the overall bundle reconstruction. At each iteration, conventional deterministic CSD-based tractography is performed while storing information on which peaks were chosen for propagation at each point. If a reconstructed streamline does not enter the user-defined target region, its points that correspond to FODs with unused peaks are used as seeds for a new tractography level. Initial directions are defined as the FOD peaks that were not used during the reconstruction of the previous levels. The algorithm runs for a pre-defined number of levels or until a pre-defined convergence criterion is met. Finally, tracts that do not enter the target region at any of the considered levels are discarded (Figure 2.1), which is a critical step to prevent the generation of aberrant branches. Co-existence of fiber crossings and fiber branching is facilitated by treating FOD peaks as crossings during propagation and only considering them as potential branches at the following iteration if a corresponding pathway does not reach a target region.

2.2.2   Data

We performed experiments on both simulated and acquired diffusion weighted images. A numeric phantom was generated using ExploreDTI [39] (v4.8.6; PROVIDI Lab, Utrecht, the Netherlands) with 6 volumes at $b = 0s/mm^2$ and 60 volumes at $b = 1200s/mm^2$ with a resolution of 1mm isotropic (Figure 2.2). The phantom represented three fiber bundles with two branching spots, conceptually mimicking fiber configurations as those that can be observed in the CST. The experiments with this phantom were performed without noise and for two signal-to-noise ratio (SNR) levels: 25 and 15.

In order to analyze the performance of our method on in-vivo brain images, the MASSIVE [40] dataset was used. The data consisted of 430 volumes at $b = 0s/mm^2$, 250 volumes at $b = 500s/mm^2$, 500 volumes at $b = 1000s/mm^2$, $2000s/mm^2$ and $3000s/mm^2$ each, 600 volumes at $b = 4000s/mm^2$. The data was acquired with a resolution of 2.5 mm isotropic. The MASSIVE dataset was corrected for signal drift [41], subject head motion, eddy current and echo-planar imaging distortions [42].

Additionally, we applied our method to the preprocessed data of ten subjects from the Human Connectome Project (HCP). The data had a resolution of 1.25mm isotropic and contained 18 volumes at $b = 0s/mm^2$ and 90 volumes at $b = 1000s/mm^2$, $2000s/mm^2$ and $3000s/mm^2$ each.

Multi-shell CSD [43] was used for the FOD estimation. The motor cortex was segmented as a combination of the left and right precentral and paracentral gyri (Figure 2.3) with FreeSurfer [44–46] (v6.0.0, Laboratory for Computational
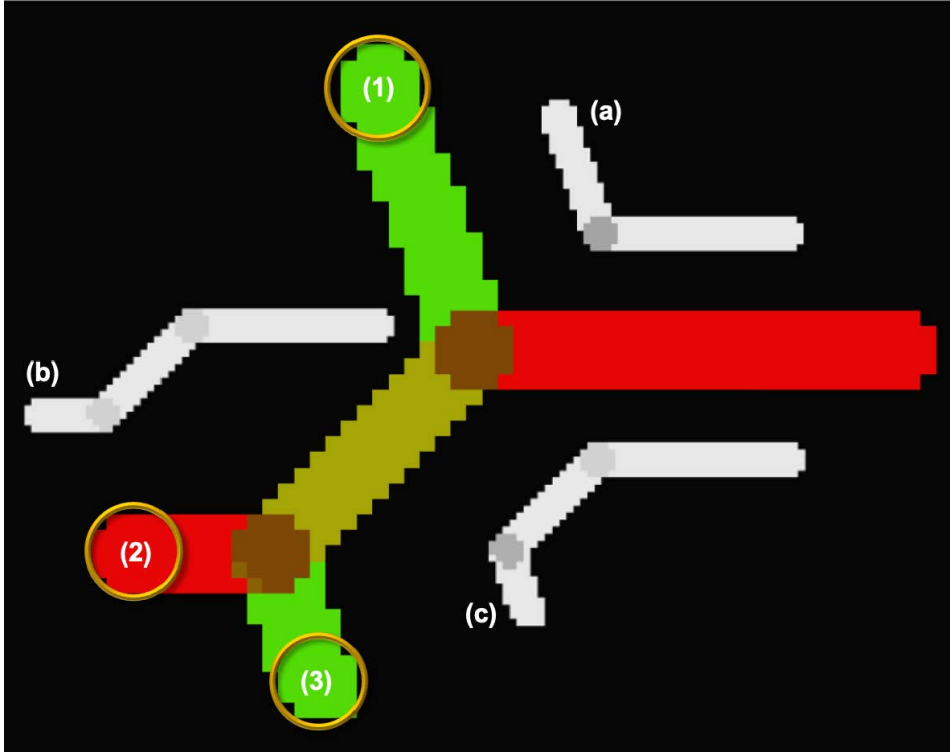
Figure 2.2: A representation of the numeric phantom (colored based on diffusion direction and FA value) with two branching points. It consists of three individual fibers (a-c, colored according to FA value) with corresponding endpoint regions [6, 10, 34].

Neuroimaging, Charlestown, MA, USA) and was used as a target region.

2.2.3   Experiments

Experiment 1. Tractography in silico. We evaluated MLFT as well as iFOD2 [47], as it is a popular choice of probabilistic tractography algorithm, using a noiseless phantom. In all the experiments the implementation of iFOD2 from the MRtrix package [48] was used and all the options were set to default except for providing the seeding region. The same seed point was used for tracking in both cases.

The endpoint regions were placed at the separate ends of each sub-bundle (Figure 2.2) that served as target regions of interest for MLFT. They were also used to select the target fibers from the results of iFOD2, which was run with default parameters. The parameter setup for MLFT was as follows: angle threshold $= 45°$,

Figure 2.3: The target cortical region. To reconstruct the corticospinal pathways, the motor cortex (red) was delineated for both hemispheres with FreeSurfer.

maximum order of spherical harmonics $L_{max} = 8$, FOD peak value threshold $= 0.1$, the default value in ExploreDTI. The step size was set to half the voxel size and the number of iterations was set to two.

Experiment 2. Robustness to noise. The sensitivity of the MLFT to noise was tested. Fiber tracking was performed for the phantoms at varying SNR levels with the same settings as in Experiment 1. The target fibers were then compared across SNR levels.

Experiment 3. Tractography in vivo. The MLFT approach was used to delineate the CST with the MASSIVE and HCP brain data described above. The motor cortex area of both hemispheres was used as a target region. The added value of our multi-level strategy was investigated more closely on the fanning projection of the left CST.

In order to evaluate whether MLFT reconstructs parts of the pathways belonging to the corpus callosum (CC), the bundle was delineated with both deterministic CSD-based whole-brain tractography and MLFT. The overlap of the CST and the CC generated by MLFT and CSD-based whole-brain tractography, respectively, was visually evaluated. The results of our algorithm were evaluated along with the results produced by the conventional deterministic CSD-based tractography from ExploreDTI as well as iFOD2 and GT [49] implemented in MRtrix. The CSD-based tractography, MLFT and iFOD2 used the same seed regions. The streamlines reconstructed by iFOD2 were further selected to include only the tracts that visit the target cortical area. In the case of GT, the masks of the seed and target regions were used to delineate the CST from the whole-brain tractography. To improve the visual interpretation of the results, implausible streamlines were removed using identical exclusion regions for all methods in case of the MASSIVE dataset.

Radial extents of the reconstructed bundles were calculated. In order to do

that the area covered by bundles endpoints in the cortex was calculated given that coronal projection of the motor cortex defines a 90° segment. Obtained radial extents were compared per hemisphere using paired Wilcoxon signed-rank test with significance level $\alpha = 0.05$. Additionally, density distributions of the endpoints in the motor cortex were evaluated per subject for each algorithm.

The tractography parameters were set as in Experiment 1. Reconstructions with two iterations (for both MASSIVE and HCP) and three iterations (only for MASSIVE) were performed with MLFT. To obtain the whole brain reconstruction with GT, the number of iterations was set to 109, segment length $= 1.5mm$, maximum spherical harmonics order $L_{max} = 8$. The default values were used for the remaining settings.

To reconstruct the CST with the MASSIVE dataset, the seed regions were placed close to the internal capsule. In case of HCP subjects an axial cross section of the brain stem was used. For seeding 100 points per voxel were evenly distributed at a single slice level. The number of seed points per voxel was selected empirically.

To run iFOD2 the FODs that were used for MLFT and CSD-based reconstructions were converted to MRtrix format using MRIToolKit (Image Sciences Institute, UMC Utrecht, the Netherlands). iFOD2 was provided with a mask of the seed region used for MLFT, seed_image option was used. When performing iFOD2 on the HCP data, the number of selected pathways was empirically set to 10000. In addition, the target regions were provided using include option, while the same function was used for filtering as in MLFT in case of the MASSIVE dataset. During the analysis of the HCP data, a NOT gate was used to remove inter-hemispheric connections, due to the use of the common seed region in the brain stem for both of the CST branches.

Experiment 4. Topographic organization. Previous research has established that both the motor cortex and the internal capsule can be divided into regions corresponding to specific motor functions, and that such organization is preserved within the CST [30,50]. The topography preservation index (TPI) [51] was calculated, which highlights whether pathways that pass in close proximity to each other through the internal capsule also have closely located endpoints in the motor area. This index reflects how well the internal organization is preserved in the bundle reconstruction. The lower the TPI score the more topographic organization is preserved in the reconstruction.

In order to calculate TPI scores, rectangular ROIs were defined around the left and right internal capsules, then the longest axis of the ROI was used to map all the tract points crossing the ROI onto [0; 1] segment. Consequently, each pathway is assigned a value $v_i \in [0;1]$, where i is an index of a pathway. Afterwards, a triangulation is built using the endpoints in the motor area and each edge connecting two endpoints of pathways j and k is assigned a weight equal to the distance of the projections in the ROI: $w = |v_j - v_k|$. Finally, the TPI score is an average of the weights. The edge in the calculated triangulation

signals close proximity of the endpoints in the motor area, while the weight serves as a penalty if the corresponding pathways' locations in the internal capsule are distant.

The TPI was computed for the left and right CST branches reconstructed by each of the algorithms. To visually appreciate such organization, the CST streamlines were colored according to the part of the area of the motor cortex they reach. This allows to visually check whether the pathways reconstructed by MLFT and iFOD2 on the MASSIVE data corresponded to the anatomical position of the same associated function in the internal capsule. Additionally, statistical testing was performed to compare obtained TPI scores using paired sign-rank Wilcoxon test with significance level $\alpha = 0.05$.

Experiment 5. Anatomical plausibility. As the previous experiment evaluates topography preservation capability of the algorithms by comparing relative placement of the endpoints, the coherence of the pathways was evaluated in order to observe whether the geometric similarity between pathways closely located to each other along their length is associated with the calculated TPI scores. We hypothesize that a fiber reconstruction with a lower intrinsic geometric similarity corresponds to a higher TPI, highlighting the effect of the bias on fiber pathway propagation. To this end, the minimum average direct-flip (MADF) distance was employed, which previously has been used in bundle clustering applications [52, 53]. This metric represents the average point-to-point distance between two pathways and is invariant to the ordering of the points in each pathway (e.g., to which endpoint is considered the start/end). It is defined in the following way: $D_{AB} = \min\left(\frac{1}{N}\sum_{i=1}^{N}||a_i - b_i||, \frac{1}{N}\sum_{i=1}^{N}||a_i - b_{N-i+1}||\right)$, where a_i and b_i are the points of the pathways A and B of length N, respectively. The metric requires the compared tracts to contain an equal number of points, which is why all the pathways were uniformly resampled to $N = 200$ points. Evaluations were performed on the left and right CST bundles of the MASSIVE and HCP data obtained by the tested methods without filtering gates. For each set of the reconstructed pathways of a given subject, an all-to-all distance matrix was calculated. Then, for each pathway, the minimum distance was calculated based on that matrix.

2.3   Results

Experiment 1. Tractography in silico. Both MLFT and iFOD2 reconstructed all the phantom branches of the noiseless DWI phantom, as shown in Figure 2.4. It can be observed that the results of MLFT follow the underlying simulated directions, whereas iFOD2 produces trajectories oscillating around the ground truth.

Experiment 2. Robustness to noise. The results of MLFT obtained for three different SNRs are presented in Figure 2.5. A slight misalignment lower than
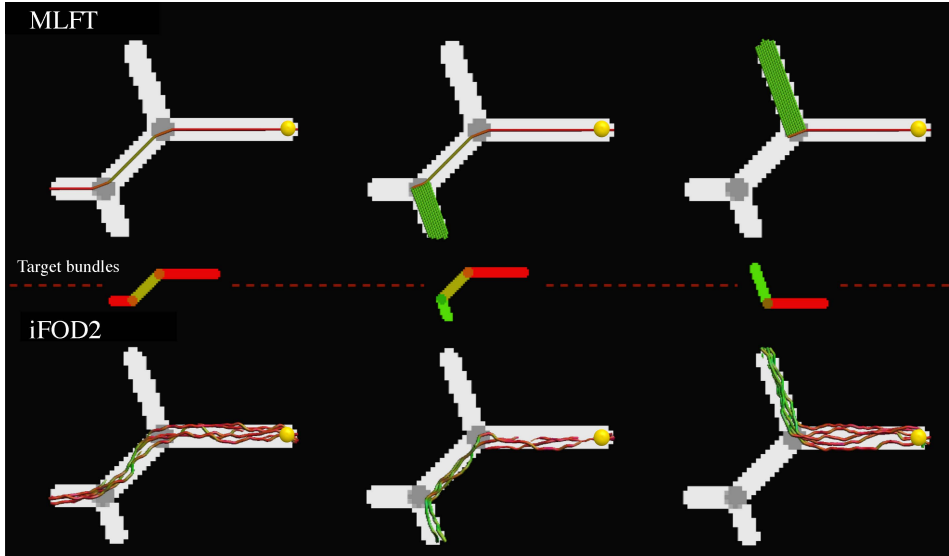
Figure 2.4: Performance of the considered methods in phantoms (FA map). The top row shows the results of MLFT and the bottom row those of the iFOD2 algorithm. The middle row illustrates the target fibers per column (orientation-based colored FA map). The same single seed point (yellow sphere) was used for both algorithms. The results of iFOD2 were subsampled for easier visual assessment. Streamlines' colors are based on orientation color-coding.

$10°$ can be observed at the branching point at $SNR = 25$, which becomes more evident at $SNR = 15$ with values up to $30°$. The case with the lowest SNR is also characterized by an increased pathway number of branching configurations at the points where original bundles diverge, as can be seen in the top row in Figure 2.5.

Experiment 3. Tractography in vivo. The multi-level structure of the reconstructed left CST bundle can be seen in Figure 2.6, which clearly shows the benefit of the proposed algorithm over conventional deterministic CSD-based tractography with the improved extent of the bundle fanning. The addition of an extra layer increases the number of streamlines reaching the motor cortex but does not bring further improvement to the coverage of the motor cortex: the radial extent with 3 levels amounts to $75.66°$ while, 2-level reconstruction has an extent of $71.48°$. Consequently, in all of the in-vivo experiments the number of levels was set to two.

The full reconstructions of the CST segmented by MLFT, iFOD2, GT and deterministic CSD-based tractography in the MASSIVE data is shown in Figure 2.7. It can be observed that the obtained with MLFT pathways densely cover most of the motor cortex unlike the results of deterministic CSD-based tractography.
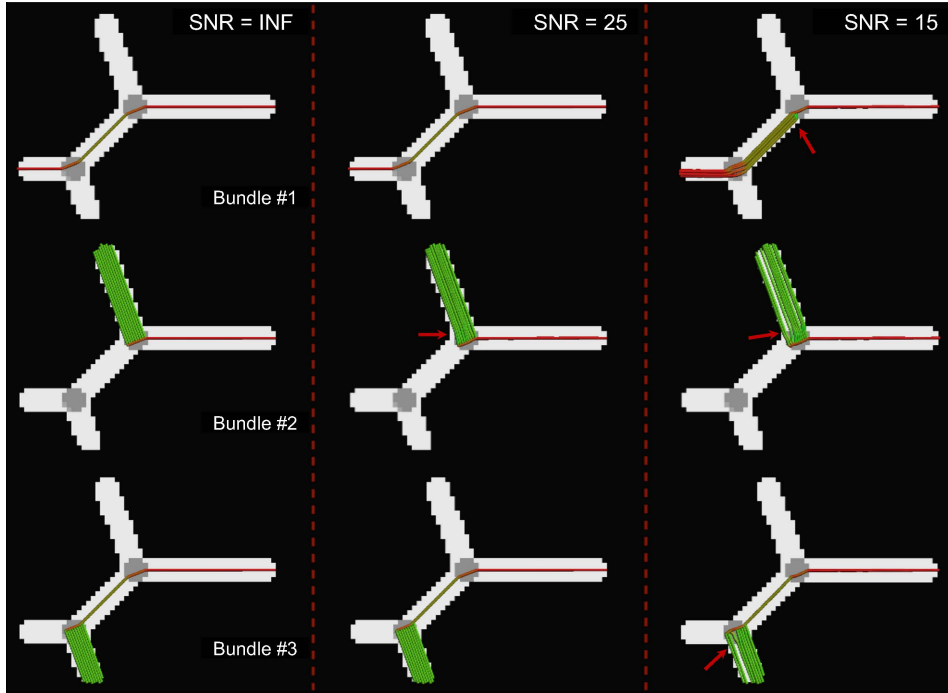
Figure 2.5: Tracts reconstructed by MLFT on the phantom data (FA map) at multiple SNR levels. Considerable angular errors are only observed at SNR = 15: increased number of branching configurations and direction perturbations up to 30º (red arrows). At SNR = 25 there is a minor angular deviation below 10º (red arrow). Streamlines are colored using standard orientation color-coding.

At the same time, both MLFT and iFOD2 cover most of the motor area Figure 2.7. For the iFOD2 reconstruction, the pathways traversing into contralateral hemisphere are present due to them bending after visiting the target region, returning into the white matter and propagating through the CC.

Regarding the reconstruction achieved by GT using the MASSIVE dataset, although the CST fanning is quite sparse, it reaches most parts of the motor cortex (Figure 2.7). The sparsity allows for a closer comparison of the multi-level and global tractography results which can be seen in Figure 2.8. Unlike in the case of GT, the CST reconstructed by MLFT does not reach the approximate leg-related motor area. In the face area the pathways generated by GT are aligned to those generated by MLFT, although they do not show any branching, but rather a smooth curving trajectory.

The CST bundles that were reconstructed for the HCP subjects by the proposed approach, iFOD2, GT and deterministic CSD-based tractography are shown
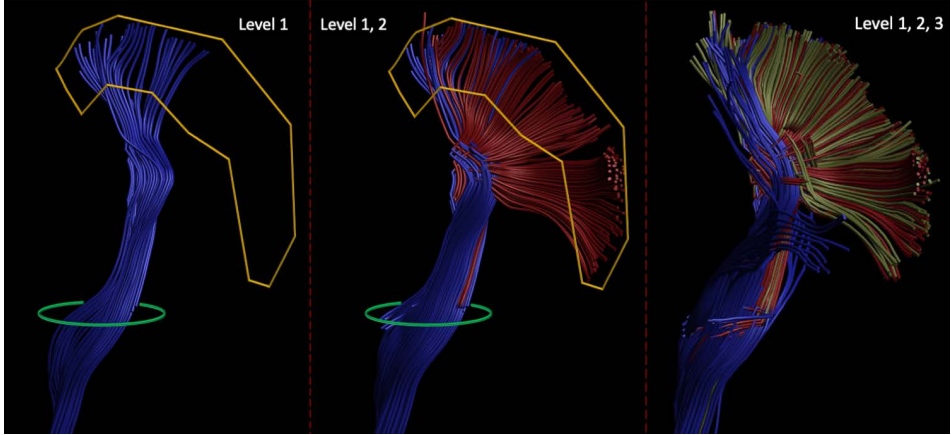
Figure 2.6: Fiber pathways reconstructed by the deterministic CSD-based approach (left) and MLFT with two (middle) and three (right) levels from the same seed region (green) with the same target region (yellow, the motor cortex) using MASSIVE dataset. Adding the second-level branches (red) to the pathways obtained at the first level (blue) improves the extent of the reconstructed bundle. Using three-level reconstruction from the same seed region does not show coverage improvements over the two-level reconstruction.
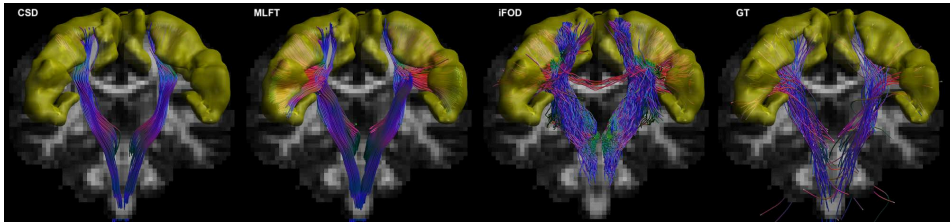
Figure 2.7: Corticospinal pathways reconstructed by the conventional deterministic CSD-based tractography, MLFT, iFOD2 and global tractography using the MASSIVE data. The motor cortex is shown in yellow. Some of the pathways reconstructed by iFOD2 enter the motor cortex and diverge into the CC propagating into the contralateral hemisphere.

in Figure 2.9. Overview of the radial extents achieved by all the employed algorithms can be seen in Figure 2.10. Regarding iFOD2, the results have the same characteristics as the results obtained using the MASSIVE data described above. Generally, both MLFT and iFOD2 reconstructions are represented by the bundles with a plausible fanning extent. GT seems to show lower radial extent compared to its result using the MASSIVE data.

Despite iFOD2 and MLFT both showing high radial extent, in case of iFOD2
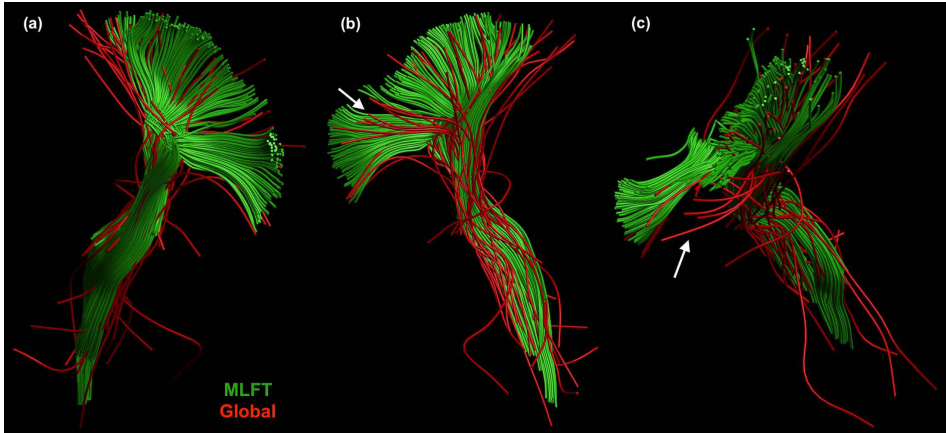
Figure 2.8: Comparison of the left CST reconstructions obtained by MLFT (green) and GT (red) using the MASSIVE dataset. (a) The reconstruction by GT is sparser, but it provides additional coverage towards the approximate leg area unlike the MLFT reconstruction. (b) Pathways delineated by GT generally follow the same trajectory of the bundle reconstructed by MLFT but with smoother branching turns. (c) Some of the GT-produced pathways that are reaching the face motor area (white arrows in (b) and (c)) are shifted towards posterior part of the brain and are not completely aligned with others as well as with the corresponding part of the MLFT-reconstructed fanning.

the tempo-lateral part of the motor cortex is covered more sparsely than its superior part (Figure 2.11), At the same time, MLFT provides more uniform coverage of the motor cortex, although the superior motor cortex coverage is still relatively denser. Given the sparse reconstruction achieved by GT, its density distribution also appears quite uneven as can be seen in Figure 2.11.

Performing statistical testing to compare the radial extents of the algorithms has shown no statistically significant difference between MLFT and iFOD2: $p = 0.21$ for the left and $p = 0.53$ for the right hemisphere. Also, no significant difference is observed between GT and CSD-based tractography: $p = 1$ for the left and $p = 0.06$ for the right hemisphere. All the other comparison combinations when performing Wilcoxon test resulted in p values lower than the significance level.

The CST and CC bundles reconstructed using a subject from HCP data are depicted in Figure 2.12 for comparison. In the axial view it is well visible that part of the CST fanning does not overlap with the CC pathways, as the CC is not covering lateral part of the motor cortex.

Experiment 4. Topographic organization. The TPI scores are reported in Table 2.1. The deterministic CSD-based tractography seems to outperform other
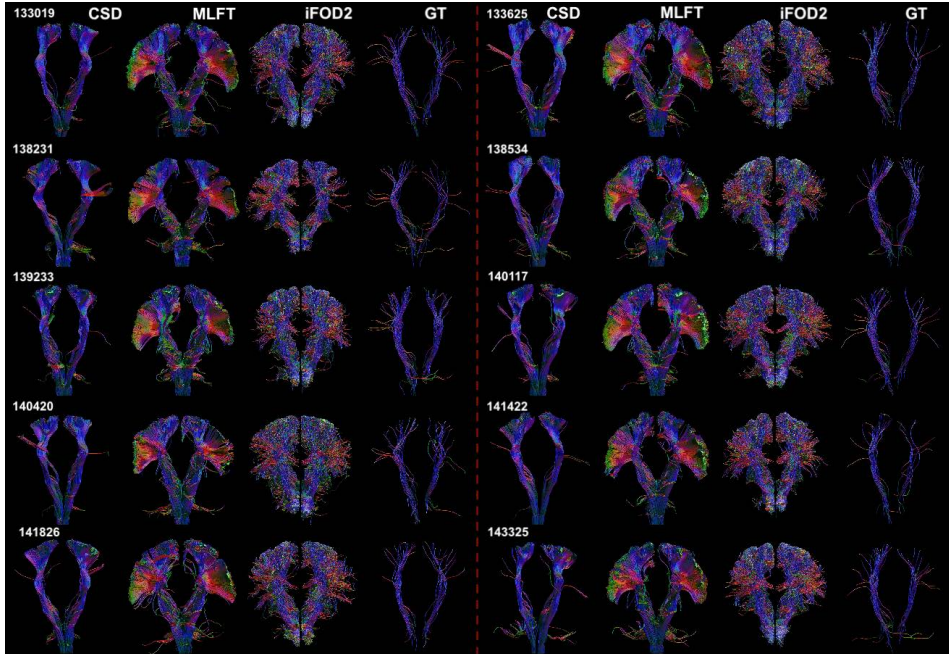
Figure 2.9: The CST reconstructions obtained by MLFT, iFOD2, GT and CSD-based tractography using the HCP data. The reconstructed by MLFT bundles are in line with the observations in Figure 5 and consistent with each other. iFOD2 also achieves high motor cortex coverage. The extents of the GT-reconstructed bundles are comparable to the ones obtained by MLFT, but with less satisfactorily spatial coverage.

algorithms showing lower values of the TPI metric, and thus higher coherence, for every subject. Both MLFT and CSD-based tractography achieved TPI scores that are significantly different from the scores of both iFOD2 and GT with $p < 0.001$. Despite rather close mean scores (0.03 and 0.06 for the left and 0.03 and 0.05 for the right CSD-based and MLFT reconstructions respectively) MLFT and CSD-based reconstructions were shown to achieve significantly different TPI scores ($p < 0.001$). MLFT is shown to have seemingly comparable TPI scores than the CSD-based tractography, while they are still consistently lower than the scores of iFOD2 and GT reconstructions. In this regard, iFOD2 and GT show generally comparable performance to each other without statistically significant difference: $p = 0.17$ for the left and $p = 0.21$ for the right hemisphere.

Figure 2.13 shows the pathways color-coded according to their final locations in the motor cortex. The visualization demonstrates that MLFT maintains the anatomical configuration of the pathways, according to which the organization of
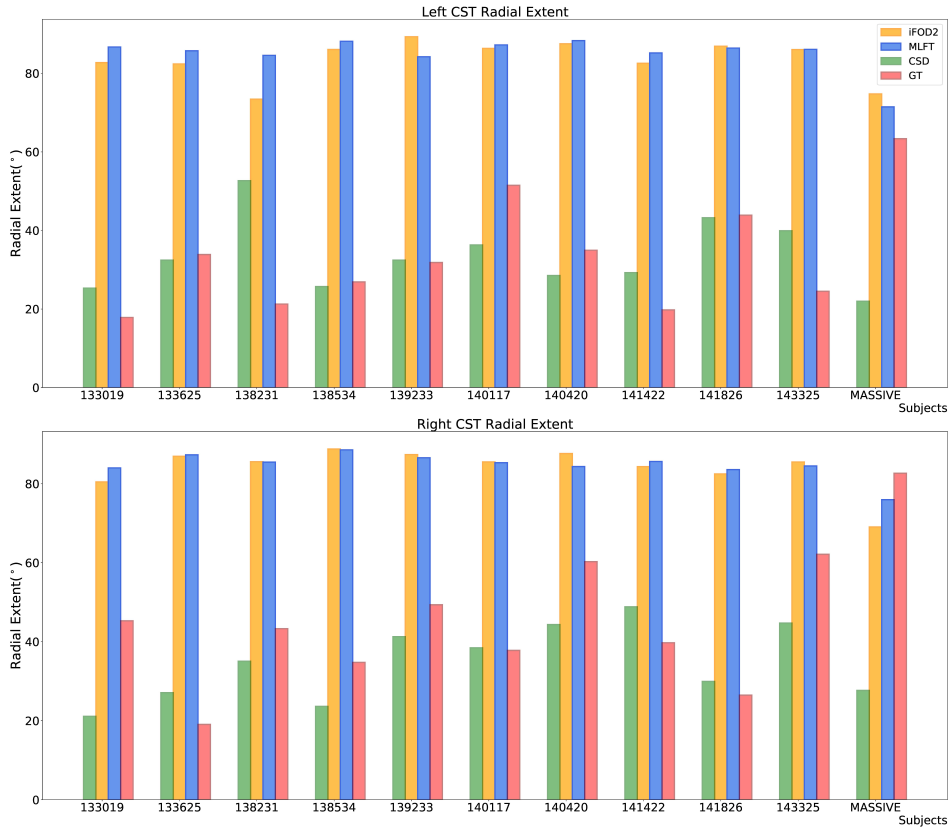
Figure 2.10: Radial extents of the reconstructed CST bundles for both left and right hemispheres. MLFT (blue) is shown to improve the radial extent compared to the conventional deterministic CSD-based tractography (green). iFOD2 (orange) and MLFT (blue) appear to have comparable radial extents. GT (red) achieves high radial extent on the MASSIVE dataset, while on HCP data the extent is primarily low.

tracts connecting specific sub-domains of the motor cortex is maintained throughout the bundle. In contrast, the bundle produced by iFOD2 seems to be less organized.

Experiment 5. Anatomical plausibility. The normalized histograms of the MADF distance are shown in Figure 2.14. The distributions are similar across subjects per tractography approach and show that the distance between the closest pathways obtained by MLFT is generally smaller than that of iFOD2. The results of GT showed the highest distance, which is attributed to the sparsity of the bundles. The CSD-based reconstructions also appear to be very similar
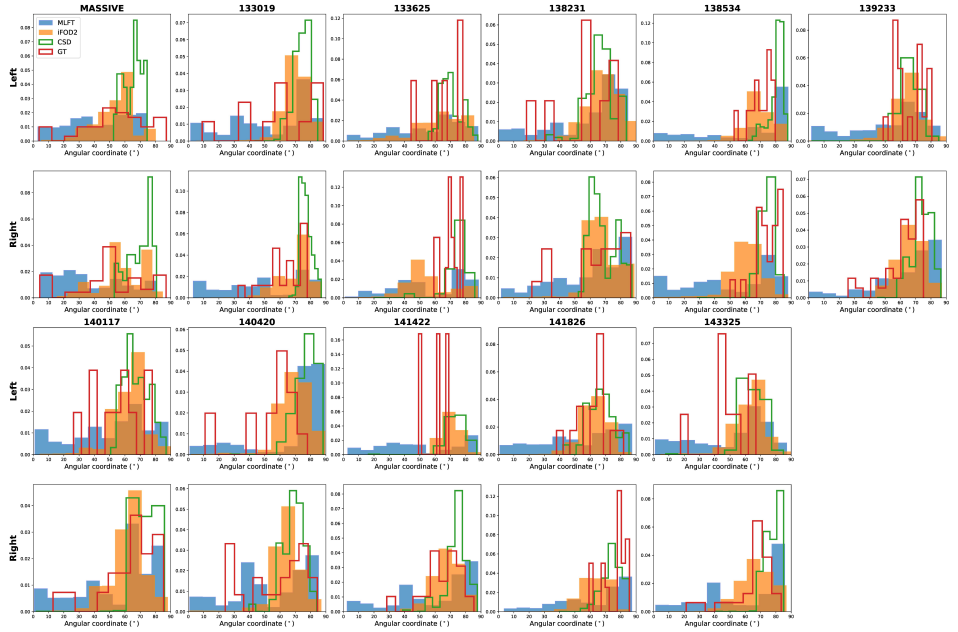
Figure 2.11: Density of the motor cortex coverage by the reconstructed CST bundles considering with angular coordinate starting at tempo-lateral point of coronal projection of the motor cortex and increasing towards superior motor cortex separately for each hemisphere. All the algorithms appear to densely cover superior part of the motor cortex. However, MLFT (blue) consistently covers most lateral part of the motor cortex with its density more evenly distributed compared to iFOD2 (orange). GT (red) also occasionally covers tempo-lateral motor cortex, although the coverage is very sparse. CSD-based tractography (green) primarily covers superior motor cortex part in all the subjects.

geometrically according to the MADF distance with the peak of the distribution being very close to zero for most of the subjects.

2.4   Discussion and Conclusion

In this study we presented MLFT, a novel strategy to enhance fiber tractography by reconstructing branching configurations. The strategy we propose achieves anatomically plausible reconstructions of the CST bundles, is robust and reproducible, and maintains topographic organization. Each iteration of the proposed tractography algorithm attempts to branch existing streamlines towards the target region, which may open up new avenues for investigating more complex pathway
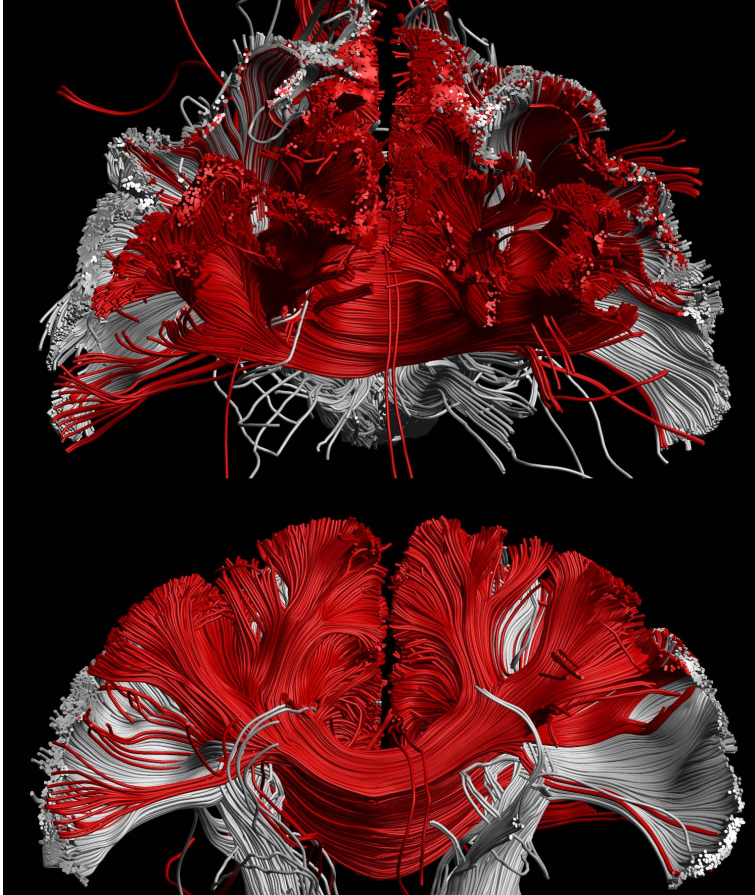
Figure 2.12: The CST bundle (white) reconstructed by MLFT, and the CC bundle (red) reconstructed by whole-brain CSD-based tractography using a subject from the HCP dataset. The CST bundle was reconstructed using MLFT while the part of the CC bundle was extracted from whole-brain reconstruction obtained with the same parameters as in case of the MLFT reconstruction. An overlap can be seen in superior lateral part of motor cortex as well as occasionally in its temporal part. As it is known that the CC also originates from the motor cortex, the results support the ambiguity of whether the second-level branches the CST reconstruction belong to the CC or the CST, as they were not reconstructed by the deterministic CSD-based tractography in either cases given the same parameter settings.

configurations in the brain [54]. Given that image resolution is usually not suffi-cient to distinguish branching points, some of the FOD peaks might not only be

Subject	Left				Right			
	CSD	MLFT	iFOD2	Global	CSD	MLFT	iFOD2	Global
MASSIVE	0.08	0.08	0.15	0.18	0.08	0.08	0.21	0.17
133019	0.03	0.06	0.13	0.36	0.02	0.05	0.1	0.21
133625	0.03	0.05	0.36	0.11	0.03	0.05	0.1	0.08
138231	0.02	0.06	0.36	0.2	0.02	0.04	0.09	0.25
138534	0.03	0.05	0.3	0.1	0.03	0.05	0.16	0.23
139233	0.02	0.07	0.43	0.12	0.03	0.07	0.15	0.1
140117	0.02	0.05	0.11	0.13	0.02	0.04	0.1	0.11
140420	0.04	0.07	0.15	0.14	0.03	0.06	0.1	0.15
141422	0.03	0.06	0.46	0.09	0.02	0.04	0.09	0.26
141826	0.02	0.05	0.18	0.12	0.02	0.05	0.09	0.1
143325	0.02	0.04	0.08	0.13	0.02	0.04	0.1	0.09

Table 2.1: TPI scores of the left and right CST reconstructions by MLFT, iFOD2 and GT and also the TPI score of the first level of MLFT only, which is reconstructed by deterministic CSD-based tractography (the lowest score is indicated in bold). According to the TPI values, the CSD-based reconstruction of both CST branches has best-preserved topography. The scores of MLFT and CSD are comparable and consistently low in contrast to iFOD2 and GT.
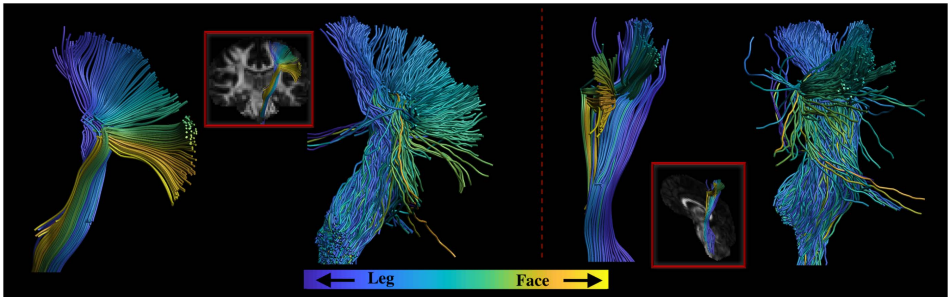
Figure 2.13: Coronal and sagittal views of the left CST reconstructed by MLFT and iFOD2 using the MASSIVE data. The fiber pathways are colored according to the locations of their endpoints in the motor cortex. The pathways reconstructed by MLFT are shown to have a clearer topographic organization.

an indication of crossing fibers, but of branching ones.

Given the improved extent of the bundles and anatomically imposed control over false positives, our approach is attractive for a number of applications. It can be used to support presurgical planning, as it reveals more extensive coverage of the motor cortex than the conventional deterministic CSD-based tractography [5, 55], while maintaining clear structure of the reconstructed bundles.
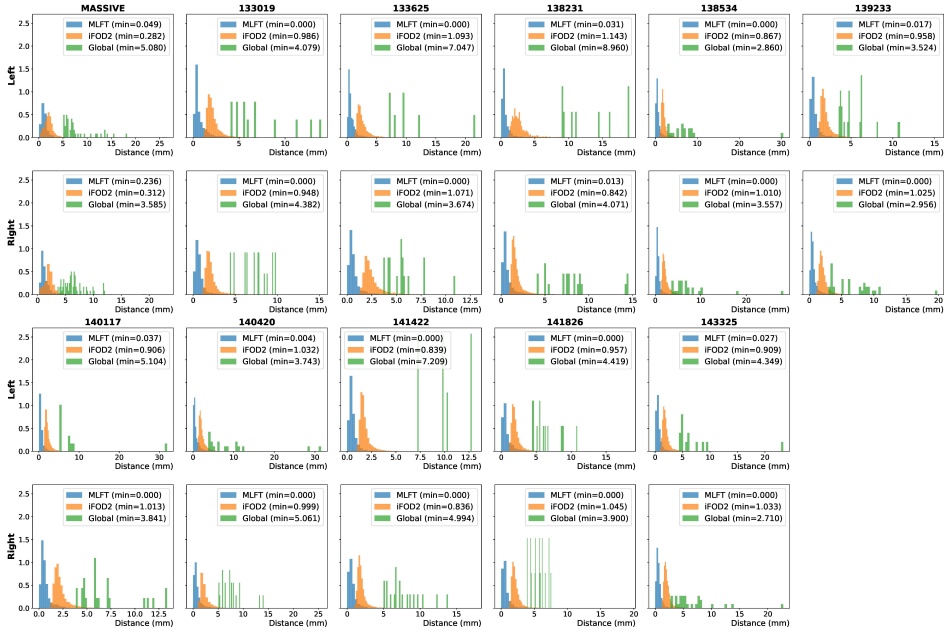
Figure 2.14: Normalized distributions of the distances from each pathway to the nearest neighbor based on the MADF distance for all the processed subjects. The distributions of the distances appear to be similar across subjects.

2.4.1   MLFT features

With simulations, we have shown that MLFT can reliably reconstruct branching fiber configurations that are less tortuous as compared to a probabilistic algorithm (Figure 2.4). Additionally, the results of MLFT are reproducible. Although higher tortuosity of the probabilistic tractography reconstruction is an expected behavior, overcrowded reconstruction makes it a bit more challenging to spot spurious pathways. This also can be connected to the ability of the tractography algorithms to maintain topographic organization, which is relevant in applications involving brain stimulation methods, such as transcranial magnetic stimulation or direct electric stimulation.

Robustness to noise is another important aspect to consider. In order to analyze the sensitivity to noise of our algorithm, the same phantom bundles were simulated with three different SNR levels. The effect of SNR on the reconstructed pathways became clearly visible only at the lowest SNR level ($SNR = 15$), as reflected by an increased number of branching configurations and occasional perturbations after branching (Figure 2.5).

When using the concept of branching for in-vivo brain tractography a well-

delineated fanning was observed close to the motor cortex (Figure 2.6). Although, MLFT and iFOD2 achieved comparable reconstructions (Figure 2.10) of the CST fanning without statistically significant difference, iFOD2 reconstruction contains multiple spurious tracts (Figure 2.7, Figure 2.9). Apart from that MLFT reconstructions show more uniform coverage of the lateral part of the motor cortex, while iFOD2 appears to be provide much denser coverage of the superior motor cortex while sparsely lateral part (Figure 2.11).

Most of the fanning consists of second level branches, which might often look as if they diverge into another bundle at the branching points making a sharp turn. However, high angular deviations have been observed by Van Wedeen et al [56]. Similarly, Mortazavi, et al [20] also observed axon T-branching as well as sharp turns at sub-millimeter scale performing tract tracing experiments in the area under the motor cortex. Both of those papers present results based on the analysis of the macaque brain, but the statements are likely also valid for the human brain, which is reportedly congruent to the structure of the macaque brain [20], although it is difficult to provide estimates on the distribution of this type of branching in the human CST dissections. Additionally, certain cases can be considered a branching from a modeling point of view given the resolution. For instance, in case of the CST the fibers originating in the cortex descend into the trunk of the bundle. At this point they pass through a "bottleneck" (at sulcus circularis insulae) and merge together [57]. As was presented in [7], up to 7 bundles appear to co-exist in a single voxel in the mentioned area, which would also suggest that some of the peaks may indicate a splitting of a bundle or an overlap of two bundles. Additionally, the angle between the CST trunk and the fanning close to the "bottleneck" area appears to be around 90° (Figure 5 in [57]), which is usually absent due to the angular deviation threshold as propagation is uncapable of making sharp turns. For this reason, probabilistic approaches struggle with reconstructing the inferior lateral part of the CST without smoothing the angle between the trunk and the fanning of the CST (Figure 2.11). However, setting a threshold as high as nearly 90° for probabilistic tractography would overflow the result with false positives by allowing sampling not only around the FOD extremums.

The validity of the MLFT reconstructions can also be evaluated with Figure 2.12. It is known that part of the CC originates from the motor cortex [34, 58]. Thus, a successful reconstruction of the motor part of the CC remains prone to ambiguity as the CST pathways are present in that area as well. Similarity of the shapes of the MLFT-reconstructed bundles to those presented by Wasserthal et al [59] provides additional confidence in plausibility of the results obtained by MLFT. Additionally, the comparison to the results of GT (Figure 2.8) has shown that this alternative approach reconstructs similar pathways, although with certain smoothing of the high-angular bifurcations that are observed in MLFT results. In general, the resemblance between the second level of the CST and the CC bundle can be explained by the co-alignment of the pathways of different bundles near

the motor region reported by W. Krieg for the macaque brain and for the human brain [60]. This does not necessarily demonstrate that these similar pathways are true positive but serves as a reference which shows stable delineation of certain structures across various algorithms.

Specific topographic organization is a characteristic of a number of brain fiber bundles [28]. Somatotopic organization of the CST [29, 50] is one of the established examples of known internal bundle organization. Similarly to [27], we have evaluated the ability of the algorithms to maintain topographic organization using TPI score. According to the observed results, MLFT can preserve topographic organization of the fiber bundles as can be seen in Figure 2.13. This is also reflected by the TPI scores (Table 2.1) across all the subjects analyzed in this study. The fact that topography preservation of MLFT is hampered compared to the deterministic CSD-based tractography might be a consequence of either obvious false-positive streamlines or precision mistakes, as in some cases first-level pathways terminate close to the target region and then branch at acute angles to reach it and thus change the expected point location. By following the FOD peaks, we propagate the streamlines along the most reliable fiber orientation and, consequently, we are less affected by the noise. This leads to a more stable pathway propagation and, consequently, to a more anatomically reliable organization of the bundle. This is also supported by the presented higher values of pathway coherence of CSD-based tractography and MLFT compared to iFOD2 and GT (Figure 2.14).

2.4.2   Limitations

Some degree of uncertainty propagates in the results from the CSD procedure, as the response function is not voxel-wise perfect and FOD peaks have limited angular resolution. This limitation is, however, inherent to most tractography algorithms. Further, branching along a pathway might generate false-positive reconstructions. In our current implementation, correctly chosen anatomical priors are key to control the rate of false-positive pathways.

As revealed by the experiments with the phantom (Figure 2.4), deterministic reconstruction from a single point may generate a whole dense branch, leading to an unrealistic density distribution. This is a result of the current implementation choice, of not imposing an upper limit to the number of times a streamline is allowed to branch. We believe that this aspect could be potentially improved in future work, for example, with a microstructure-informed extension of our framework.

2.4.3   Methodological considerations

Given the results of the three-level reconstruction (Figure 2.6), it seems increasing the number of reconstructed levels requires an increasingly accurate delineation of the target region. While error propagation across multiple levels may lead to

spurious results, at the same time, the definition of the seed region seems to play a key role in the robustness of the reconstruction. In both HCP and MASSIVE datasets, the seed regions were placed based on specific landmarks (brain stem and internal capsule). Incomplete segmentation of those regions would probably lead to reduced density of fiber pathways and, as a consequence, reduced quality of the reconstruction.

In this work the analysis was fully focused on the application of the CST bundle given the well-defined anatomical landmarks that can be associated with the target and seed regions. Consequently, spurious pathways are often easy to detect which may not be the case for bundles. For instance, to test the generalizability of MLFT, a reconstruction of the cingulum was performed with the MASSIVE dataset (Figure S6). Despite the reconstruction being visually similar to the reference bundle from the ISMRM 2015 challenge, certain pathways may as well be spurious. For that reason, the MLFT reconstruction should be treated as a guidance, unless the target region is defined based on functional data. In any case, general prior knowledge of the anatomical configuration of the fiber bundle-of-interest is required to disambiguate interdigitating from branching pathways.

We would also like to stress that this approach in its current form is only suitable for bundle-specific applications or other cases that aim to investigate connections between two specific regions. As a consequence, it cannot be combined with algorithms for whole-brain reconstructions at the current moment.

2.4.4 Future work

Although in this work we integrated the MLFT framework with the deterministic tractography, it can also be implemented for probabilistic tractography. In some probabilistic tractography methods such as iFOD2, for example, new directions are sampled at each propagation step from the fiber orientation distribution (concentrating around the peaks) only regarding peaks with an angular deviation lower than the pre-defined threshold (Figure 2.15). In this context, MLFT could be similarly applied to sample the propagation direction from the part of distribution outside the area conforming with the angular threshold when branching into the second level (Figure 2.15).

MLFT has shown promising results in healthy controls, but it remains unclear whether its performance will be maintained in presence of pathology especially with routinely acquired clinical data. Thus, evaluation of the algorithm in a clinical setting would also be beneficial.

It must be noted that in this work we did not focus on devising an approach for estimating the required number of levels based on convergence criteria, which might be useful for clinical translation. For this study, those settings were identified empirically. Experiments were performed with up to 3 levels, however, there was not much change observed between results with 2 and 3 levels. One of the possible future directions of this work could be to introduce microstructural information in
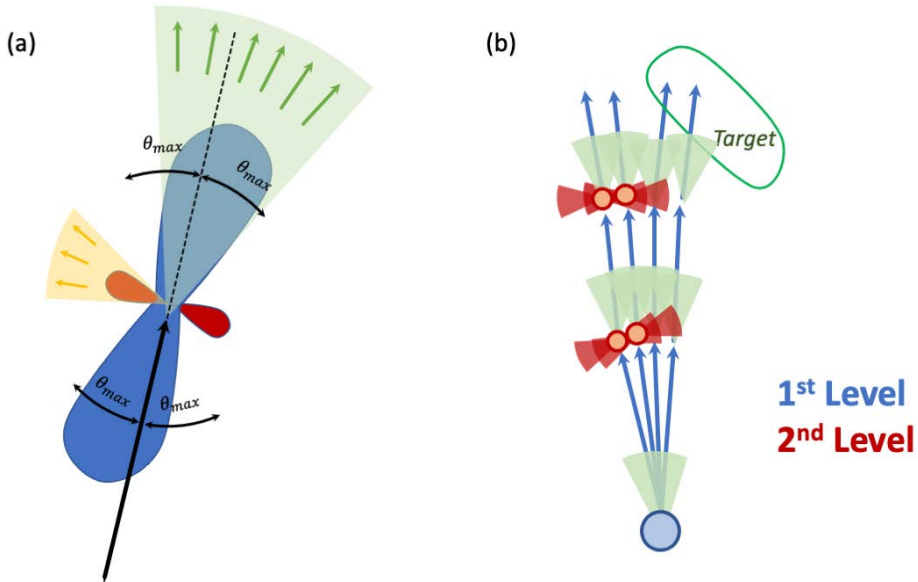
Figure 2.15: (a) In probabilistic tractography new step directions are sampled into the directions with higher probability (green arrows) and then also constrained with an angular threshold (θ_{max}). (b) Applying MLFT approach to probabilistic tractography at the second level would require sampling into the directions of the peak with deviation that is higher than the threshold (red area).

analogy to the dynamic seeding approach [61], which may allow for the automatic estimation of the number of levels, and which could facilitate the identification of valid branches.

Corticospinal tract reconstruction in patients with high-grade glioma

Abstract

While the diagnosis of high-grade glioma (HGG) is still associated with a considerably poor prognosis, neurosurgical tumor resection provides an opportunity for prolonged survival and improved quality of life for affected patients. However, successful tumor resection is dependent on a proper surgical planning to avoid surgery-induced functional deficits whilst achieving a maximum extent of resection (EOR). With diffusion magnetic resonance imaging (MRI) providing insight into individual white matter neuroanatomy, the challenge remains to disentangle that information as correctly and as completely as possible. In particular, due to the lack of sensitivity and accuracy, the clinical value of widely used diffusion tensor imaging (DTI)-based tractography is increasingly questioned.

We evaluated whether the recently developed multi-level fiber tracking (MLFT) technique can improve tractography of the corticospinal tract (CST) in patients with motor-eloquent HGGs. Forty patients with therapy-naïve HGGs (mean age: 62.6 ± 13.4 years, 57.5% males) and preoperative diffusion MRI [repetition time (TR)/echo time (TE): $5000/78ms$, voxel size: $2 \times 2 \times 2mm^3$, one volume at $b = 0s/mm^2$, 32 volumes at $b = 1000s/mm^2$] underwent reconstruction of the CST of the tumor-affected and unaffected hemispheres using MLFT in addition to deterministic DTI-based and deterministic constrained spherical deconvolution (CSD)-based fiber tractography. The brain stem was used as a seeding region, with a motor cortex mask serving as a target region for MLFT and a region of interest (ROI) for the other two algorithms.

Application of the MLFT method substantially improved bundle reconstruction, leading to CST bundles with higher radial extent compared to the two other algorithms (delineation of CST fanning with a wider range; median radial extent for tumor-affected vs. unaffected hemisphere – DTI: $19.46°$ vs. $18.99°$, $p = 0.8931$; CSD: $30.54°$ vs. $27.63°$, $p = 0.0546$; MLFT: $81.17°$ vs. $74.59°$, $p = 0.0134$). In addition, reconstructions by MLFT and CSD-based tractography nearly completely included respective bundles derived from DTI-based tractography, which was however favorable for MLFT compared to CSD-based tractography (median coverage of the DTI-based CST for affected vs. unaffected hemispheres – CSD: 68.16% vs. 77.59%, $p = 0.0075$; MLFT: 93.09% vs. 95.49%; $p = 0.0046$). Thus, a more complete picture of the CST in patients with motor-eloquent HGGs might be achieved based on routinely acquired diffusion MRI data using MLFT.

3.1   Introduction

Gliomas represent the most common malignant brain tumors in adults, with an average annual age-adjusted incidence rate of ~ 4.67 to 5.73 per 100,000 population [62,63]. Anaplastic astrocytoma and glioblastoma are the major high-grade glioma (HGG) entities and peak in elderly subjects. [62–64]. Overall prognosis is poor, with a median survival below 2 years [62,63,65]. HGGs can be regarded as chronic progressive diseases and typically show infiltrative growth behavior, which renders curative treatment almost impossible for the majority of affected patients [64,66].

Nowadays, the standard treatment approach in patients harboring HGGs is a combination of neurosurgical resection, extended focal radiotherapy, and adjuvant chemotherapy. [67–70] Nonetheless, multiple factors including histopathological characteristics, molecular tumor biology, as well as functional eloquence of the affected brain region contribute to individual therapy decision-making in clinical practice. [70,71] Regarding neurosurgical resection, a maximum extent of resection (EOR) has been associated with prolonged survival rates and better quality of life. [1, 2, 16, 72–75]. However, mostly depending on individual tumor location, achieving a maximum EOR can be in conflict with preserving specific functions, such as the ability to move or speak without constraints. Thus, the principle of contemporary brain tumor surgery aims at an optimum EOR whilst avoiding surgery-related functional decline as far as possible. [76, 77]

The gold-standard method for spatially resolved assessment of brain function is intraoperative direct electrical stimulation (DES), which can be applied as a strategy to guide neurosurgical resection and to avoid functional deficits in the course of tumor resection. [69,78–80] In addition to intraoperative DES, presurgical imaging is paramount to achieve an optimized onco-functional result. At the forefront of imaging techniques, multi-sequence magnetic resonance imaging (MRI) is applied to gather insights into spatial location, spread, and phenotyping of brain tumors [81–84]. Lately, diffusion tensor imaging (DTI) in particular has seen increasing relevance as it allows identifying and delineating subcortical white matter (WM) structures non-invasively [85–89]. In the neurosurgical context, DTI is frequently used for tracking of the corticospinal tract (CST), the main WM pathway subserving human motor function. The popularity of DTI can be explained by the low false-positive rate of tractography maps. [6] Yet, the approach tends to produce underrepresented fiber bundles. [5] Consequently, this causes an ongoing debate on whether conventional DTI methods are accurate and reliable enough to serve as a workable solution for delineating WM architecture in patients with glioma. [90–93] Specifically, one main criticism is that the brain's WM architecture harbors numerous fiber crossings and further complex geometrical configurations, including fiber branching, which are hard to resolve. [94,95]

While deterministic tractography with DTI is the most common preoperative approach, a variety of models has been proposed to overcome the overall limitations of DTI-based tractography and improve the reconstruction of WM fiber

organization as an attempt to further narrow the gap between imaging and reality, including diffusion kurtosis imaging and fiber orientation distribution (FOD)-based approaches using constrained spherical deconvolution (CSD) as the most prominent representative. [21, 25, 96] At the same time, although these models are more capable of disentangling fiber orientations, tractography algorithms commonly impose additional constraints that are set to achieve structurally plausible results, such as angular deviation and consideration of all the orientations as separate fibers. Consequently, either pathway propagation may be terminated, or a diverging branch may be pruned due to the angular limitations as well as related to spatial resolution constraints, which may artificially push the rate of false-negative findings. [20] Thus, the possibility of incorporating fiber bifurcations with high angular deviations, such as those observed for the human CST, remains neglected. Probabilistic algorithms that are supposed to improve reconstructions by not just propagating into the peak FOD direction but sampling each step from the FOD could compensate for the angular resolution of the FOD model and capture certain pathway bifurcations. A series of previous publications has shown the ability of probabilistic tractography to improve the extent of the bundles over DTI-based tractography while highlighting microstructural changes induced by the tumor. [97–99] However, usually direction samples are not drawn out of the whole FOD but from the segment defined by an angular deviation threshold. [48] This introduces a limitation to probabilistic methods that is using higher angular deviation thresholds helps in reconstructing more complete bundles while also increasing the false-positive rate. [6]

Against this background, we evaluate a method for improved fiber tractography of the CST in patients suffering from motor-eloquent HGGs, which aims to specifically tackle the issue of missing fiber branching of currently existing tractography procedures. We evaluate the multi-level fiber tracking (MLFT) approach proposed in Chapter 2. It adds branches to the pathways that have been previously reconstructed, but do not reach a predefined target region. Specifically, we hypothesize that the MLFT algorithm is capable of improving the reconstruction of the CST in the vicinity of a brain tumor when compared to conventionally used DTI-based tractography as well as tractography using CSD.

3.2   Methods

3.2.1   Study Design and Patient Inclusion

This study was approved by the local institutional review board and was conducted in accordance with the Declaration of Helsinki. The requirement for written informed consent was waived due to the study's retrospective design.

Patients who underwent brain MRI using a multi-sequence imaging protocol for brain tumors according to clinical indication were retrospectively identified in

the institutional Picture Archiving and Communication System (PACS). The time interval for PACS search ranged from February 2019 to February 2020 considering the time point of MRI acquisition. Inclusion criteria were 1) age above 18 years, 2) availability of preoperative 3-Tesla MRI including diffusion-weighted sequences, 3) diagnosis of a HGG (based on imaging findings and later confirmation by histopathological evaluation of biopsy probes or tumor tissue harvested during surgical resection), and 4) suspected motor-eloquent tumor location according to preoperative MRI (imaging suggesting infiltration or compression of anatomically suspected cortical motor-eloquent areas and/or suspected close proximity to the CST). The exclusion criteria were 1) artifacts due to implants or motion artifacts in imaging data according to visual image evaluation (e.g., non-diagnostic image quality due to patient movement during image acquisition), and 2) previous brain surgery.

Overall, 40 patients fulfilled the inclusion criteria and were considered for this study. Clinical details including demographics and final histopathological tumor grading were extracted from electronic health records of these patients.

3.2.2   Magnetic Resonance Imaging

Cranial MRI was performed in the preoperative routine setting. All imaging considered in this study was acquired on the same two 3-Tesla scanners (Achieva dStream or Ingenia; Philips Healthcare, Best, Netherlands) using a 32-channel head coil.

The standardized multi-sequence imaging protocol for brain tumors included a three-dimensional (3D) fluid attenuated inversion recovery (FLAIR) sequence (repetition time [TR]/echo time [TE]: $4800/277ms$, $1mm^3$ isovoxel covering the whole head), an axial T2-weighted sequence (TR/TE: $3396/87ms$, voxel size of $0.36 \times 0.36 \times 4mm^3$), a diffusion-weighted sequence (TR/TE: $5000/78ms$, voxel size of $2 \times 2 \times 2mm^3$, one volume at $b = 0s/mm^2$, 32 volumes at $b = 1000s/mm^2$), and a 3D T1-weighted turbo field echo (TFE) sequence (TR/TE: $9/4ms$, $1mm^3$ isovoxel covering the whole head) without and with application of a contrast agent using a dose of $0.2ml$ per kg body weight of gadoteric acid (Dotagraf $0.5mmol/ml$; Jenapharm GmbH & Co. KG, Jena, Germany). Further sequences not related to this study's analyses were acquired by default and used for radiological reporting and image-based diagnostics.

3.2.3   Data processing

Co-Registration and Segmentation

First, to avoid errors in the automated structural parcellation due to the presence of pathology and related anatomical distortion, lesion filling for the T1-weighted images was done prior to structural parcellation, which substitutes the

tumor volume in the image with data mimicking signal from the healthy tissue (either using noise or healthy tissue simulation). For robust parcellation, in this work we used automated Virtual Brain Grafting (VBG), which enables the generation of a virtual lesion-free T1-weighted image and structural parcellation using FreeSurfer recon-all. [46, 100] Lesion segmentation required for VBG was obtained fusing eight segmentation algorithms using majority voting from the Brain Tumor Segmentation (BraTS) toolkit. [101, 102] The BraTS toolkit relies on a multi-modal input (non-contrast and contrast-enhanced T1-weighted images, FLAIR images, and T2-weighted images) and produces segmentation masks that enclose the tumor core (necrotic center and contrast-enhancing tumor parts) and FLAIR-hyperintense zones (edema/tumor infiltration), which were further used to compute the respective volumes (by accumulating volumes of each voxel in the respective masks). [101, 102] Before performing segmentations, all MRI data were transferred to Montreal Neurological Institute (MNI) space (with an isotropic voxel size of 1 mm^3).

The diffusion-weighted MRI data of the individual patients were corrected for motion and eddy currents, and co-registered to the corresponding T1-weighted images using ExploreDTI (version 4.8.6; PROVIDI Lab, Utrecht, Netherlands). [39]. The FODs were estimated using recursive calibration of the response function [103]. We used a spherical harmonics order of $L_{max} = 6$. Motor cortex masks were assembled from precentral, postcentral, and paracentral lobule segmentations (Figure 3.1a) obtained with FreeSurfer (version 6.0.0; Laboratory for Computational Neuroimaging, Charlestown, MA, USA) [46] using the Desikan-Killiany atlas. [44] All image co-registrations and segmentations were visually inspected for quality and, in case of segmentations, manually corrected by a neuroradiologist when necessary.

Figure 3.1: (a) Motor cortex mask (red) was assembled using precentral, postcentral, and paracentral gyri as segmented using FreeSurfer. The motor cortex mask was used as a target region. (b) The seed region (green) was defined as a cross-section of the brain stem at the pontine level.

Fiber Tracking Algorithm

Three deterministic tractography approaches were used in this study to reconstruct the CST of both hemispheres: DTI-based tractography, CSD-based tractography,

and MLFT. DTI-based tractography was chosen since it is widely used in current
clinical practice. [15, 92] This algorithm propagates fiber streamlines into the main
direction of the estimated diffusion tensor. However, it leads to issues with
reconstructing pathways in certain complex situations (e.g., crossing or kissing
fibers) when the estimated diffusion becomes closer to isotropic and the main
tensor direction may not coincide with any of the underlying fiber orientations.
[94, 95] CSD-based tractography has improved the specificity compared to DTI-
based tractography given higher angular resolution and an ability to disentangle
more complex fiber configurations. [21, 25] During pathway propagation each time
the algorithm chooses an FOD peak that minimizes angular deviation from the
previous step. The CSD approach was included as it has shown to be capable of
adequately accounting for crossing fiber configurations, and it serves as a basis for
the MLFT algorithm.

As was shown in Chapter 2, the MLFT algorithm reconstructs bundles as
multi-level structures, with the exact number of levels defined by the user. Given a
seed and a target region, MLFT aims to iteratively improve bundle reconstruction
by adding pathways with high angulation reaching the target region. At each
iteration, MLFT propagates pathways from a set of seed points using deterministic
CSD-based tractography that takes every step into the direction of a FOD peak
the least deviating from the direction of the previous step. After propagation, the
points of the pathways that did not reach the target region are used as seed points
for the following iteration. Their initial directions are then defined as the peaks
of the corresponding FODs that were ignored during propagation. If a seed point
corresponds to multiple unused FOD peaks, it is duplicated to allow propagating
each of the alternative directions. The rest of the pathways reaching the target
region are forming a new level of the reconstruction. They are concatenated with
the segment of the pathway they branched from that originates from the prior seed
point set. This procedure is repeated for a predefined number of iterations. For
the CST reconstruction, two levels (iterations) were used in this study. Thus, by
extending the reconstruction with each new level, MLFT is attempting to account
for branching fibers. In Chapter 2 it was also shown to preserve topography of the
bundles.

Additionally, it can be noticed that the reconstructions performed with de-
terministic CSD-based tractography are essentially the first level of the MLFT
reconstructions. Thus, the extent of MLFT reconstructions will always at least
cover that of the CSD-based algorithm.

Tractography Setup

To reconstruct the CST within each hemisphere, the seed region was placed in
the single-slice transverse cross-section of the pontine level of the brain stem as
obtained from brain parcellations (Figure 3.1b). [19] Motor cortex masks assembled
from the segmentation of precentral, postcentral, and paracentral gyri of the

left and right hemisphere, respectively, were set as target regions for MLFT and as a region of interest (ROI) to filter the results of DTI- and CSD-based tractography (Figure 3.1a). Five seed points were sampled per voxel in the seed mask at a single-slice level in the superior part of the brain stem, ensuring that all the points were on the same transverse plane. The tractography step was set to half a voxel size, the angular threshold was set to $45°$ as in Chapter 2. For MLFT and CSD-based tractography the FOD peak threshold amplitude was set to 0.08, which was chosen empirically based on visual inspection of the results and with the aim to increase the volume of the reconstruction without introducing obvious false-positive pathways. For DTI-based tractography the fractional anisotropy (FA) threshold was set to 0.1. The number of iterations was set to 2 for MLFT. Additionally, due to reconstruction of CST branches for the left and right hemisphere from the same seed region in the brain stem, interhemispheric connections were filtered out. Additional experiments evaluating algorithms on fine-grained target regions are provided in the Supplementary Material.

3.2.4   Fiber Tracking Evaluation

Qualitative Assessment

Visual image evaluation was performed by a neuroradiologist (7 years of experience in neuroradiological imaging) using ExploreDTI. The reconstructed bundles were rendered in the same scene as the contrast-enhanced T1-weighted images for an interactive assessment of the course of the CST and its relation to the tumor.

Patients were pseudonymized during all visual image evaluations. In detail, datasets stemming from DTI-based tractography, CSD-based tractography, and MLFT were opened during three rounds of evaluation, with each round randomly including one of those tractography results per patient. Between each round of assessment, an interval of at least two weeks was established to minimize recall bias. Both the tumor-affected and unaffected hemispheres were separately evaluated per patient. First, the course of the reconstructed CST through anatomical landmarks known to be key for the descending CST (ipsilateral internal capsule and cerebral crus at the level of the brain stem) was assessed in binary fashion (CST passing through/not passing through internal capsule and cerebral crus). Second, for tractography within the tumor-affected hemisphere, the neuroradiologist assessed whether the reconstructed CST appeared to be unaffected (no contact and no visually identifiable deviation), spatially deviated, infiltrated or split, or destroyed (entire or partial disintegration of the CST) due to the tumor mass, similar to previous work on qualitative evaluation of fiber tract anatomy. [104]

Quantitative Assessment

Quantitative assessment of the CST bundles reconstructed with DTI-based, CSD-based tractography, and MLFT was performed, including radial extent and coverage of reconstructed fibers. The radial extent (in °) of the CST was calculated to show how much of the motor cortex is covered, which was achieved by computing the size of the segment of the coronal motor mask projection covered by the CST. Thus, the motor mask projection defines an arc of 90°, and the overlap of the bundle visitation mask on the motor cortex defines segments on the arc that constitute the radial extent. The difference in radial extents of the bundles reconstructed in tumor-affected and unaffected hemispheres was compared. Outliers in the difference distribution were detected as patients falling into the distribution tails and accounting for about 5% of the distribution. The threshold for the detection was calculated using the 2σ rule, where σ is the standard deviation (SD).

Given its wide use in clinical routine, DTI-based tractography was considered a baseline of comparison for the assessment of the algorithms regarding bundle trajectory. Thus, in order to assess the coherence of the CSD-based tractography and MLFT reconstructions with the DTI-based tractography results, coverage of the bundles generated with DTI-based tractography by the ones generated with CSD and MLFT was calculated. For calculation, binary visitation masks were created of the reconstructed bundles (with voxels being set to 1 if at least one pathway passed through it). Then, the part of the DTI-reconstructed bundle's mask intersecting with corresponding masks of the MLFT and the CSD-based reconstructions was calculated (in %, where 90% DTI coverage by MLFT would mean that 90% of the CST volume reconstructed by DTI-based tractography is also included in the respective reconstructed bundle when MLFT is used as the tractography algorithm in the same patient). The masks consisted of the voxels visited by the corresponding bundle (voxel contains at least one pathway point). All computations for quantitative image assessment were performed using in-house developed MATLAB scripts (version R2018b; The MathWorks Inc., Natick, MA, USA).

3.2.5 Statistics

For statistical data analyses, SPSS (version 26.0; IBM SPSS Statistics for Windows, IBM Corp., Armonk, NY, USA) and SciPy library [version 1.3.1 [105]] were used. In all statistical tests a significance level of $\alpha = 0.05$ was used.

Descriptive statistics included mean $\pm$ SD, ranges, and absolute or relative frequencies. For qualitative image assessment in the tumor-affected hemisphere, Chi-squared tests were conducted to test for differences in the spatial characteristics of the CST (unaffected, spatially deviated, infiltrated/split, or destroyed) between DTI-based tractography, CSD-based tractography, and MLFT. For quantitative

image assessment, the tractography algorithms were first compared to each other based on the radial extents of the reconstructions, separately for the unaffected and tumor-affected hemispheres and for the right versus left hemispheres, using two-sided Wilcoxon signed-rank tests. Furthermore, Wilcoxon signed-rank tests were used to compare the radial extents achieved by the same algorithm in affected and unaffected hemispheres, respectively.

Additionally, the coverage of the DTI-based reconstruction of the CST by CSD-based tractography and MLFT was compared for unaffected and tumor-affected hemispheres using two-sided Wilcoxon signed-rank tests. This allowed to assess if the presence of the tumor and related mass effects caused a significant change in the results of MLFT and CSD-based tractography compared to DTI-based tractography for tract coverage. In addition, correlations between the ratio of DTI-based reconstructions of the CST covered by CSD-based tractography or MLFT with the tumor core volumes or FLAIR-hyperintensity zone volumes were calculated using Pearson correlation coefficients.

3.3   Results

3.3.1   Patient cohort

Forty patients (mean age: 62.6 ± 13.4 years, age range: $29.5 - 85.9$ years, 17 females and 23 males) with a diagnosis of HGG and suspected motor-eloquent tumor location were included. Table 3.1 provides further cohort details.

3.3.2   Qualitative Assessment

Representative exemplary cases for CST reconstruction by DTI-based tractography, CSD-based tractography, and MLFT are shown in Figures 3.2, 3.3. The reconstructed CST passed through the internal capsule and cerebral crus as key anatomical landmarks for both hemispheres of all enrolled patients.

The reconstructed CST bundle was unaffected by or not in contact with the tumor mass in $n = 15$, 8, and 4 patients for DTI-based tractography, CSD-based tractography, and MLFT, respectively, and did not fulfill the criteria of a disintegrated course in any of the patients. Furthermore, the reconstructed CST bundle was deviated in $n = 24$, 26, and 22 patients, respectively. It appeared to be infiltrated/split in $n = 1$, 6, and 14 patients when using DTI-based tractography, CSD-based tractography, or MLFT, respectively. There was a statistically significant difference in these spatial characteristics of the CST depending on the tractography approach chosen ($p = 0.0006$).

Item		Value
Age		62.6 ± 13.4
(years; mean$\pm$SD & range)		$(29.5 - 85.9)$
Sex	Male	57.5
(% of patients)	Female	42.5
Affected hemisphere	Left	40.0
(% of patients)	Right	60.0
Surgical procedure performed	Biopsy	22.5
	Resection	67.5
(% of patients)	Resection & intraoperative RTX	10.0
Extent of resection	STR	25.8
(% of patients)	GTR	74.2
Tumor grade	WHO grade III	12.5
(% of patients)	WHO grade IV	87.5
Tumor core volume		47997.4 ± 39098.9
(mm^3; mean$\pm$SD & range)		$(2.582 - 170576)$
Volume of FLAIR-hyperintense zone		64727.3 ± 48394.8
(mm^3; mean$\pm$SD & range)		$(4625 - 184127)$

Table 3.1: Characteristics of the study cohort. SD, standard deviation: WHO, World Health Organization: STR, subtotal resection: GTR, gross total resection; RTX, radiotherapy.

3.3.3 Quantitative Assessment

Radial Extent

The radial extents of the CST branches reconstructed with the three tractography algorithms are presented in Figures 3.4, 3.5. The MLFT algorithm consistently provides increased radial extent when compared to both CSD-based and DTI-based tractography in all patients. In addition, when comparing radial extents between reconstructions from the three different tractography algorithms, results were statistically significant throughout (DTI vs. CSD/DTI vs. MLFT/CSD vs. MLFT: $p < 0.05$ each for tumor-affected vs. unaffected as well as right vs. left hemispheres; Table 3.2).

Each of the algorithms produced CST reconstructions with higher median radial extent of the reconstructions for the tumor-affected hemispheres as compared to the unaffected hemispheres, with a statistically significant difference only for MLFT (median radial extent for tumor-affected vs. unaffected hemisphere – DTI: 19.46° vs. 18.99°, $p = 0.8931$; CSD: 30.54° vs. 27.63°, $p = 0.0546$; MLFT: 81.17° vs. 74.59°, $p = 0.0134$). Furthermore, the differences in radial extents of the CST bundles in tumor-affected and unaffected hemispheres were compared (Figure 3.6). Using 2σ, three outliers were identified (patients #8, #10, and #37), who were all characterized by extensive mass effect that caused deformation of the CST bundle within the tumor-affected hemisphere, and to a lesser extent also a deviation of the CST within the unaffected hemisphere (Figure 3.7). Midline shifts can be
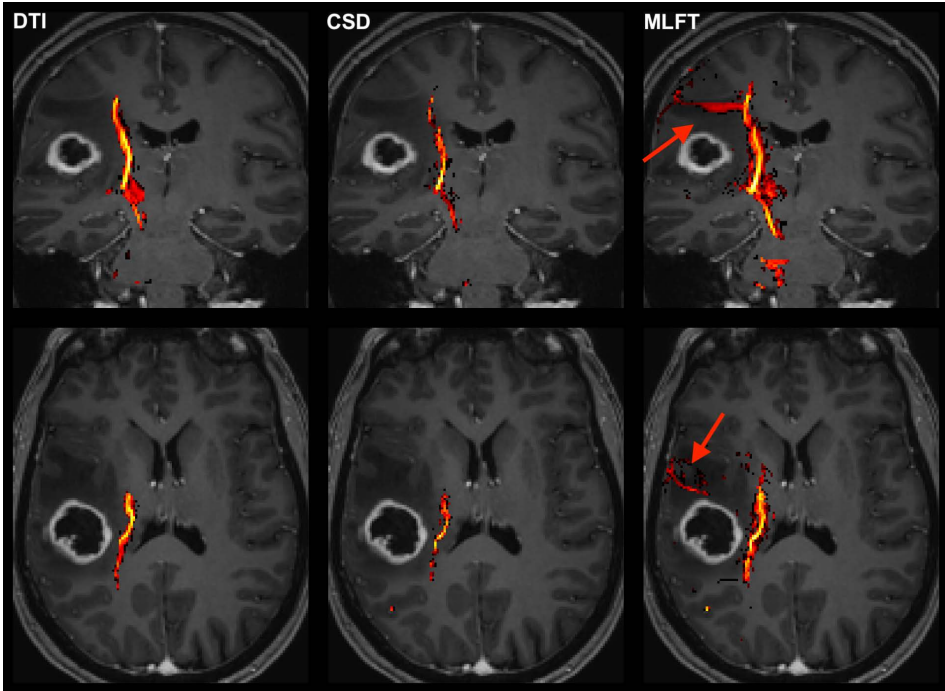
Figure 3.2: Exemplary case for reconstruction of the corticospinal tract (CST) depending on the algorithm used for tractography. This illustrative exemplary case of a patient suffering from a right-sided high-grade glioma (HGG) shows the reconstructed CST within the tumor-affected hemisphere as derived from diffusion tensor imaging (DTI)-based tractography, constrained spherical deconvolution (CSD)-based tractography, and multi-level fiber tracking (MLFT). The CST reconstructions are fused with axial and coronal contrast-enhanced T1-weighted images to outline the lesion-to-CST relationship as well as the CST volume and course. The MLFT approach enables fiber tracking with a larger radial extent, thus displaying also fanning of the CST and fibers with acute angles (red arrow).

observed in these three outliers.

Coverage of DTI

The results on comparing the coverage of DTI-based reconstructions by the corresponding CSD-based and MLFT-based reconstructions are depicted in Figure 3.8. MLFT provides a higher fraction of coverage of the DTI reconstruction results of the CST when compared to CSD.

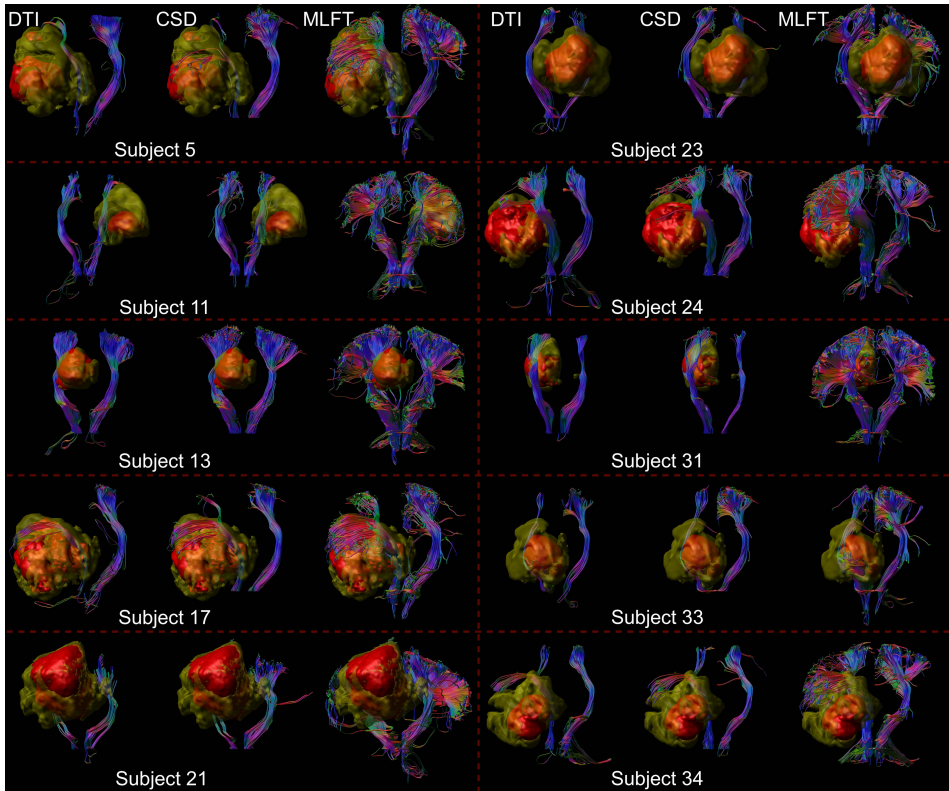Both CSD-based and MLFT results more clearly coincide with DTI-based

Figure 3.3: Comparison of reconstructions of the corticospinal tract (CST) depending on the algorithm chosen for tractography. This figure shows reconstructions of the CST within the tumor-affected and unaffected hemispheres in a subset of 10 patients from the cohort, using diffusion tensor imaging (DTI)-based tractography, constrained spherical deconvolution (CSD)-based tractography, and multi-level fiber tracking (MLFT). The tumor core is shown as a red volume, the hyperintense zone in fluid attenuated inversion recovery (FLAIR) sequences is shown as a yellow volume. While CSD-based tractography provides reconstructions comparable to DTI-based tractography, MLFT is able to improve depiction of the extent of the CST fanning of both tumor-affected and unaffected hemispheres.

reconstructions in case of the unaffected hemispheres (median coverage for affected vs. unaffected hemisphere – CSD: 68.16% vs. 77.59%, $p = 0.0075$; MLFT: 93.09% vs. 95.49%; $p = 0.0046$), while the reconstructions in the tumor-affected hemisphere are characterized by a higher mismatch. Yet, for the MLFT median coverage is $> 90\%$ for both the unaffected and tumor-affected hemisphere, which contrasts with the CSD-based reconstruction with a median coverage of $< 80\%$.

Radial Extent	Mean±SD, (°)			Range, (°)			p-value		
Hemisphere	DTI	CSD	MLFT	DTI	CSD	MLFT	CSD-DTI	MLFT-DTI	MLFT-CSD
Right	21.9 ± 11.7	30.0 ± 14.6	73.8 ± 16.1	$5.28 - 71.53$	$11.68 - 77.75$	$23.65 - 90.45$	$5.5 * 10^{-5}$	$3.6 * 10^{-8}$	$3.6 * 10^{-8}$
Left	20.1 ± 8.3	28.9 ± 10.5	67.8 ± 18.3	$1.75 - 39.84$	$5.97 - 51.72$	$22.31 - 90.07$	$5.3 * 10^{-7}$	$3.6 * 10^{-8}$	$3.6 * 10^{-8}$
Affected	21.6 ± 11.7	32.8 ± 14.6	74.8 ± 15.6	$5.28 - 71.53$	$11.68 - 77.75$	$23.65 - 89.41$	$1.1 * 10^{-6}$	$3.6 * 10^{-8}$	$3.6 * 10^{-8}$
Unaffected	20.3 ± 8.0	26.1 ± 8.9	66.7 ± 17.9	$1.75 - 36.22$	$5.97 - 51.72$	$22.31 - 90.45$	$1.5 * 10^{-5}$	$3.6 * 10^{-8}$	$3.6 * 10^{-8}$

Table 3.2: Radial extent of fiber reconstructions. This table shows the mean±SD and ranges for the radial extents of CST reconstructions with the three different algorithms used (DTI-based tractography, CSD-based tractography, and MLFT). Discrimination is made between left and right hemispheres as well as tumor-affected and unaffected hemispheres. P-values were computed for the comparisons of radial extents derived from the different algorithms (Wilcoxon signed-rank paired tests with significance level $\alpha = 0.05$). Abbreviations: CST=corticospinal tract; SD=standard deviation; DTI=diffusion tensor imaging; CSD= constrained spherical deconvolution; MLFT=multi-level fiber tracking.

The two patients that had the lowest DTI coverage (lower than 75%) in the tumor-affected hemisphere by the MLFT reconstructions were subjects with extensive mass effects and high tumor volume, namely patients #5 and #17. The lowest DTI coverage achieved with CSD-based tractography is also attributed to patient #5. For these patients, tumor volumes as well as volumes of the FLAIR-hyperintense zones ranged in the upper quartile.

The correlation coefficients of the DTI coverage by CSD-based tractography or MLFT with the tumor core (necrotic center and contrast-enhancing tumor parts) and FLAIR-hyperintense zones are shown in Table 3.3. There were statistically significant negative correlations between the volume of the FLAIR-hyperintense zone and the DTI coverage (CSD: $r = -0.52$, $p = 0.0006$; MLFT: $r = -0.52$, $p = 0.0005$). Likewise, there were statistically significant negative correlations between the volume of the tumor core plus the volume of the FLAIR-hyperintense zone and DTI coverage (CSD: $r = -0.48$, $p = 0.0018$; MLFT: $r = -0.47$, $p = 0.0021$).

	CSD coverage of DTI		MLFT coverage of DTI	
	r	p-value	r	p-value
Tumor Core Volume	-0.25	0.12	-0.24	0.14
Volume of FLAIR-hyperintense zone	-0.52	< 0.01	-0.52	< 0.01
Tumor Core Volume + FLAIR-hyperintense zone	-0.48	< 0.01	-0.47	< 0.01

Table 3.3: Correlations for coverage. This table shows the Pearson correlation coefficient (r) and related p-values for the correlations between tumor core volume, volume of FLAIR-hyperintense zone, and volume of tumor core plus FLAIR-hyperintense zone and coverage of the DTI-derived CST for reconstructions using CSD-based tractography or MLFT, respectively(significance level $\alpha = 0.05$). DTI, diffusion tensor imaging: CSD, constrained spherical deconvolution; MLFT, multi-level fiber tracking: FLAIR, fluid attenuated inversion recovery.
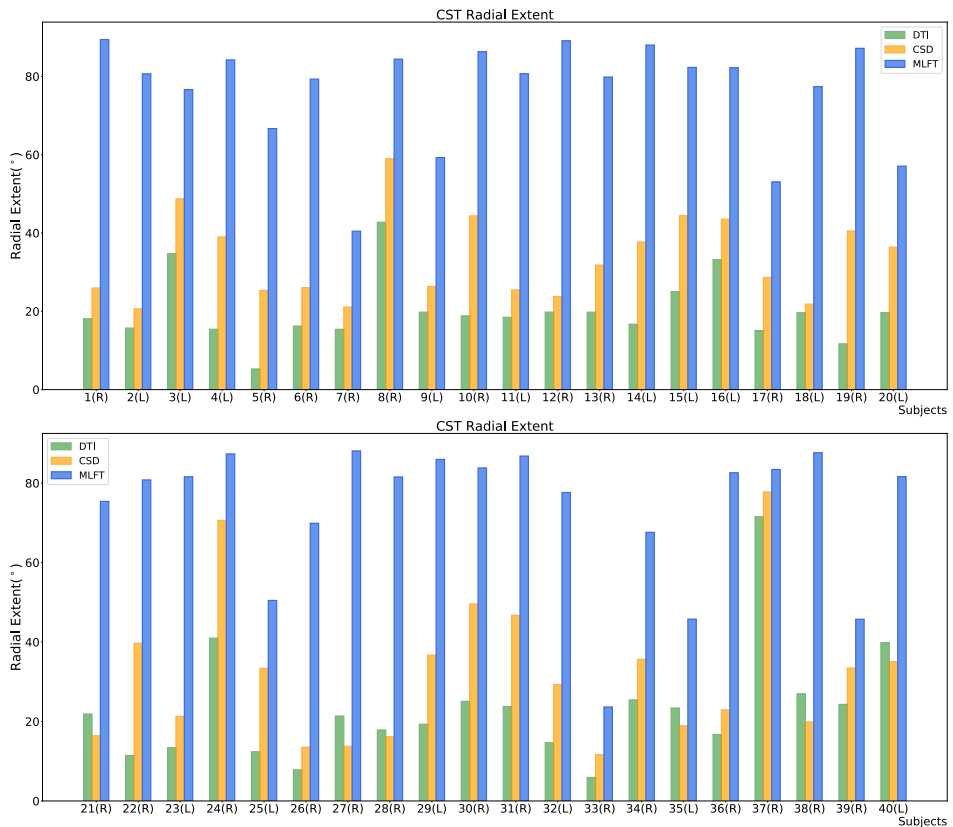
Figure 3.4: Comparison of the radial extent of the corticospinal tract (CST) branches of the tumor-affected hemispheres. This figure illustrates the radial extent for CST reconstruction using diffusion tensor imaging (DTI)-based tractography (green), constrained spherical deconvolution (CSD)-based tractography (orange), and multi-level fiber tracking (MLFT; blue). The hemisphere affected by the tumor per patient is indicated next to the subject index (L – left, R – right). Using MLFT led to CST reconstructions with larger radial extent in all patients.

3.4 Discussion

In this work we evaluated a novel tractography algorithm, MLFT, to achieve improved reconstruction of the CST in patients with motor-eloquent HGG. The MLFT algorithm was compared to deterministic DTI-based and deterministic CSD-based tractography of the CST of both hemispheres. The main findings are as follows: 1) the algorithm chosen for tractography had significant impact on the spatial course, volume, and shape of the CST, with MLFT-based recon-
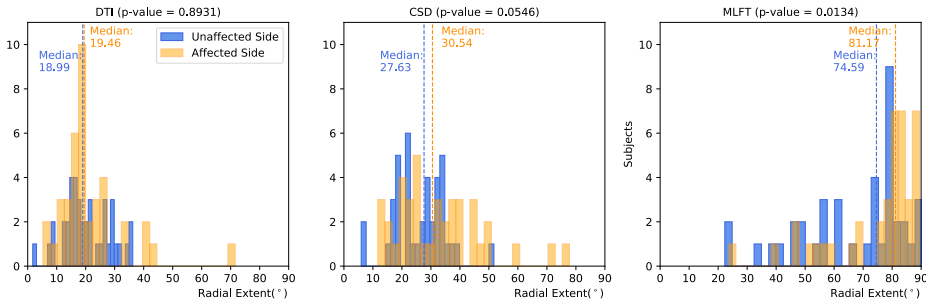
Figure 3.5: Comparison of the radial extent of the corticospinal tract (CST) branches. This figure shows the radial extents (with median values as vertical dashed lines) for the CST reconstructions derived from diffusion tensor imaging (DTI)-based tractography, constrained spherical deconvolution (CSD)-based tractography, and multi-level fiber tracking (MLFT). Columns for the tumor-affected hemispheres are displayed in orange, columns for the unaffected hemispheres are depicted in blue. The affected hemispheres show higher radial extent in case of each of the used tractography algorithms. The p-values are derived from comparisons between hemispheres per tractography algorithm (Wilcoxon signed-rank paired tests with significance level $\alpha = 0.05$).

structions showing significantly higher radial extents; 2) compared to deterministic CSD-based tractography, MLFT showed higher coincidence with the DTI-based reconstructions, with a median coverage of $> 90\%$ for both the tumor-affected as well as unaffected hemispheres; and 3) coverage of the CST as tracked by the DTI-based algorithm was significantly negatively associated with tumor-related mass effects (as estimated by volumes of tumor core and FLAIR-hyperintense zones) for both the CSD-based algorithm and MLFT.

Tractography of WM structures such as the CST is frequently employed for preoperative planning and intraoperative resection guidance in patients with intracranial neoplasms, using primarily DTI-based approaches. [85–89] However, DTI-based tractography has several known limitations that may hamper value for clinical applications, including its limited ability to resolve geometrically complex situations such as crossing or kissing fibers. [94, 95] Previous research has shown that using more advanced techniques, such as q-ball and CSD-based fiber tractography, may lead to improved results. [93, 106, 107]. In turn, the proposed MLFT algorithm is developed from CSD-based tractography and similarly propagates fiber pathways based on FOD peaks. However, unlike CSD-based tractography, MLFT assumes that FOD peaks represent not only fiber crossings, but also indicate fiber branching or high-angular deviation (see Chapter 2). Without prior anatomical knowledge, such an approach would be at risk of generating multiple false-positive streamlines, which needs to be avoided particularly for ultimate
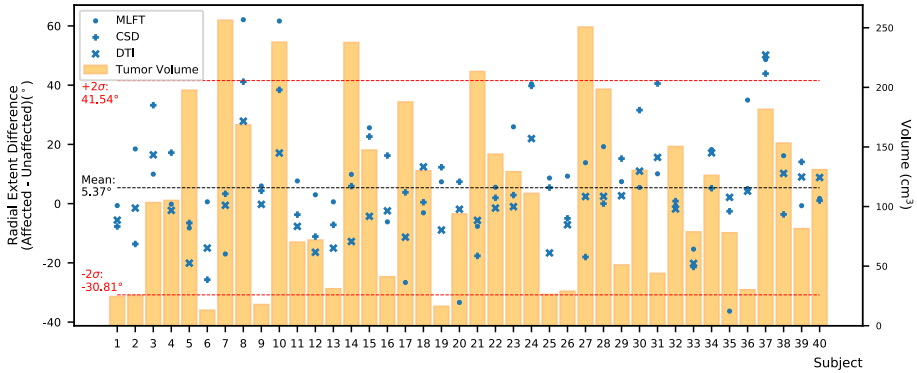
Figure 3.6: Differences between the radial extent of tumor-affected and unaffected hemispheres. This figure shows the radial extent differences in relation to combined tumor and FLAIR-hyperintense zone volumes (orange) using the mean (black dashed line) with ± 2 standard deviation (SD, provided as σ; red dashed lines) to identify potential outliers. Circles represent data points for the corticospinal tract (CST) as derived from multi-level fiber tracking (MLFT), while + represents data points derived from constrained spherical deconvolution (CSD)-based tractography and $\times$ represents data points stemming from diffusion tensor imaging (DTI)-based tractography. The outliers with positive radial extent difference are of most interest as they show unexpected behavior with higher radial extent in the tumor-affected hemisphere.

clinical applicability. In order to prevent a high false-positive rate, MLFT requires well-defined target and seed regions, and if certain pathways do not enter the target area our algorithm checks if any deviation at the previous points would allow reaching the target region. Hence, using the algorithm gives some control over specificity while improving sensitivity.

Reconstructions of the CST using MLFT consistently showed the highest radial extent when compared to DTI- or CSD-based tractography (Figure 3.3). On average, CSD-based tractography achieved higher radial extent than the DTI-based algorithm (Table 3.2), while in some individual cases DTI-based tractography outperforms the CSD algorithm for this metric (Figure 4). Yet, MLFT provided CST branches with higher radial extents even for the tumor-affected hemispheres, which may indicate that a more complete reconstruction of particularly highly angulated parts of the CST close to its origin becomes possible when using MLFT (Figures 3.4, 3.5). Indeed, based on simulations and preliminary in-vivo imaging in a cohort of healthy subjects, presented in Chapter 2, it has been suggested that the fanning close to the motor cortex can be well delineated with MLFT. Considering the potential value of a broader fanning and reconstruction of laterally coursing
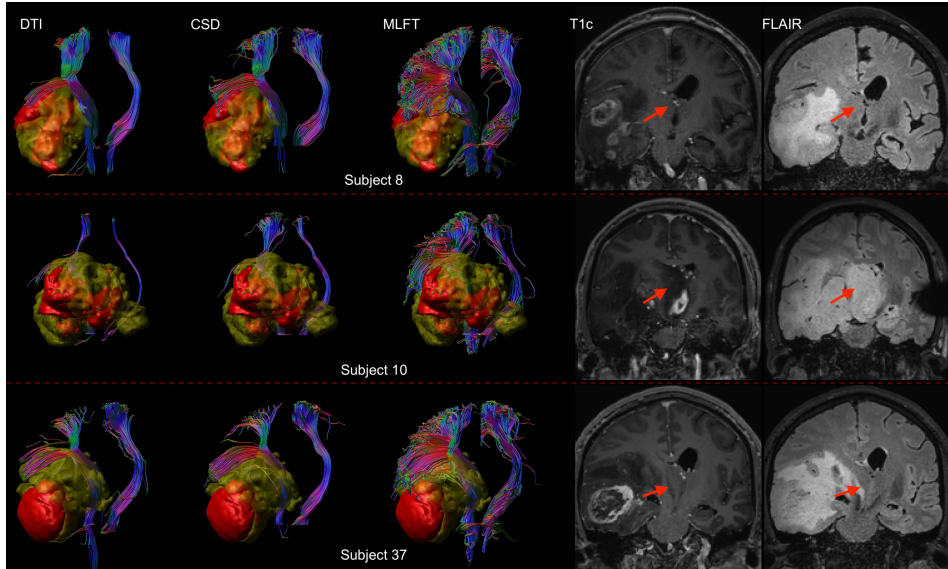
Figure 3.7: Comparison of the radial extent of the corticospinal tract (CST) branches. This figure shows the radial extents (with median values as vertical dashed lines) for the CST reconstructions derived from diffusion tensor imaging (DTI)-based tractography, constrained spherical deconvolution (CSD)-based tractography, and multi-level fiber tracking (MLFT). Columns for the tumor-affected hemispheres are displayed in orange, columns for the unaffected hemispheres are depicted in blue. The affected hemispheres show higher radial extent in case of each of the used tractography algorithms. The p-values are derived from comparisons between hemispheres per tractography algorithm (Wilcoxon signed-rank paired tests with significance level $\alpha = 0.05$).

fiber pathways, MLFT-derived reconstructions may be of merit since especially marginal fibers can be at risk for damage when aiming at a maximized EOR during surgery of motor-eloquent HGGs.

When comparing radial extents of tumor-affected and unaffected hemispheres, the observed differences are mostly comparable across the algorithms (Figure 3.6). Further, we separately explored the outliers with values above the $mean + 2\sigma$, given that they were of most interest, while any cases below the $mean - 2\sigma$ were considered in the range of an expected result. As the unaffected hemisphere apparently does not show the same changes in microstructure related to a tumor, the CST extent there should be at least comparable. Patients with considerable radial extent differences (above the 2σ threshold) are all characterized by mass effects extensive enough to cause midline shift and introduce deformations to the bundle in unaffected hemispheres (Figure 3.7), while the opposite is not always
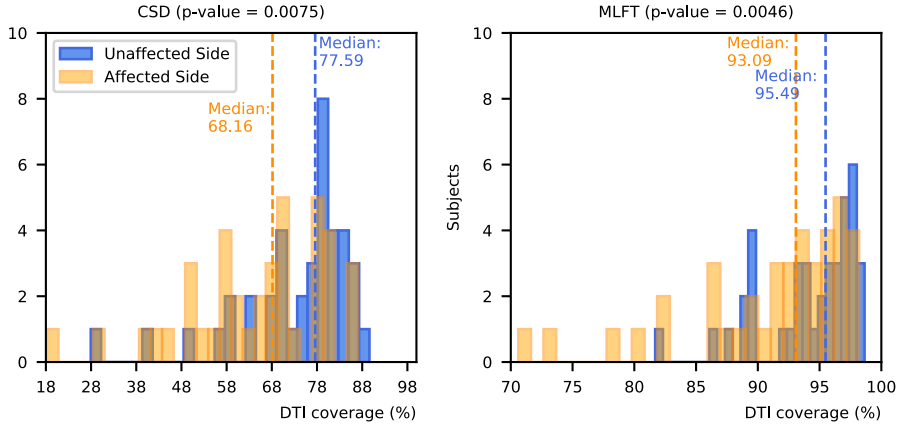
Figure 3.8: Comparison of coverage for corticospinal tract (CST) branches. This figure shows the coverage (with median values as vertical dashed lines) of the CST reconstructions derived from diffusion tensor imaging (DTI)-based tractography by constrained spherical deconvolution (CSD)-based tractography or multi-level fiber tracking (MLFT). Columns for the tumor-affected hemispheres are displayed in orange, columns for the unaffected hemispheres are depicted in blue. The affected hemispheres show lower coverage compared to the tumor-unaffected hemispheres. The p-values are derived from comparisons between hemispheres per tractography algorithm (Wilcoxon signed-rank paired tests with significance level $\alpha = 0.05$).

true. Depending on the distinct location of the tumor, midline shift may not lead to higher radial extent of the CST in the unaffected hemisphere; for instance, in cases of a more anterior tumor location and midline shift occurrence, no significant alteration was observed in radial extents. Regarding the reasons for the occurred differences, lateral components of the reconstructed CST pathways might be re-oriented as a result of WM compression causing smoothing of the acute angles of the fibers, which allowed the tractography algorithms to reconstruct them. Similarly, the CST pathways in the unaffected hemisphere could have been compressed and deviated in such a way that the angular resolution of the acquisition would not allow to resolve all fiber orientations properly, given that the acquired sequence only included 32 directions by default. In this regard, increasing the order of spherical harmonics used to estimate FODs would also increase the angular resolution, potentially solving the issue. [21] Yet, this would require inclusion of a higher number of gradient directions in the sequence. [108] At the same time, MLFT already reconstructs pathways closer to the tumor (Figure 3.2), hinting at potentially small tumor-to-CST distances that may exert impact on neurosurgical planning and have implications for patient outcome in terms of motor function

and avoidance of surgery-related functional decline.

While the general trajectory and shape of the DTI-based reconstructions tend to be maintained by both MLFT and CSD-based tractography, MLFT improves the coverage of CST reconstructions as provided by DTI-based tractography over those taken from the CSD algorithm (Figure 3.8). Notably, the median coverage of DTI-based CST reconstructions by the CST as delineated with MLFT was higher than 90% for both tumor-affected and unaffected hemispheres. This indicates that the approach does not considerably increase the false-negative rate, while performing better than the CSD algorithm that provides a median coverage below 80%. At the same time, the coverage of the DTI-based CST reconstruction by MLFT as well as CSD-based tractography is inversely correlated to measures for tumor-related mass effects (as estimated by volumes of tumor core and FLAIR-hyperintense zones), which might reflect the effect of tumor-induced WM changes on the estimated orientation distribution by either of the used models (Table 3.3). However, the question arises which method comes closest to the in-vivo course and architecture of the CST. The gold standard to test this would be intraoperative DES, which has not been applied to evaluate CSD or MLFT results because of this study's retrospective design. Yet, there seems high agreement in neurosurgical oncology that techniques should move beyond DTI-based tractography to improve accuracy of tracking results. [90–93]

One aspect that may further improve tractography using the MLFT algorithm is to combine it with techniques that provide function-based ROIs for seeding. In this regard, previous work has used activation maps derived from functional MRI for ROI placements. [109–111] More recently, motor maps derived from navigated transcranial magnetic stimulation (nTMS) have been used for ROI placements. [4, 112–116] Of note, it has been demonstrated that nTMS facilitates optimized tracking results for the CST, particularly when the primary motor cortex was in close vicinity of a brain tumor, suggesting that nTMS may be considered the method of choice to achieve proper ROI placements for CST tractography using DTI. [115] Comparisons between the three algorithms using nTMS motor maps for seeding may help identify parts of the CST that are underrepresented by DTI- or CSD-based tractography but are evidently connected to the primary motor cortex, which might in particular include fibers with acute angles that could be better delineated with the MLFT method. Additionally, subcortical language network analysis using nTMS-defined ROIs could be part of future work, as to date it has predominantly been performed with DTI-based tractography. [112, 117–119]

The main limitation of the MLFT method is related to the accuracy of the estimated FODs in the WM. In a clinical setting neither the number of acquired directions nor b-values are routinely set high, and the accuracy of the fitted diffusion models may therefore be hampered, as the FODs have to be represented by lower-order spherical harmonics. Additionally, the FOD algorithm used does not estimate separate response functions for different tissues. [103] An acquisition with multiple diffusion weightings (e.g., multi-shell imaging) would allow to use

FOD estimation algorithms that are capable of differentiating multiple tissues. [120] Another important limitation of this study is the absence of a correlation of the tractography results derived from CSD and MLFT to findings of intraoperative DES, as it would allow estimation of the sensitivity and specificity rates of these tractography algorithms. This is due to the study's retrospective character, while conventionally used DTI-based tractography for delineation of the CST has, however, been performed and considered for presurgical planning and intraoperative guidance within the scope of the standard of clinical care.

3.5 Conclusion

The results of this work suggest that tractography of the CST in patients harboring motor-eloquent HGGs may be improved using the proposed MLFT method. This advancement of the CSD principle enabled delineation of the CST with significantly increased radial extent for fibers close to the motor cortex, while maintaining coincidence with DTI-reconstructed CST bundles.

Supplementary material

Target region from finer brain parcellation

Using FreeSurfer-based multi-scale parcellation [121], we have segmented the pre-central gyrus subdividing the superior precentral and lateral precentral gyri (Figure 3.9). After that tractography was performed with the same settings as the experiments from the main manuscript. The comparisons of the radial extents for each new target region of each hemisphere are presented in Figures 3.10, 3.11, 3.12, 3.13. MLFT provided reconstructions with a radial extent covering most of the motor cortex in almost all the cases. Conversely, DTI- and CSD-based algorithms repeatedly failed to reconstruct pathways reaching the precentral gyri (Figures 3.12, 3.13, 3.15). At the same time, DTI- and CSD-based reconstructions are often comparable to those of MLFT when targeting the superior precentral gyrus, (Figures 3.10, 3.11, 3.14). Interestingly, DTI-based tractography reconstructed bundles targeting the superior part of the precentral cortex with higher extent in certain cases as compared to CSD-based reconstructions. While MLFT achieved superior performance to deterministic DTI- and CSD-based reconstructions when using the lateral part of the precentral cortex as the target region, some false-positive pathways may be observed in the MLFT reconstructions (Figure 3.15). Those pathways are primarily branching from pathways that propagate towards superior precentral part during the first iteration, which is not part of the target region in this case. When using the whole motor cortex as the target region (as presented in the main manuscript), these pathways would not have been used for seeding at the second iteration having reached their destination, thus highlighting the importance of the adequate choice of the target region.
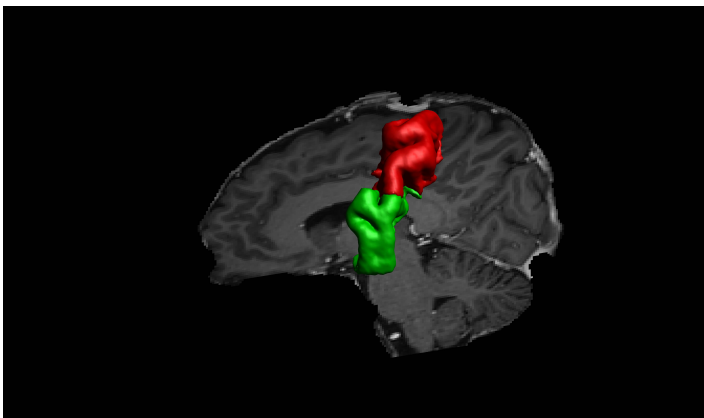

Figure 3.9: Precentral gyrus was subdivided into superior (red) and lateral (green) parts for the experiments exploring the effect of smaller target regions.

Figure 3.10: Comparison of the radial extent of the corticospinal tract (CST) sub-bundle reaching the superior part of the precentral cortex in the left hemisphere. This figure illustrates the radial extent for the reconstructions using diffusion tensor imaging (DTI)-based tractography (green), constrained spherical deconvolution (CSD)-based tractography (orange), and multi-level fiber tracking (MLFT; dark blue). The maximum extent that is the extent of the target cortex part is depicted in light blue.

Figure 3.11: Comparison of the radial extent of the corticospinal tract (CST) sub-bundle reaching the superior part of the precentral cortex in the right hemisphere. This figure illustrates the radial extent for the reconstructions using diffusion tensor imaging (DTI)-based tractography (green), constrained spherical deconvolution (CSD)-based tractography (orange), and multi-level fiber tracking (MLFT; dark blue). The maximum extent that is the extent of the target cortex part is depicted in light blue.
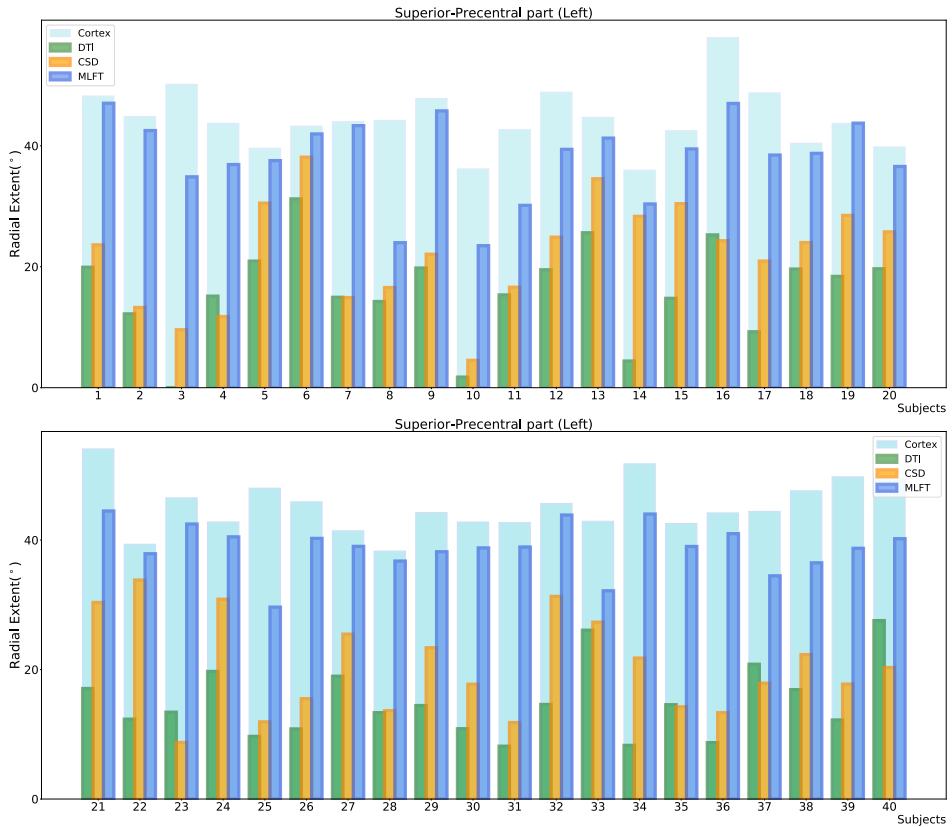
Figure 3.12: Comparison of the radial extent of the corticospinal tract (CST) sub-bundle reaching the lateral part of the precentral cortex in the left hemisphere. This figure illustrates the radial extent for the reconstructions using diffusion tensor imaging (DTI)-based tractography (green), constrained spherical deconvolution (CSD)-based tractography (orange), and multi-level fiber tracking (MLFT; dark blue). The maximum extent that is the extent of the target cortex part is depicted in light blue.
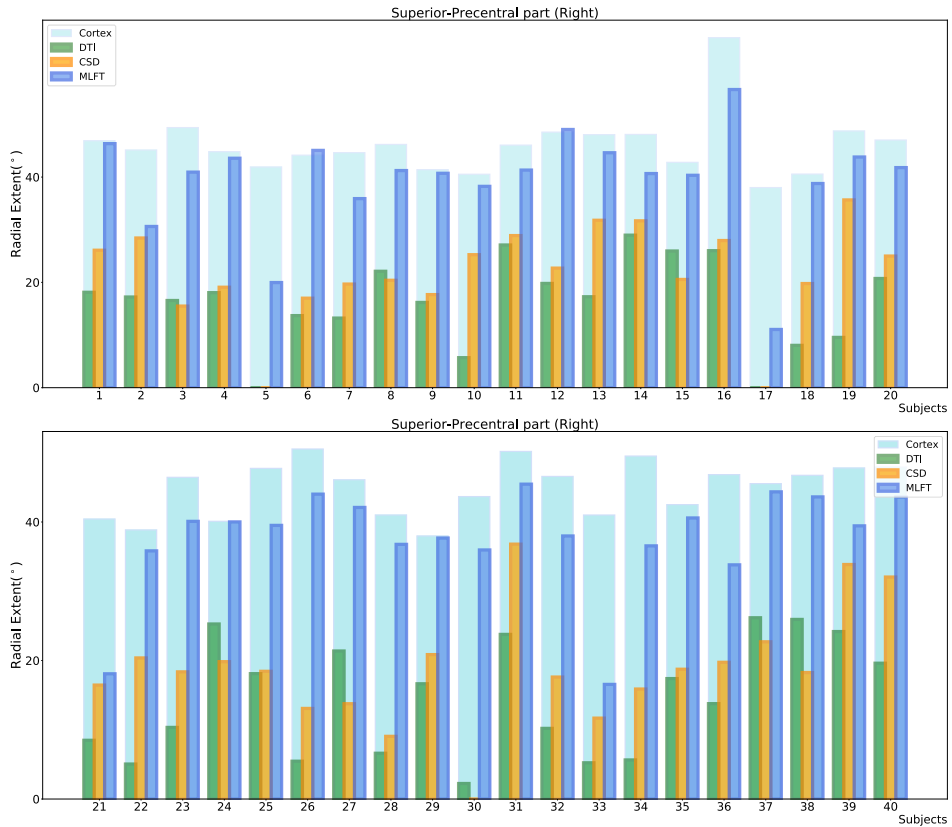
Figure 3.13: Comparison of the radial extent of the corticospinal tract (CST) sub-bundle reaching the lateral part of the precentral cortex in the right hemisphere. This figure illustrates the radial extent for the reconstructions using diffusion tensor imaging (DTI)-based tractography (green), constrained spherical deconvolution (CSD)-based tractography (orange), and multi-level fiber tracking (MLFT; dark blue). The maximum extent that is the extent of the target cortex part is depicted in light blue.
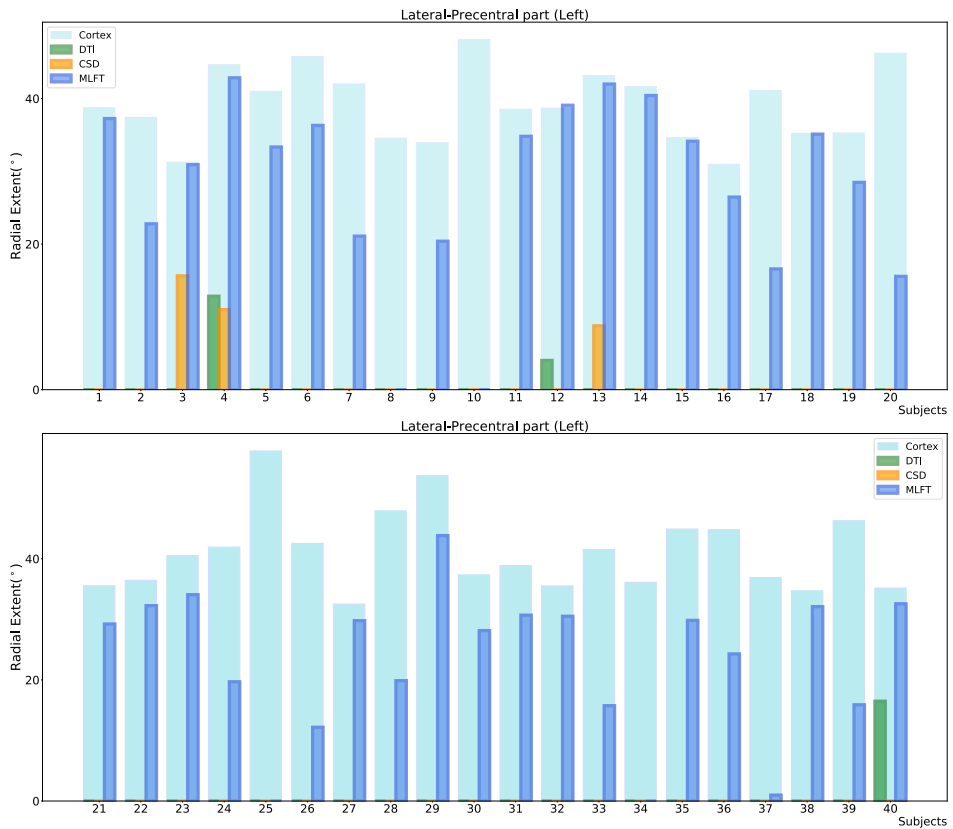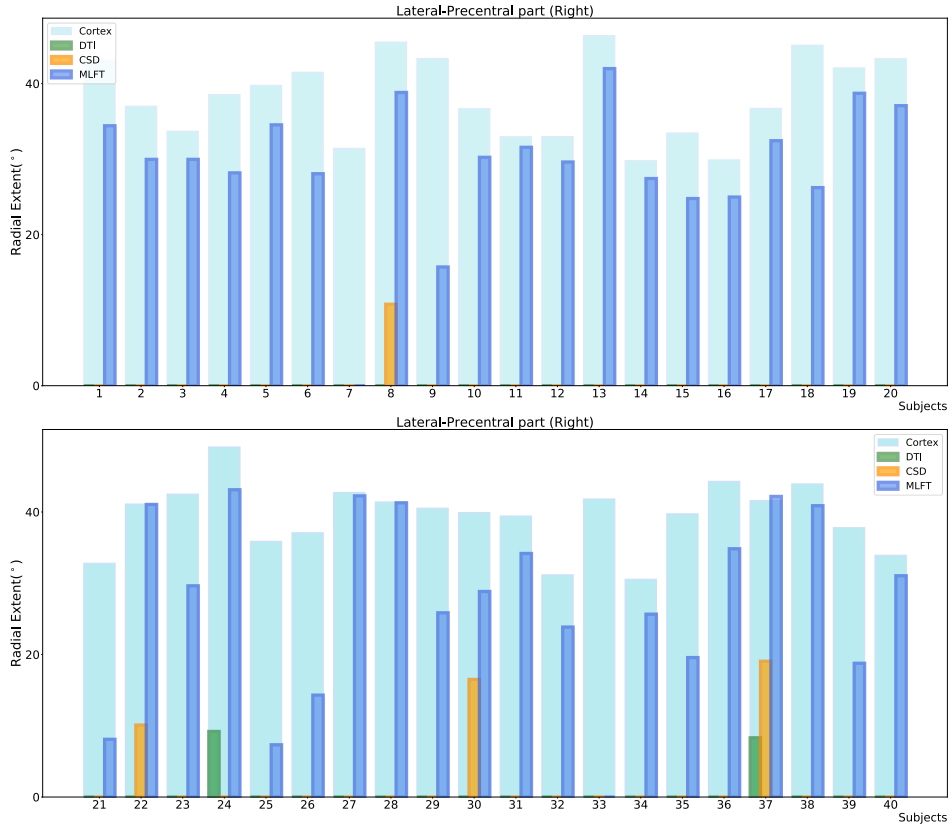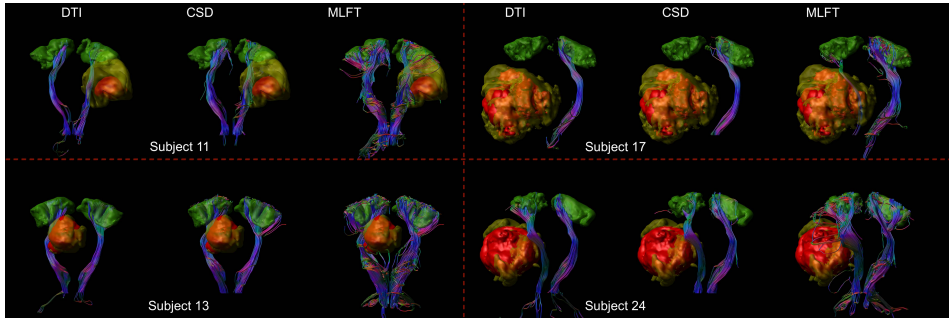
Figure 3.14: Reconstructions of the corticospinal tract (CST) sub-bundles given the superior part of the precentral gyrus (green) as the target region of interest. In most cases, deterministic diffusion tensor imaging (DTI)- and constrained spherical deconvolution (CSD)-based reconstructions reach the target region. However, in presence of extensive tumor (red) and edema (yellow), only MLFT was capable of providing a proper fiber reconstruction.
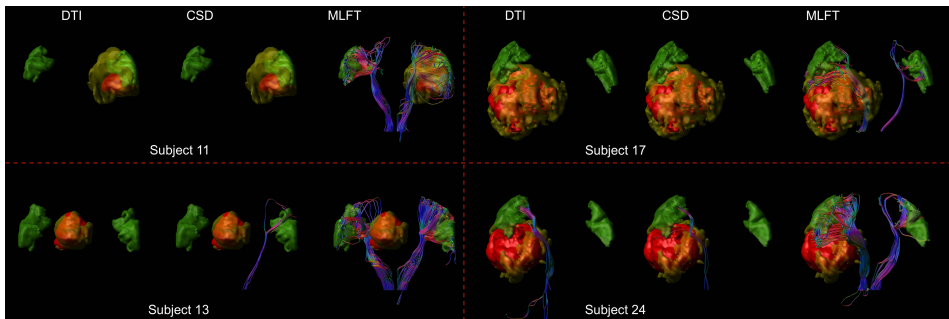
Figure 3.15: Reconstructions of the corticospinal tract (CST) sub-bundles given the lateral part of the precentral gyrus (green) as the target region of interest. The limitation of diffusion tensor imaging (DTI)- and constrained spherical deconvolution (CSD)-based algorithms is highlighted as most often these approaches are unable to reconstruct any pathways given such target regions, regardless of tumor size (red: tumor core, yellow: edema).

Multi-level fiber tractography combined with functional motor cortex mapping

Abstract

Tractography of the corticospinal tract is paramount to presurgical planning and guidance of intraoperative resection in patients with motor-eloquent gliomas. It is well-known that DTI-based tractography as the most frequently used technique has relevant shortcomings, particularly for resolving complex fiber architecture. The purpose of this study was to evaluate multilevel fiber tractography combined with functional motor cortex mapping in comparison with conventional deterministic tractography algorithms.

Thirty-one patients (mean age, 61.5 [SD, 12.2] years) with motor-eloquent high-grade gliomas underwent MR imaging with DWI (TR/TE = $5000/78ms$, voxel size= $2 \times 2 \times 2mm^3$, 1 volume at $b = 0s/mm^2$, 32 volumes at $b = 1000s/mm^2$). DTI, constrained spherical deconvolution, and multilevel fiber tractography–based reconstruction of the corticospinal tract within the tumor-affected hemispheres were performed. The functional motor cortex was enclosed by navigated transcranial magnetic stimulation motor mapping before tumor resection and used for seeding. A range of angular deviation and fractional anisotropy thresholds (for DTI) was tested.

For all investigated thresholds, multilevel fiber tractography achieved the highest mean coverage of the motor maps (eg, angular threshold = 60°; multilevel/constrained spherical deconvolution/DTI, 25% anisotropy threshold = 71.8%, 22.6%, and 11.7%) and the most extensive corticospinal tract reconstructions (e.g., angular threshold = 60°; multilevel/constrained spherical deconvolution/DTI, 25% anisotropy threshold = $26,485mm^3$, $6308mm^3$, and $4270mm^3$).

Multilevel fiber tractography may improve the coverage of the motor cortex by corticospinal tract fibers compared with conventional deterministic algorithms. Thus, it could provide a more detailed and complete visualization of corticospinal tract architecture, particularly by visualizing fiber trajectories with acute angles that might be of high relevance in patients with gliomas and distorted anatomy.

4.1   Introduction

Gliomas are the most prevalent malignant brain tumors in adults, and particularly anaplastic astrocytoma and glioblastoma as representatives of high-grade gliomas have poor prognoses [62,63,122]. Contemporary treatment combines neurosurgical tumor resection with extended focal radiation therapy and adjuvant chemotherapy [67–69]. Specifically, a maximum extent of resection correlates to prolonged survival and improved quality of life [1, 72, 74]. However, a maximum extent of resection needs to be weighed against the risk of surgery-related functional decline such as persistent paresis or aphasia, which may arise from tumor resection in or near functionally eloquent structures such as the motor or language cortex [76,77]. Additionally, subcortical WM pathways such as efferent fibers that interconnect certain brain areas or course down to the periphery may need to be respected to avoid lasting functional deficits [123, 124].

Imaging and mapping of brain function are essential for a maximum safe resection combined with a high extent of resection and a low-risk profile for permanent functional deterioration [69,80,81,125]. In the preoperative setup, DWI with tractography is used for delineation of WM architecture, which can then be visualized and respected during tumor resection [126,127]. Particularly, DTI-based tractography is commonly applied to reconstruct certain fiber tracts, relating to its comparatively wide availability and low false-positive rate [6]. However, despite its frequent application in the preoperative work-up of patients with glioma, the technique has relevant shortcomings that render the accuracy of the method questionable [91,128]. Specifically, major issues relate to potential underrepresentation of fiber branching or crossing fibers, which are difficult to resolve by DTI-based tractography [5, 94, 95]. Alternatives to DTI-based tractography exist, including methods such as constrained spherical deconvolution (CSD)-based tractography, which has shown improved specificity compared with DTI-based tractography, given that CSD-based tractography is determined by higher angular resolution and the possibility of also disentangling more complex fiber configurations [21,25]. In CSD, multiple fibers passing through a voxel with distinct orientations can be estimated, depending on the fiber orientation distribution (FOD) [21,25].

Multilevel fiber tractography (MLFT), presented in Chapter 2, has been developed from CSD-based tractography and similarly propagates fiber pathways on the basis of FOD peaks, with the main advancement that MLFT proposes that FOD peaks do not solely reflect crossing fibers but may also reflect high angular deviation of fibers or their branching. Chapter 3 has demonstrated that MLFT improved reconstruction of the corticospinal tract (CST) in patients with motor-eloquent high-grade gliomas by generating fiber bundles with higher radial extent (ie, delineation of CST fanning with a wider range) compared with DTI as well as CSD-based deterministic CST tractography, thus potentially showing a more complete picture of the actual CST architecture. Yet, without optimal seeding of the ROI for tractography, MLFT would be at considerable risk of reconstructing

false-positive WM pathways, given that it can also include acute angles of fiber courses, which might be particularly frequently observed among patients with brain tumors due to the space-occupying effect that may lead to fiber diversion and compression as was shown in Chapter 3.

The issue of optimal ROI seeding for CST reconstruction may be addressed by combining MLFT with preoperative functional mapping, such as navigated transcranial magnetic stimulation (nTMS). In essence, nTMS can target neurostimulation to the brain with subcentimeter precision and enables the spatial identification and demarcation of the motor cortex in relation to a lesion [129, 130]. Particularly, nTMS-based motor mapping has been frequently used in the preoperative setup and for guidance of intraoperative resection in patients with motor-eloquent brain tumors [130–132]. The approach has been shown to result in cortical motor maps similar to those generated by intraoperative direct electrical stimulation as the reference standard for functional cortical mapping [133–135]. More recently, combinations of tractography with nTMS have been used to establish function-based tractography of the CST, which is based on the definition of the nTMS-derived cortical motor map as an ROI [4, 112, 113, 136, 137].

Against this background, the purpose of the present study was to combine MLFT for reconstruction of the CST with nTMS for enclosing the functional motor cortex in patients with motor-eloquent gliomas. We hypothesized that MLFT may show higher coverage of the nTMS motor map (ie, the highest percentage of fibers of the CST being connected to the motor cortex) compared with deterministic DTI-based and CSD-based tractography.

4.2   Materials and Methods

4.2.1   Study Design and Patient Cohort

This study was approved by the local institutional review board (Ethikkommission Technische Universität München) and was conducted in accordance with the Declaration of Helsinki. The requirement for written informed consent for this study was waived due to the retrospective design.

Eligible patients were identified by chart review, covering the time interval from February 2019 to February 2020. Inclusion criteria were the following: 1) older than 18 years of age, 2) availability of preoperative 3T MR imaging, including diffusion-weighted sequences, 3) diagnosis of a high-grade glioma (based on imaging findings and later confirmation by histopathologic evaluation of biopsy probes or tumor tissue harvested during surgical resection), 4) suspected motor-eloquent tumor location according to preoperative MR imaging, and 5) availability of preoperative nTMS-based motor mapping of the tumor-affected hemisphere.

Overall, 31 patients (mean age, 61.5 [SD, 12.2] years; age range, 34.4–85.1 years; 12 women) matched the inclusion criteria and were considered for this study.

Three patients were diagnosed with World Health Organization grade III gliomas, and 28 patients with World Health Organization grade IV gliomas, and the right hemisphere was affected by the tumor volume in 19 patients.

4.2.2   Data Acquisition

MR Imaging

Preoperative MR imaging was performed on two 3T scanners (Achieva dStream or Ingenia; Philips Healthcare) using a 32-channel head coil. The imaging protocol included a 3D FLAIR sequence (TR/TE $= 4800/277ms$, $1mm^3$ isotropic voxels covering the whole head), an axial T2-weighted sequence (TR/TE $= 3396/87$ ms, voxel size $= 0.36 \times 0.36 \times 4mm^3$), a diffusion-weighted sequence (TR/TE $= 5000/78$ ms, voxel size $= 2 \times 2 \times 2mm^3$, 1 volume at $b = 0s/mm^2$, 32 volumes at $b = 1000s/mm^2$), and a 3D T1-weighted turbo field echo sequence (TR/TE $= 9/4ms$, $1mm^3$ isotropic voxels covering the whole head) without and with intravenous injection of a contrast agent using a dose of $0.2mL$ per kg body weight of gadoteric acid (Dotagraf, $0.5mmol/mL$; Jenapharm).

nTMS

Preoperative motor mapping of the tumor-affected hemisphere was performed using nTMS (NBS system 4.3 or 5.0; Nexstim). For neuronavigation, the preoperatively acquired contrast-enhanced 3D T1-weighted turbo field echo sequence was used. Motor mapping was performed according to a standardized protocol using a figure-of-eight stimulation coil and a biphasic pulse wave application [130, 138]. Both representations of upper and lower extremity muscles were mapped within the tumor-affected hemisphere using an intensity of 105%–110% of the individual resting motor threshold for the upper extremity and an intensity of at least 130% of the resting motor threshold for the lower extremity muscles [130, 138]. Motor-positive nTMS points were identified during post hoc analysis, which were required to show an amplitude of motor-evoked potentials of $\geq 50\mu V$, with motor-evoked potential onset latencies within the typical ranges [130, 139, 140].

Image Segmentation and Processing of DWI Data.

Before image segmentation, all MR imaging data were transferred to Montreal Neurological Institute space (with an isotropic voxel size of $1mm^3$). Given that commonly used parcellation pipelines may not produce robust segmentations in the presence of brain tumors, lesion filling was performed using the Virtual Brain Grafting toolkit [46, 100]. This approach replaces the tumor volume with synthetic healthy tissue [100].

As a prerequisite for lesion filling, lesion segmentation was performed using the BraTS toolkit [101, 102]. The BraTS toolkit was provided with T1-weighted images, both noncontrast and contrast-enhanced, as well as FLAIR and T2-weighted images, to perform the lesion segmentation [101, 102]. The segmentation differentiates between the tumor core (necrotic center and contrast-enhancing tumor parts) and FLAIR-hyperintense zones (edema/tumor infiltration).

All diffusion-weighted data sets were preprocessed by performing motion and eddy current corrections [141]. To estimate FODs, we used recursive calibration of the response function [103]. Given the number of acquired diffusion-weighted volumes, the order of spherical harmonics describing FODs was set to $L_{max} = 6$. All processing was performed in ExploreDTI (Version 4.8.6).

Because nTMS was performed as a separate acquisition, nTMS points had to be transferred to the space of the T1-weighted and diffusion imaging data sets, achieved by performing registration of the contrast-enhanced T1-weighted images to the masks containing all motor-positive nTMS points of the tumor-affected hemisphere. All nTMS points were enlarged using a hull of 2-mm radius by default to provide the final motor cortex seed mask [4, 112]. All image coregistrations and segmentations were visually inspected for quality and manually corrected, when necessary, by a trained neuroradiologist.

Tractography Algorithms

Three tractography algorithms were used for CST reconstruction: DTI-based tractography, CSD-based tractography, and MLFT. MLFT was introduced in Chapter 2 and is a bundle-specific algorithm that reconstructs fiber bundles as multilevel structures. The algorithm requires seed and target regions (i.e., the ipsilateral anterior pontine brainstem level and the nTMS-derived cortical motor map) and a maximum number of levels. At each iteration, streamline propagation is performed using a deterministic CSD-based algorithm. At the end of each iteration, FOD peaks of the points along pathways that did not reach the target region are used as initial directions at the following iteration. Thus, the potential of the peaks to represent branches is explored.

The angular deviation threshold (ADT) is aimed at maintaining smoothness and physical plausibility of the fiber pathways because it prevents propagation into directions highly deviating from the previous step direction. However, the threshold may impact the accuracy of the reconstruction, depending on the voxel and angular resolution of the data. Thus, each tractography algorithm was run with 3 different ADTs, namely 20°, 45°, and 60°. For DTI-based tractography, 3 levels of the fractional anisotropy threshold (FAT) were used by setting the individual fractional anisotropy to a maximum value that enables reconstructing a minimum fiber course (ie, 100% FAT). For CSD-based tractography as well as MLFT, the FOD peak threshold was set to 0.08 similarly to the study in Chapter 3. The tractography step size was set to half the voxel size, and the number of

iterations for MLFT was set to 2.

Statistical Analysis

Statistical testing was performed using SPSS (Version 26.0; SPSS Statistics for Windows; IBM) and the SciPy library (Version 1.3.1). The threshold for statistical significance was set at $\alpha = 0.05$.

To assess and compare reconstructions of the CST, we computed the ratio of the visited voxels of the nTMS mask to the reconstructed fibers for each parameter configuration (ADT = 20°, 45°, and 60°; FAT = 25%, 50%, and 75%) and algorithm (DTI-based tractography, CSD-based tractography, and MLFT). This computation provides an estimate of how much of the nTMS mask (ie, cortical motor-positive nTMS points) is covered and, consequently, how complete the reconstruction is according to the function-based reference (nTMS mask). Additionally, volumes of the reconstructed bundles were computed as the accumulated volume of all the voxels visited by at least 1 fiber pathway. Only the bundle part between the seed and target region was taken into account. To compare the nTMS coverage as well as the volumes of the reconstructions as obtained by the different algorithms depending on the FAT as well as ADT, we performed paired 1-sided Wilcoxon tests. Furthermore, the nTMS coverage achieved by the same algorithm at different ADT settings was compared using paired 2-sided Wilcoxon tests.

4.3 Results

Tractography using MLFT was capable of reconstructing fiber bundles with higher volumes (on average 10,367, 19,567, and $26,485 mm^3$ for ADTs of 20°, 45°, and 60°) than what was achieved by the DTI- and CSD-based algorithms, true for all used ADTs and FATs (Figure 4.1 and Table 4.1). DTI-based tractography reconstructed statistically significant smaller bundles than CSD-based tractography at 25% ($p = 0.54$, 0.99, and 1 for 20°, 45°, and 60° ADT), 50% ($p = 0.97$, 1, and 1 for 20°, 45°, and 60° ADT) and 75% FAT ($p = 1$ for all ADTs) based on 1-sided Wilcoxon tests.

Compared with the other approaches, MLFT reconstructions of the CST achieved the highest coverage of the nTMS motor map, which amounted to 38.7%, 60.8%, and 71.8%, on average, for ADTs of 20°, 45°, and 60°, respectively (Figure 4.2 and Table 4.2). MLFT also achieved higher coverage in case of tumor-induced bundle deformations (Figure 4.1). CSD-based tractography achieved higher coverage of the nTMS motor map than DTI-based tractography, regardless of the settings for ADT and FAT (Figure 4.2). This finding was also confirmed by comparing reconstructions obtained with the same ADTs with 1-sided Wilcoxon tests ($p > 0.95$ for all comparisons, Table 4.2).
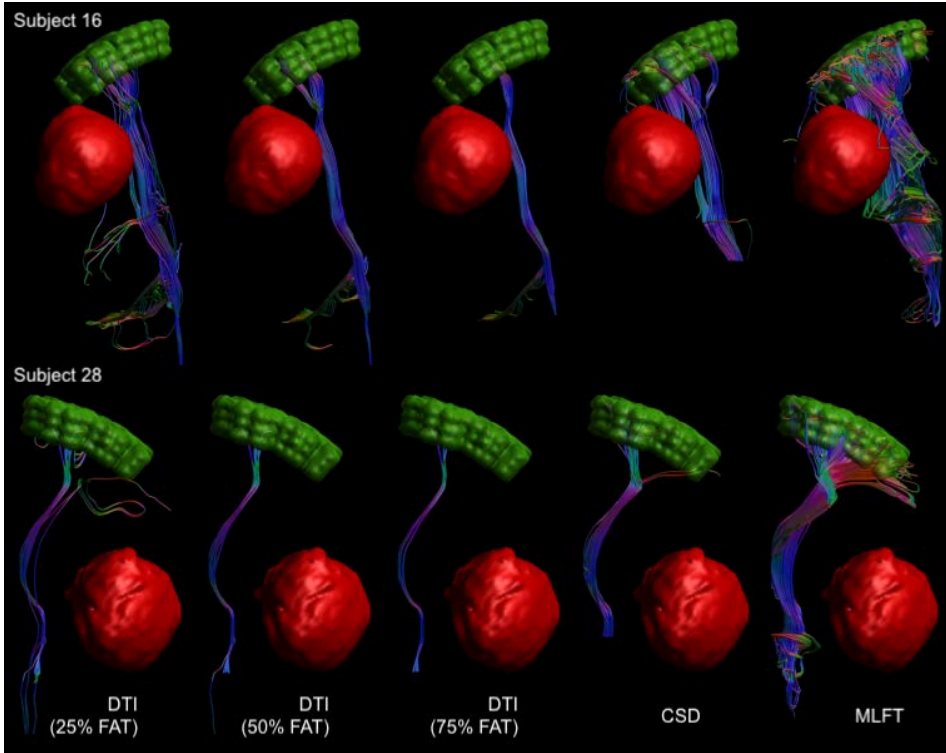
Figure 4.1: The nTMS-based motor map (green indicates single motor-positive nTMS points with a 2-mm hull) was used as the target region for reconstruction of the CST within the tumor-affected hemisphere (red indicates the tumor core). MLFT shows higher nTMS mask coverage compared with DTI- and CSD-based results, including cases of tumor-induced bundle deformation (subject No. 28).

The change of the ADT led to statistically significant changes in nTMS motor map coverage ($p < .01$) based on 2-sided Wilcoxon tests, which can also be observed in an exemplary patient case (Figure 4.3). Only when using 75% FAT for DTI-based reconstruction was a statistically nonsignificant difference observed between reconstructions obtained with 20° and 60° ADT as well as 45° and 60° ADT.

4.4   Discussion

We combined MLFT with motor mapping for CST reconstruction based on nTMS motor maps used for ROI placement in patients with motor-eloquent gliomas. Tractography results were compared against deterministic DTI-based and CSD-
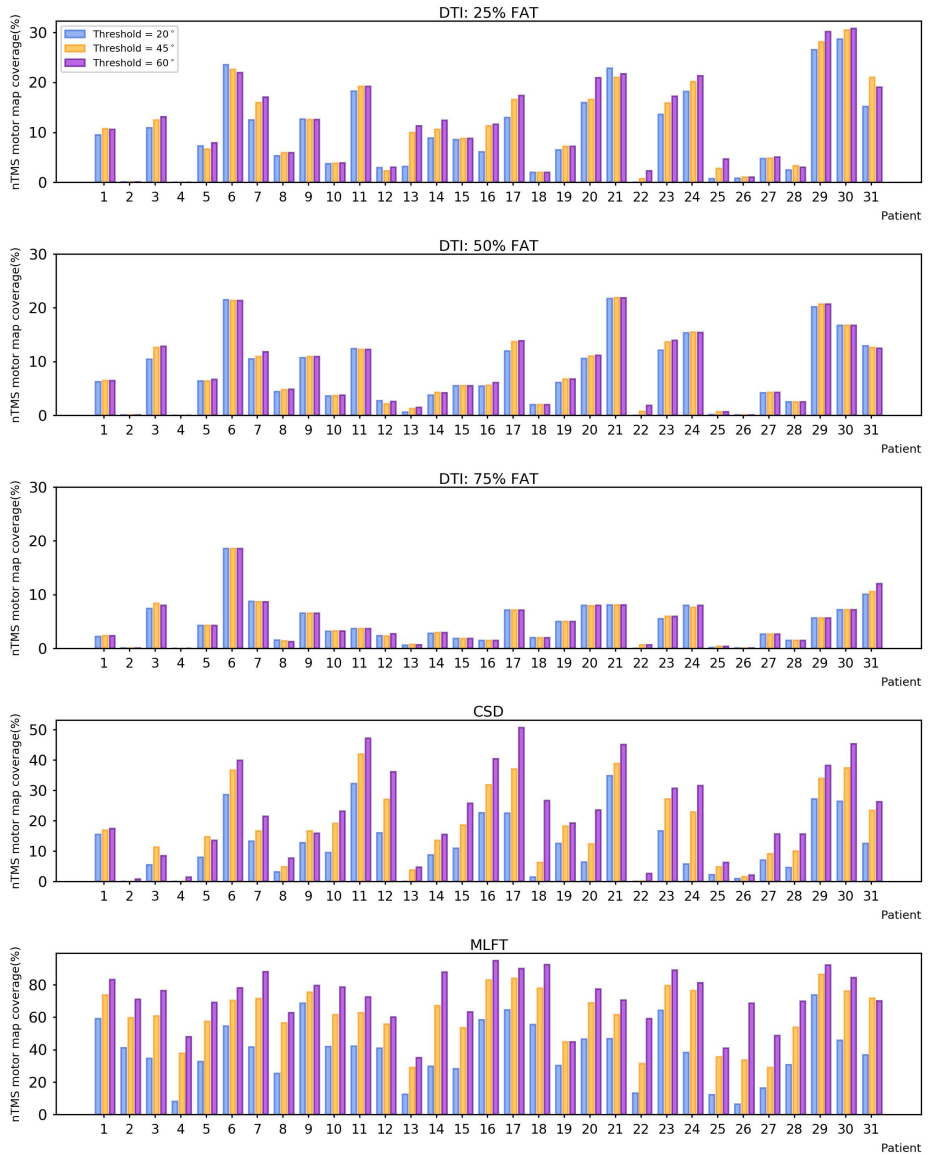
Figure 4.2: nTMS motor map coverage derived from CST reconstructed with DTI-based (with 25%, 50%, and 75% of the individual FAT), CSD-based, and MLFT tractography. Changes of ADTs appear to only have visible effect on the result of CSD-based tractography and MLFT.
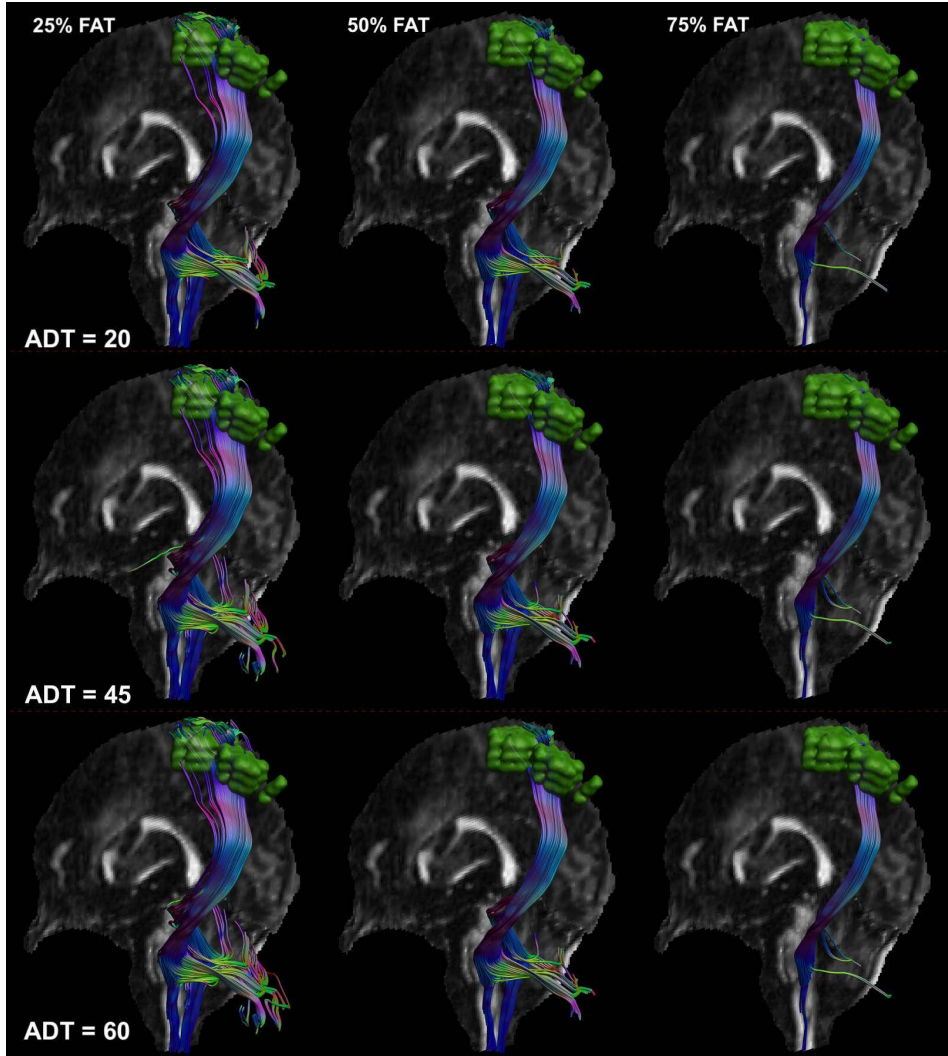
Figure 4.3: DTI-based reconstructions of the CST with the nTMS-based motor map (green indicates single motor-positive nTMS points with a 2-mm hull) with varied ADT (rows) and FAT levels in subject No. 30.

based tractography, given that these techniques are commonly used for clinical tractography in patients with brain tumors. The main findings are as follows: 1) MLFT enabled CST reconstruction with higher bundle volumes, and 2) MLFT yielded higher coverage of the nTMS motor map (ie, a higher percentage of the nTMS points reached by the reconstructed CST).

The MLFT algorithm we used was developed from CSD-based tractography, and it similarly reconstructs fiber pathways on the basis of FOD peaks as was shown in Chapter 2. However, in contrast to CSD-based tractography, MLFT suggests that FOD peaks may also be reflective of high angular deviation of fibers or their branching and may not only stem from fiber crossings. Hence, reconstruction of the CST with MLFT may produce bundles with higher radial extent; thus, the delineation of CST fanning with a wider range by also reconstructing fiber courses with acute angles becomes possible. We have shown this feature in Chapter 3 study among patients with motor-eloquent high-grade gliomas, but the motor cortex mask was defined using a parcellation mask of the precentral, postcentral, and paracentral gyri combined with a cross-section of the brainstem at the pontine level.

Given that MLFT may naturally reconstruct bundles with higher fiber count due to inclusion of fibers that course with acute angles, the potential risk of increasing the false-positive rate (i.e., proportion of fibers that are visualized but do not connect to the actual functional motor cortex) is present. Specifically, to avoid a high false-positive rate, MLFT would require well-defined ROI seeding, and if certain pathways do not connect to the ROI, the algorithm checks to see if any deviation at the previous reconstruction points would allow connection to the ROI, thus providing some control over specificity while potentially improving sensitivity. In this regard, motor maps from preoperative nTMS were used as the target ROIs, given that nTMS motor mapping has shown high agreement with intraoperative direct electrical stimulation as the reference standard for functional mapping in patients with brain tumor [133–135]. Furthermore, nTMS has also been effectively combined with DTI-based tractography in the past, allowing DTI-based reconstruction of the CST using functional data for ROI seeding, which could improve tracking of fibers for preparation and guidance of tumor resection and stratification for perioperative functional deficits [4, 112–114, 136]. In this context, compared with conventional seeding without functional data (e.g., manual delineation of the brainstem for ROI generation), nTMS-based tractography of the CST has been shown to result in a lower number of aberrant tracts (ie, tracts not belonging to the CST), and it changed the surgical strategy in more than twice as many patients [113, 114]. Furthermore, detailed somatotopic CST reconstructions might become possible when using nTMS motor maps as ROIs, with greater spatial overlap between the motor cortex and the cortical end region of the CST compared with conventional anatomic seeding for tractography [137].

Reconstructions of the CST using MLFT showed the highest bundle volume for the CST, combined with the highest coverage of the nTMS motor map compared with deterministic DTI- or CSD-based tractography. This result may indicate that a more complete reconstruction of the CST can be achieved with MLFT, which is most likely due to reconstruction of fibers with higher radial extents. Glioma may cause considerable deviation of CST fibers, which may, in part, be lost to reconstruction when using DTI- or CSD-based approaches (Fig 4.1). The higher

coverage of nTMS maps when applying MLFT could increase confidence because the fibers reconstructed from MLFT are actually representative of the motor system (Figure 4.2), given that higher nTMS coverage is suggestive of more fibers being connected to the actual functional motor cortex. Of note, preoperatively enclosing the functional motor cortex with nTMS allows definition of its individual extent and location, which can be drastically aberrant to the structural landmark anatomy due to shifts related to the space-occupying effects and, most notably, due to plastic reshaping of functional motor representations in response to the presence and growth of glioma [142–144].

A more complete reconstruction of fibers belonging to the CST is of clinical merit when achieving an optimal onco-functional balance because their visualization could help avoid surgery-induced damage and, thus, occurrence of lasting perioperative paresis. Specifically, CST reconstruction with broader fanning by MLFT could also generate laterally coursing and marginal fibers, which could be at particular risk of damage when approaching a maximized extent of resection. The higher CST bundle volumes may likely also result in pathways with a smaller lesion-to-tract distance, having potential impact on resection planning. Previous work using nTMS motor mapping combined with DTI-based tractography of the CST has proposed the lesion-to-tract distance as a parameter for presurgical stratification of the risk of permanent motor function decline, with lower lesion-to-tract distances being associated with a higher risk for lasting deficits [4, 112, 136]. Application of MLFT instead of DTI-based tracking might potentially allow refined results for lesion-to-tract distances, with a potential definition of more realistic lesion-to-tract distances that may facilitate improved surgical outcome in terms of the extent of resection and the patient's functional status.

A major limitation of this study is that tractography results were not confirmed by intraoperative direct electrical stimulation as the reference standard for functional mapping. Due to the retrospective character of this study, this confirmation was not possible but may be achieved in future studies. Hence, potential overrepresentations of fibers when using the MLFT algorithm cannot be fully excluded. Another limitation of MLFT relates to FOD accuracy, given that a high number of diffusion directions and high b-values are not routinely acquired for clinically used diffusion-weighted MR imaging sequences. As a consequence, the accuracy of the fitted diffusion models could be restricted because FODs have to be represented by lower-order spherical harmonics. Furthermore, the FOD algorithm used does not estimate separate response functions for different tissues [103]. However, using acquisitions with multiple diffusion-weightings (eg, multishell imaging) over the sequence we used would facilitate applying FOD algorithms that can differentiate multiple tissues [120].

4.5 Conclusion

Compared with routinely used deterministic DTI-based and CSD-based tractography of the CST, MLFT may enable CST reconstructions with a higher bundle volume paired with higher coverage of the functional motor cortex. Thus, MLFT could provide a more detailed visualization of CST architecture by also visualizing fiber courses with acute angles, which might be of particular relevance in patients with gliomas and distorted anatomy of the motor system. However, prospective confirmation of tractography results from MLFT by intraoperative direct electrical stimulation as the reference standard for functional mapping is required for validation purposes.

Supplementary material

		ADT = 20°			ADT = 45°			ADT = 60°		
		Mean Volume±SD (range), mm^3	p-value CSD	MLFT	Mean Volume±SD (range), mm^3	p-value CSD	MLFT	Mean Volume±SD (range), mm^3	p-value CSD	MLFT
DTI	25% FAT	3226 ± 2401 (0 − 7851)	0.54	1	3940 ± 2790 (0 − 9624)	0.99	1	4269 ± 3045 (0 − 11020)	1	1
	50% FAT	2739 ± 2031 (0 − 6359)	0.98	1	3038 ± 2118 (0 − 6633)	1	1	3199 ± 2230 (0 − 8062)	1	1
	75% FAT	1518 ± 1095 (0 − 4187)	1	1	1585 ± 1026 (0 − 4164)	1	1	1618 ± 1055 (0 − 4384)	1	1
CSD		3284 ± 2618 (0 − 9724)	-	1	5149 ± 3305 (0 − 12038)	-	1	6308 ± 3761 (187 − 13812)	-	1
MLFT		10367 ± 4912 (1440 − 20712)	0	-	19567 ± 8039 (4209 − 37172)	0	-	26485 ± 10719 (8688 − 54909)	0	-

Table 4.1: Volumes of the bundles reaching the nTMS motor map (mean and standard deviation (SD)). Only the bundle parts between the seed and target regions were taken into account. For DTI-based tractography, three ADTs as well as three FATs were included. *P*-values are presented for the comparison of volumes between methods (one-sided Wilcoxon test where the alternative hypothesis states that the approach from the column (CSD or MLFT) achieves greater coverage). MLFT-reconstructed bundles are shown to have higher volumes than the bundles reconstructed by DTI- and CSD-based tractography with the same ADT.

		ADT = 20°			ADT = 45°			ADT = 60°		
		Mean Coverage±SD (range), %	p-value CSD	MLFT	Mean Coverage±SD (range), %	p-value CSD	MLFT	Mean Coverage±SD (range), %	p-value CSD	MLFT
DTI	25% FAT	9.8 ± 8.1 (0 − 28.7)	0.961	1	11.1 ± 8.4 (0 − 30.4)	0.99	1	11.7 ± 8.6 (0 − 30.8)	1	1
	50% FAT	7.8 ± 6.8 (0 − 21.7)	0.9994	1	8.1 ± 6.7 (0 − 21.8)	1	1	8.2 ± 6.6 (0 − 21.8)	1	1
	75% FAT	4.4 ± 4 (0 − 18.5)	1	1	4.5 ± 4 (0 − 18.5)	1	1	4.6 ± 4.1 (0 − 18.5)	1	1
CSD		11.9 ± 10.2 (0 − 34.8)	-	1	18 ± 12.8 (0 − 42)	-	1	22.6 ± 15 (1 − 50.6)	-	1
MLFT		38.7 ± 18.3 (6.4 − 73.7)	0	-	60.8 ± 17.1 (28.9 − 86.2)	0	-	71.8 ± 16 (35 − 94.7)	0	-

Table 4.2: nTMS motor map coverage (mean and standard deviation (SD)) by the three algorithms for different ADTs and FATs in case of DTI-based tractography. *P*-values are presented for the comparison of coverage between methods (one-sided Wilcoxon test where the alternative hypothesis states that the approach from the column (CSD or MLFT) achieves greater coverage). MLFT consistently achieves higher nTMS coverage compared to the DTI- and CSD-based tractography.

A comparison of spherical deconvolution models for fiber tractography in gray matter

Abstract

Diffusion MRI is a powerful tool allowing for in-vivo analysis of brain microstructure. To date, the development and application of dMRI has been mostly focused on the brain white matter. More specifically, for a long time spherical-deconvolution (SD) models have only been applied to the white matter. The brain gray matter received less attention, which is partly because of the difficulty to visualise its structure with conventionally achievable imaging resolutions. For this reason, it remains largely unknown to which extent methods developed for the brain white matter are applicable to the grey matter.

To bridge this knowledge gap we evaluated three SD models to obtain fiber orientation distribution (FOD): constrained spherical deconvolution (CSD) based FODS, multi-shell CSD-based FODs and multiple FODs with Generalized Richardson Lucy deconvolution (mFOD), using the diffusion MRI data of the motor cortex of a healthy volunteer (420 gradient directions at $b = 1000s/mm^2$ and 840 directions at $b = 2000s/mm^2$, $760\mu m$ isotropic resolution). We investigated local diffusion orientation patterns using radiality index in relation to the white-gray matter interface as well as connectivity patterns in the gray matter based on deterministic streamline-based tractography.

All the evaluated diffusion models showed capability to reflect the expected diffusion orientation patterns in cortical foldings. White-gray matter interface was generally characterized by lower radiality in the banks ($\sim$0.25, mean over all SD models) and higher in the crowns ($\sim$0.59, mean over all SD models) in the crowns. Both in crowns and banks all models showed highest radiality in deeper part of GM (ranging between 0.75 and 0.93) which is followed by a drop in radialty in the pial surface. Fiber tractography using each of the models revealed well-organized tangentially oriented pathways and highlighted the difference in intracortical connectivity between the primary and somatosensory motor areas. The shortest group of fiber pathways were characterized by the highest deviation when connecting white and gray matter surfaces, reaching maximum mean deviation of $71°, 72°, 70°$ in M1 and $61°, 68°, 63°$ in S1 for CSD-, MS CSD- and mFOD-based reconstructions, all respectively, while groups of longer pathways did not exceed mean deviation of $30°$ per connectivity group.

5.1 Introduction

Over the years diffusion MRI (dMRI) has provided valuable insight into the macro- and micro-structure of the human brain. However, the advances in tractography [3] and connectomics [9] using dMRI have been primarily focused on the brain white matter (WM). The brain gray matter (GM) largely remains terra incognita. The interest of tractography and connectivity in relation to GM so far mainly centered on solving the issue of gyral bias [145, 146] and cortical parcellation [147, 148].

However, disentangling the neuronal structure of GM might have a wider number of applications. As all the nerve fibers are originating into WM from the cortex, it is of high interest to understand the wiring inside the cortex itself for precise and robust functional mapping. Neuroanatomical knowledge of GM may also be useful in pathological cases, for instance, for GM atrophy analysis in multiple-sclerosis patients [149].

In the past decade several papers provided insights into GM micro-structure and intra-connectivity both in vivo and ex vivo. McNab et al. [150] presented depth-dependent analysis of micro-structural properties and showed that the diffusion tensor model can reflect the difference in fiber orientation in subparts of the motor and visual cortex detailing the observations of Anwander et al. [151]. They highlighted sharp differences in dominant diffusion orientation between primary and somatosensory cortex, with the former characterized by mainly radial diffusion orientation in relation to the cortical surface and the latter by mainly tangential diffusion orientation.

Even more detailed layer-related information was presented by Aggarwal et al. [152] who performed high-resolution ex-vivo diffusion MRI acquisition with $92 \mu m$ isotropic voxel resolution. The work provided insight into the ratio of tangential and radial diffusion orientations in a number of brain areas, including primary and somatosensory motor cortex, with the help of constrained spherical deconvolution (CSD) based fiber orientation distributions (FODs) [21].

Tractography-based analysis of the inter-connectivity was performed by Leuze et al. [153] presenting qualitative analysis on the ex-vivo specimen of the visual cortex dividing it into four layers. Using CSD for FOD estimation, the authors could differentiate each of the layers based on the diffusion orientation in relation to the surface.

These studies were either performed using very high-resolution ex-vivo data or with the use of only a diffusion tensor model because of the technical limitations of high-resolution in-vivo acquisition. However, with the recent advances in diffusion MRI acquisition it is now possible to acquire in-vivo brain scans with sub-millimeter resolution [154]. This provides an opportunity to make use of state-of-the-art diffusion models. However, most of the existing models were created and used with WM in mind. Thus, an investigation into whether they can adequately reflect known anatomical microstructural features of GM is called for.

The models we chose to focus on are all based on spherical deconvolution (SD). CSD was chosen as one of the commonly used approaches to FOD estimation. However, although it performs well in WM, using the same response function for GM may lead to less specific results, meaning that the dominant diffusion orientations may appear less pronounced. For that reason, we also use a multi-shell CSD (MS CSD) [43] approach for our analysis which considers the contribution of WM, GM and the corticospinal fluid to the final diffusion signal. A downside of the MS CSD approach is that it uses a single response function throughout the brain, which may not properly reflect anisotropic characteristics of GM. Therefore, a multiple FOD (mFOD) [120] approach based on Generalized Richardson-Lucy deconvolution was also included, as it estimates separate response functions for each compartment. The mFOD algorithm was developed with multiple-tissue analysis in mind trying to provide adequate FODs per tissue type. This way the performance is not limited by a single response function that might mainly reflect WM properties.

In this work we investigated the applicability of existing models focusing on the primary and somatosensory motor regions. The difference in myelination structure between these cortical areas is well established, with more prominent tangentially-oriented nerve layers in the somatosensory cortex [155]. We extended the analysis strategy of McNab et al [150] by comparing peaks of the SD-based local fiber orientation distributions to the local orientation of the intermediates cortical surfaces as well as by analyzing tractography reconstructions in order to investigate whether state-of-the-art SD models can reflect laminar structure of the cortex from in-vivo data.

5.2   Methods

5.2.1   Data

We used dMRI data obtained from a single healthy male volunteer, born in 1989, with an imaging resolution of $760\mu m$ isotropic, which is freely distributed by Wang et al. [154]. Data included 420 gradient directions at $b = 1000s/mm^2$ and 840 directions at $b = 2000s/mm^2$. High-resolution FreeSurfer cortex parcellation [46] was obtained after registration of the T1 image ($0.7mm$ isotropic) to dMRI space. The brain was cropped around the left primary motor (M1) and sensory motor (S1). Fiber orientation distributions (FOD) were estimated using CSD, multi-shell (MS) CSD and the mFOD framework using ExploreDTI [39] and MRIToolKit (https://github.com/delucaal/MRIToolKit) with the order of spherical harmonics set to $L_{max} = 8$. The FOD peaks were estimated with minimum peak amplitude threshold at 0.01. Additionally, the tensor model (DT) was fit to estimate the first eigenvector direction and used to compare to seminal works, such as McNab et al. [150].

5.2.2 Experiments

The primary and somatosensory cortical regions are known to have differing structures reflected in both cyto- and myeloarchitecture differences between M1 and S1 brain regions [155]. Therefore, we designed experiments that highlight whether state-of-the-art diffusion models are capable of reflecting the aforementioned variations as well as whether the reconstructed fiber pathways are in accordance with the myeloarchitecture of S1, M1 regions. In order to analyze if the models reflect the laminar structure of GM three equidistant surfaces between the WM-GM interface and the GM-CSF interface were built using FreeSurfer (Figure 5.1), as done by McNab et al. [150, 156].
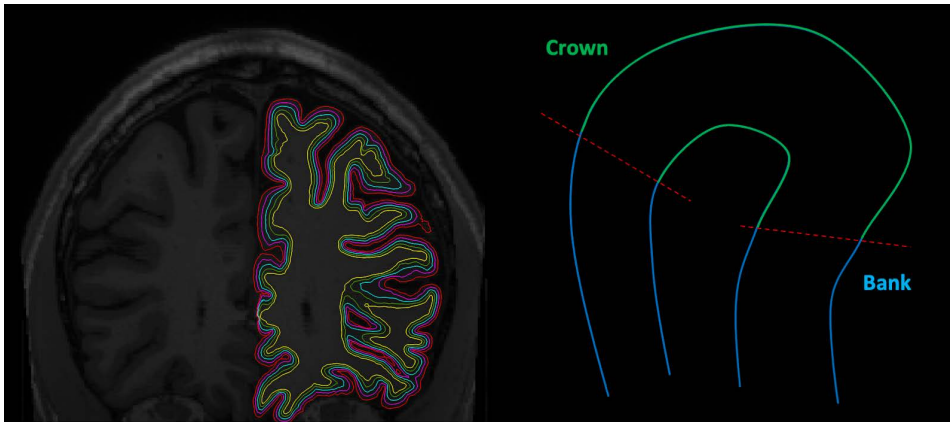

Figure 5.1: Left: three equidistant intermediate surfaces were generated using FreeSurfer between the WM-GM interface and the pial surface for laminar structure investigation. Right: crowns and banks were segmented in the surfaces based on the curvature-based criteria: $c < -0.15$ for crowns and $|c| < 0.15$ for banks (where c is a curvature value).

Surface-based FOD analysis

First of all, to compare our results to the existing results on DT models [150] the deviation between the surface orientation and the orientations of the dominant FOD peaks was estimated at each surface vertex. More specifically, the deviation between the normal to each surface vertex and the peak orientation of the FOD in the vertex was calculated, using the radiality index $r = \frac{\langle \vec{p}, \vec{n} \rangle}{|\vec{p}|}$, where $\vec{p}$ – peak vector, $\vec{n}$ – vertex normal [150, 151]. In this work we focused mainly on the first FOD peaks, the peaks with the highest amplitude.

As McNab et al. [150] report a difference in diffusion radiality pattern between bank and crown parts of the cortical folds (Figure 5.1), we similarly segment the

same regions of the cortical surfaces to perform more specific analysis. Banks and crowns were segmented based on curvature of the WM surface with crown points having a curvature of $c < -0.15$ and banks: $|c| < 0.15$ [150], where c is a curvature value. The segmentation was then extended to the other four surfaces.

Surface-based tractography analysis

Fiber tractography reconstruction was performed to investigate how the aforementioned models reflect intracortical structure of the brain. FOD-based deterministic streamline tractography [25] was performed in ExploreDTI. Reconstruction was performed solely in the GM including both seeding and propagation. Seeds were placed uniformly throughout the GM of the cropped brain segment. The angular deviation threshold was set to $30°$. The propagation step size was $0.3mm$. The minimum FOD peak amplitude was set to 0.1.

Given a large number of pathways populating a relatively small volume, we clustered the reconstructed pathways based on their length and explored the groups separately. The clustering thresholds were chosen based on pathway length distributions over all the reconstructions.

In order to investigate whether the reconstructed fiber pathways tend to be arranged into layers inside the cortex, the deviation of the pathways from the surfaces was computed. For each pathway point, the closest surface mesh vertex was found and the radial index was computed using the normal of the vertex and the propagation direction from the pathway point. This also allows exploring a relation between the length of the streamline and its deviation from the surfaces. Additionally, for same purpose, tractography reconstruction was qualitatively assessed by rendering length-based pathway clusters colored according to the radial index along the streamlines.

To provide additional insight into obtained fiber reconstructions, connectivity matrices were computed by counting the number of streamlines connecting pairs of intermediate surfaces per pathway cluster. According to our hypothesis, the connectivity matrices may reflect laminar organization by showing connectivity patterns either between remote or close intermediate surfaces.

5.3   Results

Surface-based FOD analysis

The relation between surface orientation and the dominant diffusion orientation (dominant FOD peak) was generally consistent across all models, as can be seen in Figures 5.2, 5.3. In both S1 and M1, crowns appear to contain mainly radially oriented peaks. In the banks, the WM surface and the first intermediate surface contain a considerable number of tangentially aligned peaks. Additionally, S1

appears to contain a higher ratio of tangentially oriented peaks compared to M1, which is especially visible in the banks. This changes only in the vicinity of the GM surface (Table 5.1, Figure 5.2). The SD models all revealed a higher presence of radially oriented peaks compared to tensor models.

Cortex area	Surface	Banks			Crowns		
		CSD	MS CSD	mFOD	CSD	MS CSD	mFOD
S1	WM	0.21 ± 0.24	0.2 ± 0.22	0.19 ± 0.21	0.53 ± 0.35	0.56 ± 0.33	0.55 ± 0.33
	Surface 1	0.47 ± 0.4	0.46 ± 0.39	0.43 ± 0.38	0.75 ± 0.32	0.77 ± 0.3	0.74 ± 0.32
	Surface 2	0.75 ± 0.34	0.76 ± 0.34	0.73 ± 0.34	0.85 ± 0.27	0.87 ± 0.25	0.84 ± 0.26
	Surface 3	0.83 ± 0.27	0.84 ± 0.27	0.81 ± 0.27	0.85 ± 0.27	0.89 ± 0.21	0.85 ± 0.26
	GM	0.75 ± 0.3	0.58 ± 0.36	0.73 ± 0.31	0.67 ± 0.33	0.72 ± 0.32	0.69 ± 0.32
M1	WM	0.3 ± 0.31	0.28 ± 0.29	0.29 ± 0.29	0.65 ± 0.33	0.61 ± 0.33	0.62 ± 0.34
	Surface 1	0.6 ± 0.4	0.59 ± 0.39	0.58 ± 0.39	0.84 ± 0.25	0.82 ± 0.25	0.81 ± 0.27
	Surface 2	0.83 ± 0.28	0.84 ± 0.27	0.81 ± 0.28	0.93 ± 0.15	0.91 ± 0.17	0.87 ± 0.22
	Surface 3	0.84 ± 0.28	0.84 ± 0.25	0.78 ± 0.29	0.85 ± 0.24	0.85 ± 0.26	0.81 ± 0.3
	GM	0.62 ± 0.37	0.77 ± 0.3	0.55 ± 0.36	0.54 ± 0.39	0.58 ± 0.37	0.52 ± 0.37

Table 5.1: Statistics (mean $\pm$ standard deviation) of radiality index between the surface and the first peak of SD-based FOD computed per surface as well as cortical and folding area. S1 is mainly characterized by lower mean radiality compared to M1 which does not always hold in shallower surfaces: Surface 3 and GM surface.

Surface-based tractography analysis

Based on the distributions (Figure 5.4) of the pathway lengths it was chosen to set the top-length threshold for the first cluster at $6mm$ which separates a group of pathways with the most common fiber length. The group of fiber pathways longer than $6mm$ was clustered into two more groups to separate the approximate tail of the fiber-length distribution. The second threshold was set at $12mm$.

The connectivity matrices of the surfaces based on the performed tractography are given in Figure 5.5. Longer pathways ($\geq 6mm$) appear to connect either the same surfaces or the adjacent ones (e.g. surface 3 to surfaces 2 and 4). This, in combination with lower deviations along the pathways (Figure 5.6), may indicate that the longer pathways are lying rather tangentially to the intermediate surfaces and, consequently, WM-GM interface. The group of short pathways ($< 6mm$), on the other hand, presents two different patterns depending on whether they are located in S1 or M1. The short pathways in M1 appear to primarily connect distant surfaces (e.g. WM surface 1 to surface 3). That also corresponds to pathways intersecting intermediate cortical surfaces at higher deviation angles (Figure 5.6). Conversely, the shortest pathways in S1 do not exhibit a clear dominance of pathways connecting neighboring or distant surfaces.

Moreover, the connectivity matrices of the longer-pathway groups in S1 exhibit strong connections between three intermediate surfaces showing that pathways are primarily starting and ending next to the same intermediate surfaces with slight deviation. A similar pattern can be observed in the M1 area. However, in S1 the
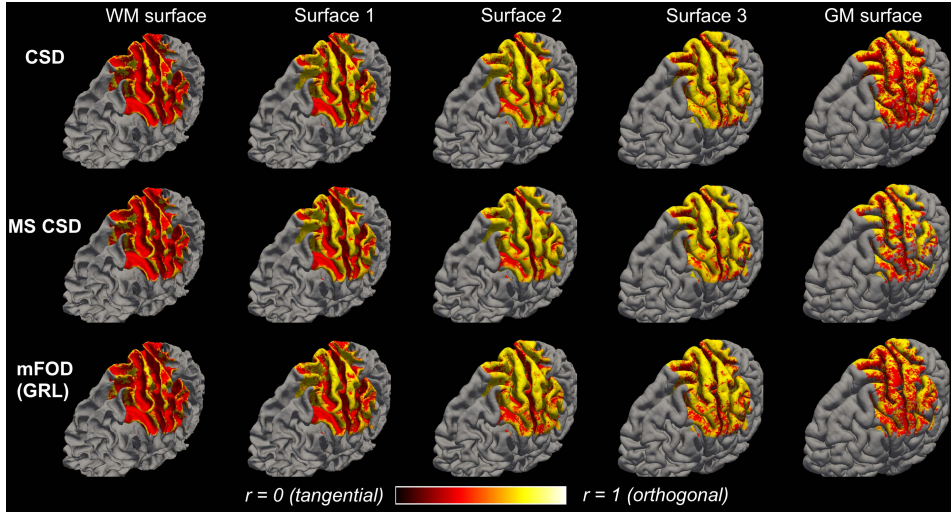
Figure 5.2: Projections of the radiality index r calculated using the first FOD peak in relation to each of the surfaces for CSD-, MS CSD-based FODs and mFODs. The more orthogonal the peak direction is to the surface, the closer the color is to white. It can be seen that the banks of the sulci are mainly characterized by tangentially oriented peaks (especially close to the WM surface). In the crowns, on the other hand, the first FOD peaks are primarily oriented orthogonally, which slightly changes in the GM surface.

number of such pathways is relatively higher, while more distant connections are relatively less common than in M1.

Pathways shorter than $6mm$ represent $\sim$83% (502079 pathways) of the CSD-based reconstruction, $\sim$87% (201849 pathways) of the MS CSD-based and $\sim$86% (389891 pathways) of the mFOD-based reconstructions. The group of length between 6 and $12mm$ constitutes $\sim$15% (92552 pathways), $\sim$11% (25838 pathways) and $\sim$13% (56914 pathways) in case of using CSD, MS CSD and mFOD respectively. Lastly, the group of the pathways longer than $12mm$ constitute $\sim$2% (CSD: 10768, MS CSD: 4509, mFOD: 7575 pathways).

5.4   Discussion

In this study we investigated the applicability of SD models to unravel fiber orientations and tracts within human brain GM using high-resolution in-vivo acquired dMRI with the focus on the motor cortex. For the purpose of localized analysis, the cortex was divided by three intermediate surfaces equidistantly spaced between white-matter and pial surface. Analysis of the diffusion orientations on the
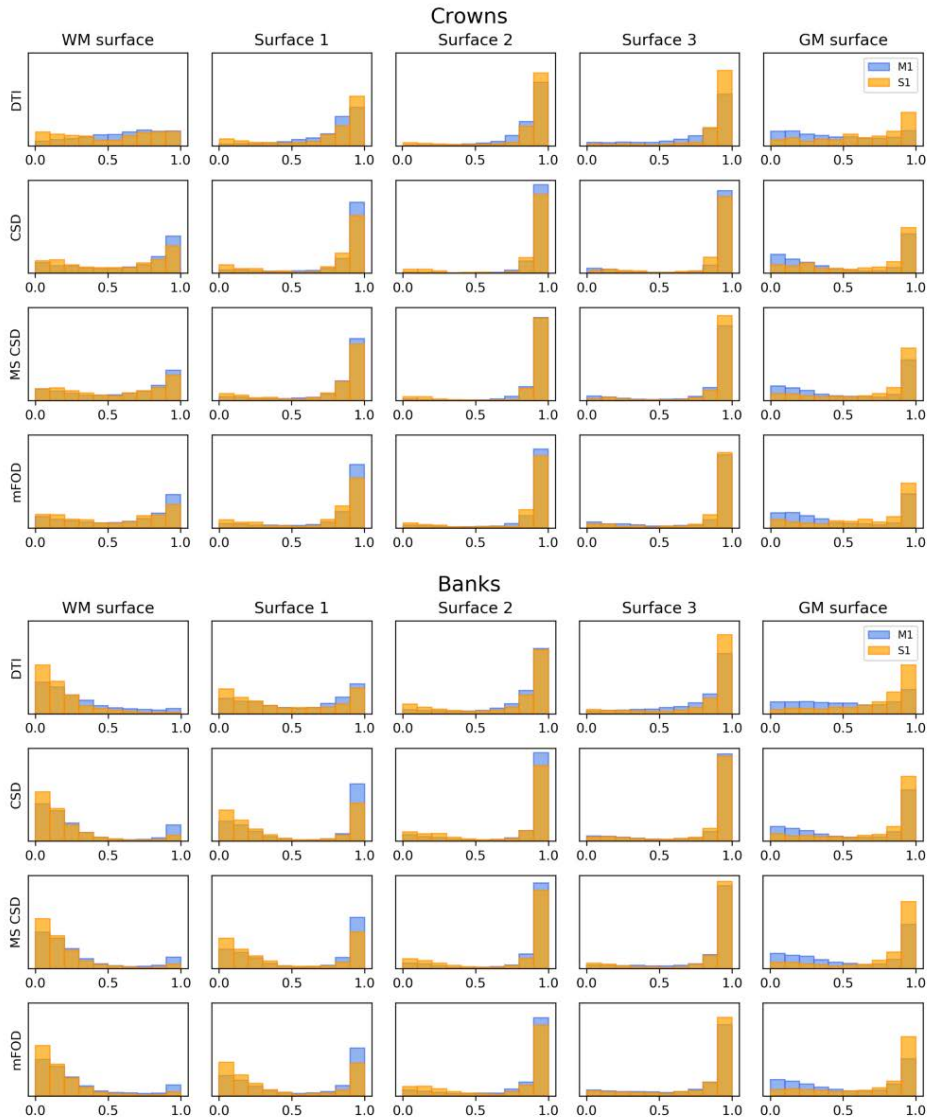
Figure 5.3: Distributions of the radiality index between the surface orientation and first peak/eigenvector at the corresponding surface vertex in the brain in S1 (orange) and M1 (blue) using the radiality coefficient (horizontal axis). For both areas dominant diffusion orientations in the crowns of the cortex appear to be more radially oriented to the surfaces, while in the banks tangential behavior is more pronounced close to WM surface. Although in both M1 and S1 the ratio of radial peaks is high, the S1 region is characterized by higher number of points with diffusion close to tangential.
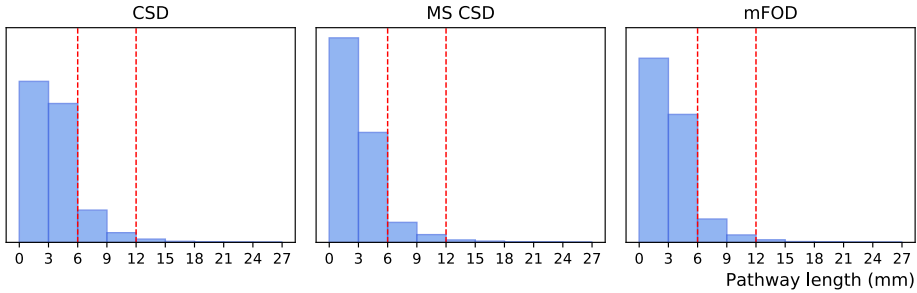
Figure 5.4: Normalized density distributions of the pathway lengths of the CSD-, MS CSD- and mFOD-based reconstructions. The first threshold was set at $6mm$ to separate the peak of the distribution. The second threshold was set at $12mm$ in order to approximate the tail of the distribution.
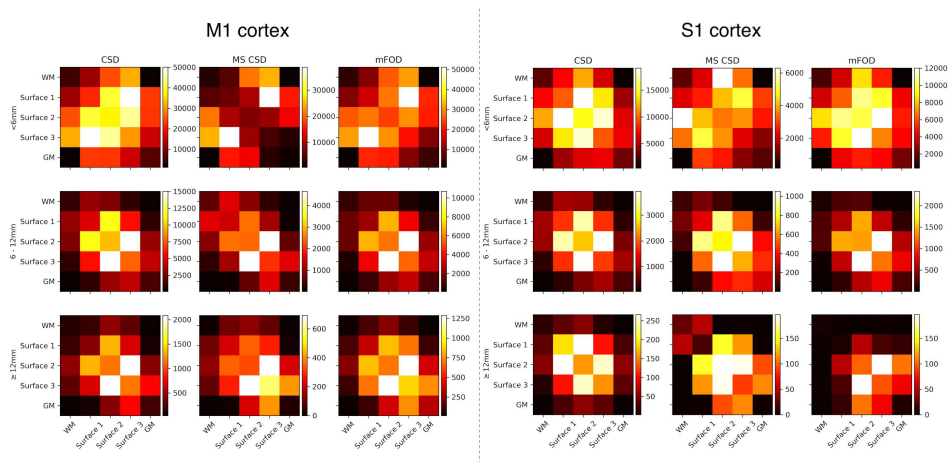

Figure 5.5: Inter-surface connectivity matrices in M1 and S1 areas for each model and tract group showing number of pathways connecting each pair of the surfaces. In M1 the shortest tract cluster reveals a dominance of remote connections, travelling across multiple layers; while in S1 the group of the shortest tracts does not show a specific consistent pattern across the models. The other two groups of tracts are characterized by pathways connecting relatively close layers in both cortical areas. However, S1 is characterized by a more specific pattern of pathways connecting same surfaces with only slight deviations. This may signal of higher tangentiality. Surfaces 1, 2 and 3 in the figure indicate intermediate surfaces.

surfaces were shown to be consistent with known patterns of the cortical structure. Performed tractography reconstruction also showed the ability of the employed SD
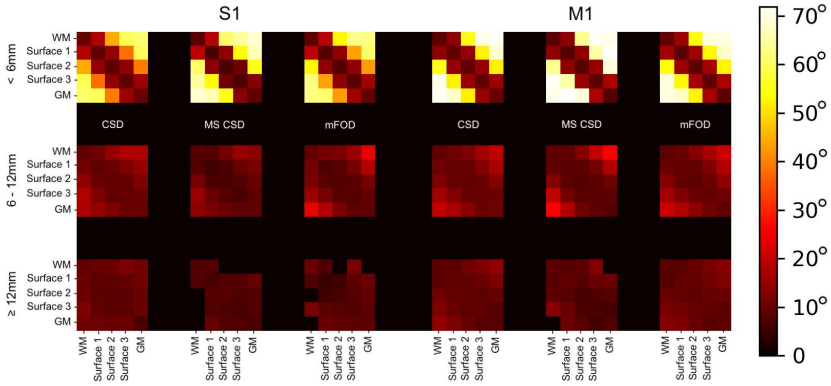
Figure 5.6: Mean pathway-to-surface deviation (in degrees) per fiber pathway group connecting a pair of surfaces showing general orientation of the pathway in the cortex. The deviations in primary motor cortex are clearly higher for the shortest pathway cluster compared to those in somatosensory cortex. The highest mean deviation is observed in pathways connecting the first and the third intermediate surfaces. Surfaces 1, 2 and 3 in the figure indicate intermediate surfaces.

models to adequately reflect cortical neuroarchitectural patterns, such as higher tangentiality in S1 area compared to M1.

A comparison of the radiality indices and peak directions obtained with different deconvolution models suggests they overall perform similarly to each other on cortical regions as well as on folding areas (Figures 5.2 and 5.3). The dominant orientations in the banks are primarily tangential in the deep cortex, while the FODs in the crown appear to have a dominant orientation with high radiality against the cortical surface. These observations are in agreement with the results of McNab et al. [150], which is also shown by including the first eigen vector of the diffusion tensor as was done by McNab et al. Additionally, the percentage of points with more tangential orientations is higher in S1 in most cases. This may reflect the known presence of tangential myelination in the S1 region, while M1 also consists of higher number of radially oriented nerve fibers [155].

The FOD orientation patterns that we observed also are in line with a previous report of Aggarwal et al. [152] using CSD-based FODs. The specimens used in their study show a mixture of orthogonal and tangential directions close to the WM surface, while radiality increases when moving into the middle of the cortex. Similar to their results, the superficial cortex is characterized by an increased tangentiality (Table 5.1).

While at FOD level all the models demonstrated comparable behavior, connectivity patterns derived from tractography appear to be quite different (Figure

5.5). CSD-based results appear the most sensitive of the techniques, as it includes a higher number of pathways compared to other approaches and the results seem nosier given large number of short pathways, while MS CSD-based reconstruction is rather specific, containing fewer and seemingly more organized pathways, and mFOD-based ones seemed to fit in the middle: less specific and more sensitive than MS CSD and also less sensitive and more specific than CSD (Figure 5.7). While the absolute number of pathways is significantly different, each of the length-based fiber clusters is similarly represented in the reconstructions. Comparable ratios of the pathway numbers allow free choice of the model in case of statistical analysis. For instance, tract length maps could be constructed similar to cortical tract length maps analyzed by Bajada et al. [157].
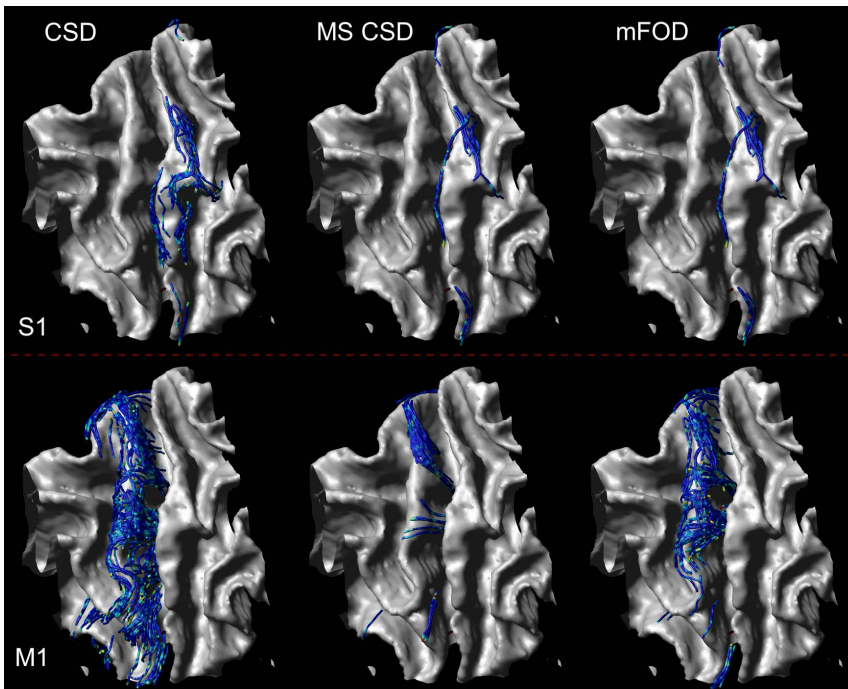

Figure 5.7: Fiber pathways reconstructed using CSD (left), MS CSD (middle) and mFOD (right) techniques connecting the intermediate Surface 2. CSD-based tractography appears to produce the most populated fiber reconstruction, while MS CSD-based results happen to be more specific. The mFOD-based reconstruction, in that regard, falls between the other two approaches.

Despite differences in connectivity patterns, general orientation of the reconstructed pathways in relation to the cortex was also shown to be consistent (Figure 5.6). In both S1 and M1 the shortest pathways connecting most distant surfaces exhibit the highest mean deviation, which suggests consistent radiality of their

orientation against the cortex. At the same time, the longer pathways are considerably more tangential, not exceeding 30° deviation.

The cause for the difference in the numbers of reconstructed streamlines probably lies in the way the response function is estimated by each of the methods. CSD estimates the response function in WM voxels, and therefore it might not accurately capture the diffusivity profile of GM, which is remarkably different [120]. MS CSD also estimates a single response function but does take into account additional compartments for GM and corticospinal fluid, attenuating their confounding effect on the FOD. Finally, mFOD combines a WM-specific and a GM-specific response functions establishing what fits best on a per voxel basis. Consequently, when the WM-based response function is deemed best, it leads to higher number of strong peaks in FOD, followed by an increased number of fiber pathways. Nevertheless, establishing which method provides the most accurate reconstructions remains an open question for future research.

We see two potential directions of research. First, tractography in this paper was performed with a rather low angular threshold (30°). While that is a common setting for WM fiber tractography in lower resolution data (compared to the one used in this work), higher resolution data might require a higher threshold. This might reveal a change in the fiber length distributions as well as in connectivity patterns.

Second, further analysis could focus on exploring whether laminar surfaces (or at least patches) could be estimated from the dMRI data. The surface probability index [158] could be used for that purpose coupled with either CSD or mFOD techniques for FOD estimation as their higher sensitivity will have a better chance of revealing intracortical layers.

5.5 Conclusions

In this work we explored the feasibility of the use of the state-of-the-art SD diffusion models in the gray matter. All the SD methods were shown to reflect the expected diffusion orientation patterns in crown and bank sulci as well as the differences between S1 and M1 cortical areas. Fibers tangentially oriented to the WM-GM interface could be reconstructed using each of the models. Additionally, analysis of the intracortical connectivity revealed variance between reconstructions based on different SD models, which may be a subject of further investigation.

CHAPTER 6

Discussion

In this thesis we presented a new tractography algorithm that addresses the issue of fiber branching and high-angular deviations. While this thesis focused on deterministic tractography, our concepts can as well be generalized and implemented in a probabilistic fashion (Chapter 2). We further explored whether the proposed method has translational potential by performing a clinical evaluation on subjects with motor-eloquent high-grade glioma. The evaluation was performed by relying on neuroanatomical knowledge of an experienced neuroradiologist (Chapter 3) as well as using functional data acquired with nTMS (Chapter 4). Finally, we ventured beyond the white matter to analyze gray matter structure, investigating whether tractography based on state-of-the-art diffusion models is capable of reflecting the laminar structure of certain cortical areas (Chapter 5).

When aiming at clinical application, robustness of the solution should always be one of the primary goals. It may be achieved by reducing the uncertainty of the solution results. If we think about the possible sources of uncertainty in fiber tractography, a relevant source is the fact that the tractography algorithm itself is essentially a heuristic procedure that does not necessarily provide a completely accurate result.

The wide range of proposed algorithms includes both "traditional" streamline-propagation algorithms [3], algorithms performing global optimization [49] as well as algorithms making use of deep learning techniques [59, 159]. Each of these paradigms has its own advantages. Thus, streamline-propagation algorithms allow localized reconstructions. Global tractography takes into account the complete signal of the brain but may not be locally accurate. The deep-learning algorithms seem especially promising in cases of dMRI acquisitions with low spatial and angular resolution, as they may compensate for the lack of precision in the FOD estimation. However, they may require the training dataset to be representative of the target population on which the model is going to be used. It is clear that while each of the algorithms is capable of producing results that are to some extent plausible, there is no guarantee that it is completely accurate.

With that in mind the developed multi-level fiber tractography algorithm was presented in deterministic implementation of the individual pathways. This

supposedly reduces the total uncertainty of the results while the algorithm achieves a bundle reconstruction extent comparable to probabilistic approaches. However, we also propose an implementation that allows extending the concept behind the algorithm with probabilistic direction sampling. The algorithm was also shown to be capable of preserving bundle topography, which may be an important when reconstructing fibers corresponding to a very specific function [27].

As none of the existing algorithms are completely free of false-positve results, the post-processing approaches become even more relevant. An example hereof is the COMMIT framework [160, 161] that is capable of automatically filtering out false streamlines from a whole-brain tractography reconstruction based on diffusion signal modelling. However, such filtering algorithms are not applicable to bundle-specific reconstructions without first performing whole-brain tractography. Thus, to have control over the false-positive rate MLFT relies on the prior neuroanatomical knowledge.

Another important source of uncertainty is the model used to estimate the FOD. Being dependent on a response function properly reflecting tissue properties, FODs are already limited in their precision. And what seems to limit them even more is the interpretation of the FOD and FOD peaks. Peaks are commonly considered to represent independent fibers. However, it is known that actual nerve fibers do branch out, and that branching occurs rather often [20]. MLFT addresses this aspect by iteratively expanding the reconstruction by following FOD peaks with a higher deviation and including those that lead to plausible pathways, which was shown to achieve an adequate extent of the bundle reconstructions.

Most tractography algorithms are presented on cohorts of healthy subjects. There are also cases when tractography is performed on ex-vivo data with histological ground truth [162]. However, there is still a lack of validation of the results obtained in-vivo on clinical subjects. Being part of a consortium focused on "clinical translation", it was only natural for us to make an attempt of bringing our development closer to the clinics. In collaboration with Klinikum rechts der Isar in Munich, we have performed tractography on a cohort of patients with motor-eloquent high-grade glioma comparing routinely used DTI-based tractography with CSD-based and multi-level tractography algorithms. All the results were validated by an experienced neuroradiologist by checking that the bundles pass through the known anatomical landmarks. However, when it comes to tracking nerves in tumor patients, multiple complications arise. In certain cases edema may lead to a dramatic signal loss that would not allow tracking fibers through the affected area. It must be noted, that in such cases the absence of pathways in fiber tractography results does not imply by itself that the corresponding sub-bundle is not functional. Another complication may be caused by the mass effect when the tumor growth leads to a considerable shift of the brain tissues. In such cases, the question is whether the nerves were compressed or whether they were infiltrated by the tumor.

Such complex cases are difficult to validate solely relying on neuroanatomical

knowledge of the experts. Thus, we have also performed evaluation on the sub-cohort that was exposed to nTMS motor mapping. We could observe a difference between the tractography algorithms, although the study was limited by the fact that nTMS is primarily used to map extremities: legs, arms, hands. The proposed algorithm has shown its ability to cover larger part of the motor mapping mask compared to more conventional deterministic approaches.

It should be considered that nTMS has a certain precision limit as the stimulation is not applied to a single point but rather to an area around the target location. This may lead to an inclusion of pathways that perhaps have less contribution to the registered nTMS response. To alleviate this limitation, the ability to reconstruct pathways in gray matter could be helpful as it would potentially provide more precise localization of nTMS activations. With this in mind, we performed an explorative project on the applicability of the number of spherical deconvolution methods for tractography in gray matter.

In order to avoid quality-of-life degradation, it is important to differentiate nerve fibers that are still active. While nTMS is a nice tool to create a reference for such purpose, in many cases clinical protocols do not include nTMS mapping or it may not be performed for some patients based on the decision of a neuroradiologist or a neurosurgeron. Thus, it is of interest whether the pathways that are descending from activation areas have certain micro-structural properties that would allow discovering them without stimulations. Prior research has shown very clear differences between nTMS-based reconstructions in healthy and diseased hemispheres [163]. Perhaps, one of the future ways to extend those findings would be comparing micro-structural properties of nTMS-based against nonTMS-based reconstructions in the diseased hemisphere. This would allow obtaining a similar reference as provided by nTMS in cases when patients should not or cannot be subjected to brain stimulations.

However, current routine acquisition protocols will immediately run into a complication with performing such a study as most of them are producing single-shell diffusion-weighted images, while modern tractography methods required to extract micro-structural properties rely on at least two-shell data. The limited quality of the acquisition protocols used in clinical practice is one of the bottlenecks that also what prevent advanced tractography algorithms from being adopted into clinical practice. One of the potential solutions could be to synthesize additional shells using, for instance, deep learning. A number of studies have been published by the time of writing this chapter that proposed solutions based on convolutional neural networks [164–166].

The validation of tractography in presence of tumors may be complicated by the mass effect or edema. One of the future directions to solve this challenge could be the use of tumor growth modeling that not only models the volume of the tumor or the direction of its growth but also includes modelling of the tumor-induced tissue deformation. Assuming there is a fiber-bundle atlas of a healthy brain, it can then be deformed based on the estimated deformation of the tissues.

Given the deformed fiber bundles, potentially a decision would be made on the plausibility of the reconstructions in the occluded or compressed brain areas. Such hypothesis could either be more specifically verified by pre-operative functional data, for instance, nTMS, or by direct electrical stimulation intra-operatively. Most importantly, it would provide an additional signaling mechanism that makes surgery planning more effective.

We started this work mentioning the importance of a proper robust surgical planning procedure. Although at this stage the evaluation of the proposed methodology is incomplete, we can already state that it shows enough promising results to be potentially included in surgical planning. With the TMS-based evaluation we have shown that the MLFT

To conclude, there are still many challenges to pursue in the fields of tractography and neurosurgery planning. In this work we contributed to both fields by proposing an algorithm that suggests an unconventional interpretation of fiber orientation distribution, adding translational aspect by algorithm evaluation on clinical data as well as bringing gray matter into the surgery planning spotlight as potential contributor to solving existing limitations.

Bibliography

[1] A. M. Molinaro, S. Hervey-Jumper, R. A. Morshed, J. Young, et al., "Association of maximal extent of resection of contrast-enhanced and non–contrast-enhanced tumor with survival within molecular subgroups of patients with newly diagnosed glioblastoma," JAMA Oncology, vol. 6, no. 4, pp. 495–503, 2020.

[2] M. Ammirati, N. Vick, Y. Liao, I. M. Ciric, and M. Mikhael, "Effect of the extent of surgical resection on survival and quality of life in patients with supratentorial glioblastomas and anaplastic astrocytomas," Neurosurgery, vol. 22, no. 2, pp. 201–206, 1987.

[3] B. Jeurissen, M. Descoteaux, S. Mori, and A. Leemans, "Diffusion MRI fiber tractography of the brain," NMR in Biomedicine, vol. 32, no. 4, p. e3785, 2019. e3785 NBM-17-0045.R2.

[4] N. Sollmann, N. Wildschuetz, A. Kelm, N. Conway, et al., "Associations between clinical outcome and navigated transcranial magnetic stimulation characteristics in patients with motor-eloquent brain lesions: a combined navigated transcranial magnetic stimulation–diffusion tensor imaging fiber tracking approach," Journal of Neurosurgery JNS, vol. 128, no. 3, pp. 800 – 810, 2018.

[5] S. Farquharson, J.-D. Tournier, F. Calamante, G. Fabinyi, et al., "White matter fiber tractography: why we need to move beyond DTI," Journal of Neurosurgery, vol. 118, no. 6, pp. 1367–1377, 2013.

[6] K. H. Maier-Hein, P. F. Neher, J.-C. Houde, M.-A. Côté, et al., "The challenge of mapping the human connectome based on diffusion tractography," Nature Communications, vol. 8, no. 1, p. 1349, 2017.

[7] K. G. Schilling, C. M. W. Tax, F. Rheault, B. A. Landman, et al., "Prevalence of white matter pathways coming into a single white matter voxel orientation: The bottleneck issue in tractography," Human Brain Mapping, vol. 43, no. 4, pp. 1196–1213, 2022.

[8] A. Fornito, A. Zalesky, and M. Breakspear, "Graph analysis of the human connectome: Promise, progress, and pitfalls," NeuroImage, vol. 80, pp. 426–444, 2013.

[9] P. Hagmann, M. Kurant, X. Gigandet, P. Thiran, et al., "Mapping human whole-brain structural networks with diffusion MRI," PLoS ONE, vol. 2, no. 7, p. e597, 2007.

[10] M. Catani and M. Thiebaut de Schotten, "A diffusion tensor imaging tractography atlas for virtual in vivo dissections," Cortex, vol. 44, no. 8, pp. 1105–1132, 2008.

[11] T. Jacquesson, F. Cotton, A. Attyé, S. Zaouche, et al., "Probabilistic tractography to predict the position of cranial nerves displaced by skull base tumors: Value for surgical strategy through a case series of 62 patients," Neurosurgery, vol. 0, no. 0, pp. 1–12, 2018.

[12] S. S. Panesar, K. Abhinav, F.-C. Yeh, T. Jacquesson, et al., "Tractography for surgical neuro-oncology planning: Towards a gold standard," Neurotherapeutics, vol. 16, no. 1, pp. 36–51, 2019.

[13] M. Thiebaut de Schotten, D. H. Ffytche, A. Bizzi, F. Dell'Acqua, et al., "Atlasing location, asymmetry and inter-subject variability of white matter tracts in the human brain with MR diffusion tractography," NeuroImage, vol. 54, no. 1, pp. 49–59, 2011.

[14] C. A. Clark and T. Byrnes, "DTI and Tractography in Neurosurgical Planning," in Diffusion MRI: Theory, Methods, and Applications, Oxford University Press, 2010.

[15] J. D. Costabile, E. Alaswad, S. D'Souza, J. A. Thompson, and D. R. Ormond, "Current applications of diffusion tensor imaging and tractography in intracranial tumor resection.," Frontiers in oncology, vol. 9, p. 426, 2019.

[16] S. L. Hervey-Jumper and M. S. Berger, "Evidence for improving outcome through extent of resection," Neurosurgery Clinics of North America, vol. 30, no. 1, pp. 85–93, 2019. Low-Grade Glioma.

[17] K. G. Schilling, A. Daducci, K. Maier-Hein, C. Poupon, et al., "Challenges in diffusion MRI tractography – Lessons learned from international benchmark competitions," Magnetic Resonance Imaging, vol. 57, pp. 194–209, 2019.

[18] T. Sarwar, K. Ramamohanarao, and A. Zalesky, "Mapping connectomes with diffusion MRI: deterministic or probabilistic tractography?," Magnetic Resonance in Medicine, vol. 81, no. 2, pp. 1368–1384, 2019.

[19] C. Weiss, I. Tursunova, V. Neuschmelting, H. Lockau, et al., "Improved nTMS- and DTI-derived CST tractography through anatomical ROI seeding on anterior pontine level compared to internal capsule," NeuroImage: Clinical, vol. 7, pp. 424 – 437, 2015.

[20] F. Mortazavi, A. L. Oblak, W. Z. Morrison, J. D. Schmahmann, et al., "Geometric navigation of axons in a cerebral pathway: Comparing dMRI with tract tracing and immunohistochemistry.," Cerebral cortex (New York, N.Y. : 1991), vol. 28, no. 4, pp. 1219–1232, 2018.

[21] J.-D. Tournier, F. Calamante, and A. Connelly, "Robust determination of the fibre orientation distribution in diffusion MRI: Non-negativity constrained super-resolved spherical deconvolution," NeuroImage, vol. 35, no. 4, pp. 1459–1472, 2007.

[22] F. Guo, A. Leemans, M. A. Viergever, F. Dell'Acqua, and A. De Luca, "Generalized Richardson-Lucy (GRL) for analyzing multi-shell diffusion MRI data," NeuroImage, vol. 218, p. 116948, 2020.

[23] F. Dell'Acqua, G. Rizzo, P. Scifo, R. A. Clarke, et al., "A model-based deconvolution approach to solve fiber crossing in diffusion-weighted MR imaging," IEEE Transactions on Biomedical Engineering, vol. 54, no. 3, pp. 462–472, 2007.

[24] S. Mori, B. J. Crain, V. P. Chacko, and P. C. M. Van Zijl, "Three-dimensional tracking of axonal projections in the brain by magnetic resonance imaging," Annals of Neurology, vol. 45, no. 2, pp. 265–269, 1999.

[25] B. Jeurissen, A. Leemans, D. K. Jones, J.-D. Tournier, and J. Sijbers, "Probabilistic fiber tracking using the residual bootstrap with constrained spherical deconvolution," Human Brain Mapping, vol. 32, no. 3, pp. 461–479, 2011.

[26] J.-D. Tournier, F. Calamante, and A. Connelly, "MRtrix: Diffusion tractography in crossing fiber regions," International Journal of Imaging Systems and Technology, vol. 22, no. 1, pp. 53–66, 2012.

[27] D. Aydogan and Y. Shi, "Tracking and validation techniques for topographically organized tractography," NeuroImage, vol. 181, no. 1, pp. 64–84, 2018.

[28] G. H. Patel, D. M. Kaplan, and L. H. Snyder, "Topographic organization in the brain: searching for general principles," Trends in cognitive sciences, vol. 18, no. 7, pp. 351–363, 2014.

[29] J. Ruben, J. Schwiemann, M. Deuchert, R. Meyer, et al., "Somatotopic Organization of Human Secondary Somatosensory Cortex," Cerebral Cortex, vol. 11, no. 5, pp. 463–473, 2001.

[30] D. Lee, D. Lee, and B. Han, "Topographic organization of motor fibre tracts in the human brain: findings in multiple locations using magnetic resonance diffusion tensor tractography," European Radiology, vol. 26, no. 6, pp. 1751–1759, 2016.

[31] M. J. Arcaro, M. A. Pinsk, and S. Kastner, "The anatomical and functional organization of the human visual pulvinar," Journal of Neuroscience, vol. 35, no. 27, pp. 9848–9871, 2015.

[32] P. Fillard, M. Descoteaux, A. Goh, S. Gouttard, et al., "Quantitative evaluation of 10 tractography algorithms on a realistic diffusion MR phantom," NeuroImage, vol. 56, no. 1, pp. 220–234, 2011.

[33] B. S. Han, J. H. Hong, C. Hong, S. S. Yeo, et al., "Location of the corticospinal tract at the corona radiata in human brain," Brain Research, vol. 1326, pp. 75 – 80, 2010.

[34] D. Wassermann, N. Makris, Y. Rathi, M. Shenton, et al., "The white matter query language: a novel approach for describing human white matter anatomy," Brain Structure and Function, vol. 221, no. 9, pp. 4705–4721, 2016.

[35] M. Chamberland, B. Scherrer, S. P. Prabhu, J. Madsen, et al., "Active delineation of Meyer's loop using oriented priors through MAGNEtic tractography (MAGNET)," Human Brain Mapping, vol. 38, no. 1, pp. 509–527, 2017.

[36] C. Negwer, N. Sollmann, S. Ille, T. Hauck, et al., "Language pathway tracking: comparing nTMS-based DTI fiber tracking with a cubic ROIs-based protocol," Journal of Neurosurgery, vol. 126, no. 3, pp. 1006–1014, 2017.

[37] M. Descoteaux, R. Deriche, T. R. Knösche, and A. Anwander, "Deterministic and probabilistic tractography based on complex fibre orientation distributions," IEEE Transactions on Medical Imaging, vol. 28, no. 2, pp. 269–286, 2009.

[38] J.-D. Tournier, S. Mori, and A. Leemans, "Diffusion tensor imaging and beyond," Magnetic Resonance in Medicine, vol. 65, no. 6, pp. 1532–1556, 2011.

[39] A. Leemans, B. Jeurissen, J. Sijbers, and D. K. Jones, "ExploreDTI: a graphical toolbox for processing, analyzing, and visualizing diffusion MR data.," 17th Annual Meeting of International Society of Mag Reson Med, p. 3537, 2009.

[40] M. Froeling, C. M. Tax, S. B. Vos, P. R. Luijten, and A. Leemans, ""MASSIVE" brain dataset: Multiple acquisitions for standardization of structural imaging validation and evaluation," Magnetic Resonance in Medicine, vol. 77, no. 5, pp. 1797–1809, 2017.

[41] S. B. Vos, C. M. W. Tax, P. R. Luijten, S. Ourselin, et al., "The importance of correcting for signal drift in diffusion MRI," Magnetic Resonance in Medicine, vol. 77, no. 1, pp. 285–299, 2017.

[42] A. Leemans and D. K. Jones, "The B-matrix must be rotated when correcting for subject motion in DTI data," Magnetic Resonance in Medicine, vol. 61, no. 6, pp. 1336–1349, 2009.

[43] B. Jeurissen, J.-D. Tournier, T. Dhollander, A. Connelly, and J. Sijbers, "Multi-tissue constrained spherical deconvolution for improved analysis of multi-shell diffusion MRI data," NeuroImage, vol. 103, pp. 411–426, 2014.

[44] R. S. Desikan, F. Ségonne, B. Fischl, B. T. Quinn, et al., "An automated labeling system for subdividing the human cerebral cortex on MRI scans into gyral based regions of interest," NeuroImage, vol. 31, no. 3, pp. 968–980, 2006.

[45] B. Fischl, A. van der Kouwe, C. Destrieux, E. Halgren, et al., "Automatically parcellating the human cerebral cortex," Cerebral Cortex, vol. 14, no. 1, pp. 11–22, 2004.

[46] B. Fischl, "FreeSurfer," NeuroImage, vol. 62, pp. 774–781, 2012.

[47] J.-D. Tournier, F. Calamante, and A. Connelly, "Improved probabilistic streamlines tractography by 2nd order integration over fiber orientation distributions.," 18th Annual Meeting of International Society of Mag Reson Med, p. 1670, 2010.

[48] J.-D. Tournier, R. Smith, D. Raffelt, R. Tabbara, et al., "MRtrix3: A fast, flexible and open software framework for medical image processing and visualisation," NeuroImage, vol. 202, p. 116137, 2019.

[49] D. Christiaens, M. Reisert, T. Dhollander, S. Sunaert, et al., "Global tractography of multi-shell diffusion-weighted imaging data using a multi-tissue model," NeuroImage, vol. 123, pp. 89 – 101, 2015.

[50] M. Patestas and L. P. Gartner, A Textbook of Neuroanatomy. Blackwell Publishing Ltd, 2006.

[51] D. B. Aydogan and Y. Shi, "Topography preserving tractography for mapping human brain pathways," 25th Annual Meeting of International Society of Mag Reson Med, p. 0059, 2017.

[52] E. Visser, E. H. Nijhuis, J. K. Buitelaar, and M. P. Zwiers, "Partition-based mass clustering of tractography streamlines," NeuroImage, vol. 54, no. 1, pp. 303–312, 2011.

[53] E. Garyfallidis, M. Brett, M. M. Correia, G. B. Williams, and I. Nimmo-Smith, "QuickBundles, a method for tractography simplification.," Frontiers in neuroscience, vol. 6, p. 175, 2012.

[54] D. D. O'Leary and T. Terashima, "Cortical axons branch to multiple subcortical targets by interstitial axon budding: Implications for target recognition and "waiting periods"," Neuron, vol. 1, no. 10, pp. 901–910, 1988.

[55] D. Fortin, C. Aubin-Lemay, A. Bore, G. Girard, et al., "Tractography in the study of the human brain: a neurosurgical perspective," Canadian Journal of Neurological Sciences, vol. 39, no. 6, pp. 747–756, 2012.

[56] V. J. Wedeen, D. L. Rosene, R. Wang, G. Dai, et al., "The geometric structure of the brain fiber pathways.," Science (New York, N.Y.), vol. 335, no. 6076, pp. 1628–34, 2012.

[57] U. Ebeling and H. Reulen, "Subcortical topography and proportions of the pyramidal tract," Acta Neurochirurgica, vol. 118, no. 3-4, pp. 164–171, 1992.

[58] S. F. Witelson, "Hand and sex differences in the isthmus and genu of the human corpus callosum. A postmortem morphological study," Brain: a journal of neurology, vol. 112, no. 3, pp. 799–835, 1989.

[59] J. Wasserthal, P. Neher, and K. H. Maier-Hein, "TractSeg - fast and accurate white matter tract segmentation," NeuroImage, vol. 183, pp. 239–253, 2018.

[60] W. Krieg, "Connections of the frontal cortex of the monkey," Charles C Thomas Springfield, 1955.

[61] R. E. Smith, J.-D. Tournier, F. Calamante, and A. Connelly, "SIFT2: Enabling dense quantitative assessment of brain white matter connectivity using streamlines tractography," NeuroImage, vol. 119, pp. 338–351, 2015.

[62] Q. T. Ostrom, L. Bauchet, F. G. Davis, I. Deltour, et al., "The epidemiology of glioma in adults: A state of the science review," Neuro-Oncology, vol. 16, pp. 896–913, 2014.

[63] Q. T. Ostrom, D. J. Cote, M. Ascha, C. Kruchko, and J. S. Barnholtz-Sloan, "Adult glioma incidence and survival by race or ethnicity in the united states from 2000 to 2014," JAMA Oncology, vol. 4, pp. 1254–1262, 2018.

[64] P. Y. Wen and S. Kesari, "Malignant gliomas in adults," New England Journal of Medicine, vol. 359, no. 5, pp. 492–507, 2008.

[65] Q. T. Ostrom, G. Cioffi, H. Gittleman, N. Patil, et al., "CBTRUS statistical report: Primary brain and other central nervous system tumors diagnosed in the united states in 2012-2016," Neuro-Oncology, vol. 21, pp. V1–V100, 2019.

[66] A. Claes, A. J. Idema, and P. Wesseling, "Diffuse glioma growth: A guerilla war," Acta Neuropathologica, vol. 114, no. 5, pp. 443–458, 2007.

[67] M. Martínez-Garcia, J. Álvarez Linera, C. Carrato, L. Ley, et al., "SEOM clinical guidelines for diagnosis and treatment of glioblastoma," Clinical and Translational Oncology, vol. 20, pp. 22–28, 2018.

[68] R. Stupp, W. P. Mason, M. J. van den Bent, M. Weller, et al., "Radiotherapy plus concomitant and adjuvant temozolomide for glioblastoma," New England Journal of Medicine, vol. 352, pp. 987–996, 2005.

[69] N. Sanai and M. S. Berger, "Surgical oncology for gliomas: The state of the art," Nature Reviews Clinical Oncology, vol. 15, pp. 112–125, 2018.

[70] Y. Wang and T. Jiang, "Understanding high grade glioma: Molecular mechanism, therapy and comprehensive management," Cancer Letters, vol. 331, pp. 139–146, 2013.

[71] M. N. Khan, A. M. Sharma, M. Pitz, S. K. Loewen, et al., "High-grade glioma management and response assessment-recent advances and current challenges," Current Oncology, vol. 23, no. 4, pp. e383–e391, 2016.

[72] P. D. Brown, M. J. Maurer, T. A. Rummans, B. E. Pollock, et al., "A prospective study of quality of life in adults with newly diagnosed high-grade gliomas: The impact of the extent of resection on quality of life and survival," Neurosurgery, vol. 57, pp. 495–503, 2005.

[73] A. Haj, C. Doenitz, K.-M. Schebesch, D. Ehrensberger, et al., "Extent of resection in newly diagnosed glioblastoma: Impact of a specialized neuro-oncology care center," Brain Sciences, vol. 8, no. 1, p. 5, 2017.

[74] M. Lacroix, D. Abi-Said, D. R. Fourney, Z. L. Gokaslan, et al., "A multivariate analysis of 416 patients with glioblastoma multiforme: Prognosis, extent of resection, and survival," Journal of Neurosurgery, vol. 95, pp. 190–198, 2001.

[75] O. Bloch, S. J. Han, S. Cha, M. Z. Sun, et al., "Impact of extent of resection for recurrent glioblastoma on overall survival: Clinical article," Journal of Neurosurgery, vol. 117, no. 6, pp. 1032 – 1038, 2012.

[76] H. Duffau and E. Mandonnet, "The "onco-functional balance" in surgery for diffuse low-grade glioma: Integrating the extent of resection with quality of life," Acta Neurochirurgica, vol. 155, pp. 951–957, 2013.

[77] N. A. O. Bush, S. M. Chang, and M. S. Berger, "Current and future strategies for treatment of glioma," Neurosurgical Review, vol. 40, 2017.

[78] N. Sanai and M. S. Berger, "Intraoperative stimulation techniques for functional pathway preservation and glioma resection," Neurosurgical Focus, vol. 28, 2010.

[79] P. C. De Witt Hamer, S. G. Robles, A. H. Zwinderman, H. Duffau, and M. S. Berger, "Impact of intraoperative stimulation brain mapping on glioma surgery outcome: A meta-analysis," Journal of Clinical Oncology, vol. 30, no. 20, pp. 2559–2565, 2012.

[80] S. L. Hervey-Jumper and M. S. Berger, "Maximizing safe resection of low- and high-grade glioma," Journal of Neuro-Oncology, vol. 130, pp. 269–282, 2016.

[81] J. E. Villanueva-Meyer, M. C. Mabray, and S. Cha, "Current clinical brain tumor imaging," Clinical Neurosurgery, vol. 81, pp. 397–415, 2017.

[82] G. Shukla, G. S. Alexander, S. Bakas, R. Nikam, et al., "Advanced magnetic resonance imaging in glioblastoma: a review," Chinese Clinical Oncology, vol. 6, no. 4, p. 40, 2017.

[83] W. B. Overcast, C. Y. Davis, Korbin M. Ho, G. D. Hutchins, M. A. Green, et al., "Advanced imaging techniques for neuro-oncologic tumor diagnosis, with an emphasis on PET-MRI imaging of malignant brain tumors," Current Oncology Reports, vol. 23, no. 3, p. 34, 2021.

[84] M. Smits, "MRI biomarkers in neuro-oncology," Nature Reviews Neurology, vol. 17, pp. 486–500, 2021.

[85] Y. Assaf and O. Pasternak, "Diffusion tensor imaging (DTI)-based white matter mapping in brain research: A review," Journal of Molecular Neuroscience, vol. 34, no. 1, pp. 51–61, 2008.

[86] J. L. Ulmer, A. P. Klein, W. M. Mueller, E. A. DeYoe, and L. P. Mark, "Preoperative diffusion tensor imaging: Improving neurosurgical outcomes in brain tumor patients," Neuroimaging Clinics of North America, vol. 24, no. 4, pp. 599–617, 2014. Clinical Applications of Functional MRI.

[87] J. L. Ulmer, C. V. Salvan, W. M. Mueller, H. G. Krouwer, et al., "The role of diffusion tensor imaging in establishing the proximity of tumor borders to functional brain systems: Implications for preoperative risk assessments and postoperative outcomes," Technology in Cancer Research & Treatment, vol. 3, no. 6, pp. 567–576, 2004.

[88] P. Basser, J. Mattiello, and D. LeBihan, "MR diffusion tensor spectroscopy and imaging," Biophysical Journal, vol. 66, no. 1, pp. 259–267, 1994.

[89] K. G. Abdullah, D. Lubelski, P. G. P. Nucifora, and S. Brem, "Use of diffusion tensor imaging in glioma resection," Neurosurgical Focus FOC, vol. 34, no. 4, p. E1, 2013.

[90] C. Nimsky, "Fiber tracking—a reliable tool for neurosurgery?," World Neurosurgery, vol. 74, no. 1, pp. 105–106, 2010.

[91] H. Duffau, "Diffusion tensor imaging is a research and educational tool, but not yet a clinical tool," World Neurosurgery, vol. 82, pp. e43–e45, 2014.

[92] A. R. Potgieser, M. Wagemakers, A. L. van Hulzen, B. M. de Jong, et al., "The role of diffusion tensor imaging in brain tumor surgery: A review of the literature," Clinical Neurology and Neurosurgery, vol. 124, pp. 51–58, 2014.

[93] D. Becker, M. Scherer, P. Neher, C. Jungk, et al., "Going beyond diffusion tensor imaging tractography in eloquent glioma surgery–high-resolution fiber tractography: Q-Ball or constrained spherical deconvolution?," World Neurosurgery, vol. 134, pp. e596–e609, 2020.

[94] T. E. Behrens, H. J. Berg, S. Jbabdi, M. F. Rushworth, and M. W. Woolrich, "Probabilistic diffusion tractography with multiple fibre orientations: What can we gain?," NeuroImage, vol. 34, pp. 144–155, 2007.

[95] B. Jeurissen, A. Leemans, J. D. Tournier, D. K. Jones, and J. Sijbers, "Investigating the prevalence of complex fiber configurations in white matter tissue with diffusion magnetic resonance imaging," Human Brain Mapping, vol. 34, pp. 2747–2766, 2013.

[96] J. Jensen, J. Helpern, A. Ramani, H. Lu, and K. Kyle, "Diffusional kurtosis imaging: The quantification of non-Gaussian water diffusion by means of magnetic resonance imaging," Magnetic Resonance in Medicine, vol. 53, no. 6, pp. 1432–1440, 2005.

[97] E. Mormina, M. Longo, A. Arrigo, C. Alafaci, et al., "MRI tractography of corticospinal tract and arcuate fasciculus in high-grade gliomas performed by constrained spherical deconvolution: Qualitative and quantitative analysis," American Journal of Neuroradiology, vol. 36, no. 10, pp. 1853–1858, 2015.

[98] Z. Sheng, J. Yu, Z. Chen, Y. Sun, et al., "Constrained-spherical deconvolution tractography in the evaluation of the corticospinal tract in glioma surgery," Frontiers in Surgery, vol. 8, 2021.

[99] E. Mormina, A. Arrigo, A. Calamuneri, C. Alafaci, et al., "Optic radiations evaluation in patients affected by high-grade gliomas: a side-by-side constrained spherical deconvolution and diffusion tensor imaging study," Neuroradiology, vol. 58, no. 11, pp. 1067–1075, 2016.

[100] A. M. Radwan, L. Emsell, J. Blommaert, A. Zhylka, et al., "Virtual brain grafting: Enabling whole brain parcellation in the presence of large lesions," NeuroImage, vol. 229, 2021.

[101] F. Kofler, C. Berger, D. Waldmannstetter, J. Lipkova, et al., "BraTS toolkit: Translating BraTS brain tumor segmentation algorithms into clinical and scientific practice," Frontiers in Neuroscience, vol. 14, 2020.

[102] B. H. Menze, A. Jakab, S. Bauer, J. Kalpathy-Cramer, et al., "The multimodal brain tumor image segmentation benchmark (BRATS)," IEEE Transactions on Medical Imaging, vol. 34, pp. 1993–2024, 2015.

[103] C. M. Tax, B. Jeurissen, S. B. Vos, M. A. Viergever, and A. Leemans, "Recursive calibration of the fiber response function for spherical deconvolution of diffusion MRI data," NeuroImage, vol. 86, pp. 67–80, 2014.

[104] B. J. Jellison, A. S. Field, J. Medow, M. Lazar, et al., "Diffusion tensor imaging of cerebral white matter: A pictorial review of physics, fiber tract anatomy, and tumor imaging patterns," American Journal of Neuroradiology, vol. 25, no. 3, pp. 356–369, 2004.

[105] P. Virtanen, R. Gommers, T. E. Oliphant, M. Haberland, et al., "SciPy 1.0: fundamental algorithms for scientific computing in python," Nature Methods, vol. 17, no. 3, pp. 261–272, 2020.

[106] D. S. Tuch, "Q-ball imaging," Magnetic Resonance in Medicine, vol. 52, no. 6, pp. 1358–1372, 2004.

[107] M. Bucci, M. L. Mandelli, J. I. Berman, B. Amirbekian, et al., "Quantifying diffusion MRI tractography of the corticospinal tract in brain tumors with deterministic and probabilistic methods," NeuroImage: Clinical, vol. 3, pp. 361–368, 2013.

[108] J.-D. Tournier, F. Calamante, D. G. Gadian, and A. Connelly, "Direct estimation of the fiber orientation density function from diffusion-weighted MRI data using spherical deconvolution," NeuroImage, vol. 23, no. 3, pp. 1176–1185, 2004.

[109] T. E. Conturo, N. F. Lori, T. S. Cull, E. Akbudak, et al., "Tracking neuronal fiber pathways in the living human brain," Proceedings of the National Academy of Sciences, vol. 96, no. 18, pp. 10422–10427, 1999.

[110] M. Guye, G. J. Parker, M. Symms, P. Boulby, et al., "Combined functional MRI and tractography to demonstrate the connectivity of the human primary motor cortex in vivo," NeuroImage, vol. 19, no. 4, pp. 1349–1360, 2003.

[111] P. Staempfli, C. Reischauer, T. Jaermann, A. Valavanis, et al., "Combining fMRI and DTI: A framework for exploring the limits of fMRI-guided DTI fiber tracking and for verifying DTI-based fiber tractography results," NeuroImage, vol. 39, no. 1, pp. 119–126, 2008.

[112] N. Sollmann, H. Zhang, A. Fratini, N. Wildschuetz, et al., "Risk assessment by presurgical tractography using navigated TMS maps in patients with highly motor-or language-eloquent brain tumors," Cancers, vol. 12, 2020.

[113] D. Frey, V. Strack, E. Wiener, D. Jussen, et al., "A new approach for corticospinal tract reconstruction based on navigated transcranial stimulation and standardized fractional anisotropy values," NeuroImage, vol. 62, pp. 1600–1609, 2012.

[114] S. M. Krieg, N. H. Buchmann, J. Gempt, E. Shiban, et al., "Diffusion tensor imaging fiber tracking using navigated brain stimulation - a feasibility study," Acta Neurochirurgica, vol. 154, pp. 555–563, 2012.

[115] C. Weiss Lucas, I. Tursunova, V. Neuschmelting, C. Nettekoven, et al., "Functional MRI vs. navigated TMS to optimize M1 seed volume delineation for DTI tractography. A prospective study in patients with brain tumours adjacent to the corticospinal tract," NeuroImage: Clinical, vol. 13, pp. 297–309, 2017.

[116] N. Sollmann, B. Meyer, and S. M. Krieg, "Implementing functional preoperative mapping in the clinical routine of a neurosurgical department: Technical note," World Neurosurgery, vol. 103, pp. 94–105, 2017.

[117] N. Sollmann, A. Fratini, H. Zhang, C. Zimmer, et al., "Associations between clinical outcome and tractography based on navigated transcranial magnetic stimulation in patients with language-eloquent brain lesions," Journal of Neurosurgery, vol. 132, no. 4, pp. 1033 – 1042, 2019.

[118] N. Sollmann, C. Negwer, S. Ille, S. Maurer, et al., "Feasibility of nTMS-based DTI fiber tracking of language pathways in neurosurgical patients using a fractional anisotropy threshold," Journal of Neuroscience Methods, vol. 267, pp. 45–54, 2016.

[119] G. Raffa, I. Bährend, H. Schneider, K. Faust, et al., "A novel technique for region and linguistic specific nTMS-based DTI fiber tracking of language pathways in brain tumor patients," Frontiers in Neuroscience, vol. 10, 2016.

[120] A. D. Luca, F. Guo, M. Froeling, and A. Leemans, "Spherical deconvolution with tissue-specific response functions and multi-shell diffusion MRI to estimate multiple fiber orientation distributions (mFODs)," NeuroImage, vol. 222, 2020.

[121] S. Tourbier, Y. Aleman-Gomez, A. Griffa, M. Bach Cuadra, and P. Hagmann, "Multi-scale brain parcellator: a BIDS app for the lausanne connectome parcellation.," 25th Annual Meeting of the Organization for Human Brain Mapping, p. W616, 2019.

[122] K. D. Miller, Q. T. Ostrom, C. Kruchko, N. Patil, et al., "Brain and other central nervous system tumor statistics, 2021," CA: A Cancer Journal for Clinicians, vol. 71, pp. 381–406, 2021.

[123] A. Stadlbauer, C. Nimsky, R. Buslei, E. Salomonowitz, et al., "Diffusion tensor imaging and optimized fiber tracking in glioma patients: Histopathologic evaluation of tumor-invaded white matter structures," NeuroImage, vol. 34, pp. 949–956, 2007.

[124] L. Bello, A. Gambini, A. Castellano, G. Carrabba, et al., "Motor and language DTI fiber tracking combined with intraoperative subcortical mapping for surgical removal of gliomas," NeuroImage, vol. 39, pp. 369–382, 2008.

[125] L. R. Carrete, J. S. Young, and S. Cha, "Advanced imaging techniques for newly diagnosed and recurrent gliomas," Frontiers in Neuroscience, vol. 16, 2022.

[126] F. Henderson, K. G. Abdullah, R. Verma, and S. Brem, "Tractography and the connectome in neurosurgical treatment of gliomas: The premise, the progress, and the potential," Neurosurgical Focus, vol. 48, p. E6, 2020.

[127] F. C. Yeh, A. Irimia, D. C. de Almeida Bastos, and A. J. Golby, "Tractography methods and findings in brain tumors and traumatic brain injury," NeuroImage, vol. 245, 2021.

[128] T. D. Azad and H. Duffau, "Limitations of functional neuroimaging for patient selection and surgical planning in glioma surgery," Neurosurgical Focus, vol. 48, p. E12, 2020.

[129] J. Ruohonen and J. Karhu, "Navigated transcranial magnetic stimulation," Neurophysiologie Clinique, vol. 40, pp. 7–17, 2010.

[130] N. Sollmann, S. M. Krieg, L. Säisänen, and P. Julkunen, "Mapping of motor function with neuronavigated transcranial magnetic stimulation: A review on clinical application in brain tumors and methods for ensuring feasible accuracy," Brain Sciences, vol. 11, 2021.

[131] J. P. Lefaucheur and T. Picht, "The value of preoperative functional cortical mapping using navigated tms," Neurophysiologie Clinique, vol. 46, pp. 125–133, 2016.

[132] A. F. Haddad, J. S. Young, M. S. Berger, and P. E. Tarapore, "Preoperative applications of navigated transcranial magnetic stimulation," Frontiers in Neurology, vol. 11, p. 1950, 2021.

[133] M.-T. Forster, E. Hattingen, C. Senft, T. Gasser, et al., "Navigated transcranial magnetic stimulation and functional magnetic resonance imaging: Advanced adjuncts in preoperative planning for central region tumors," Neurosurgery, vol. 68, no. 5, pp. 1317–1325, 2011.

[134] S. M. Krieg, E. Shiban, N. Buchmann, J. Gempt, et al., "Utility of presurgical navigated transcranial magnetic brain stimulation for the resection of tumors in eloquent motor areas: Clinical article," Journal of Neurosurgery, vol. 116, pp. 994–1001, 2012.

[135] P. E. Tarapore, M. C. Tate, A. M. Findlay, S. M. Honma, et al., "Preoperative multimodal motor mapping: A comparison of magnetoencephalography imaging, navigated transcranial magnetic stimulation, and direct cortical stimulation: Clinical article," Journal of Neurosurgery, vol. 117, pp. 354–362, 2012.

[136] T. Rosenstock, U. Grittner, G. Acker, V. Schwarzer, et al., "Risk stratification in motor area-related glioma surgery based on navigated transcranial magnetic stimulation data," Journal of Neurosurgery, vol. 126, pp. 1227–1237, 2017.

[137] A. Conti, G. Raffa, F. Granata, V. Rizzo, et al., "Navigated transcranial magnetic stimulation for "somatotopic" tractography of the corticospinal tract," Operative Neurosurgery, vol. 10, pp. 542–554, 2014.

[138] S. M. Krieg, P. Lioumis, J. P. Mäkelä, J. Wilenius, et al., "Protocol for motor and language mapping by navigated TMS in patients and healthy volunteers; workshop report," Acta Neurochirurgica, vol. 159, pp. 1187–1195, 2017.

[139] L. Säisänen, P. Julkunen, E. Niskanen, N. Danner, et al., "Motor potentials evoked by navigated transcranial magnetic stimulation in healthy subjects," Journal of Clinical Neurophysiology, vol. 25, pp. 367–372, 2008.

[140] N. Sollmann, L. Bulubas, N. Tanigawa, C. Zimmer, et al., "The variability of motor evoked potential latencies in neurosurgical motor mapping by preoperative navigated transcranial magnetic stimulation," BMC Neuroscience, vol. 18, 2017.

[141] S. Mohammadi, H. E. Möller, H. Kugel, D. K. Müller, and M. Deppe, "Correcting eddy current and motion effects by affine whole-brain registrations: Evaluation of three-dimensional distortions and comparison with slicewise correction," Magnetic Resonance in Medicine, vol. 64, pp. 1047–1056, 2010.

[142] D. G. Southwell, S. L. Hervey-Jumper, D. W. Perry, and M. S. Berger, "Intraoperative mapping during repeat awake craniotomy reveals the functional plasticity of adult cortex," Journal of Neurosurgery, vol. 124, pp. 1460–1469, 2016.

[143] N. Conway, N. Wildschuetz, T. Moser, L. Bulubas, et al., "Cortical plasticity of motor-eloquent areas measured by navigated transcranial magnetic stimulation in patients with glioma," Journal of Neurosurgery, vol. 127, pp. 981–991, 2017.

[144] W. R. Gibb, N. W. Kong, and M. C. Tate, "Direct evidence of plasticity within human primary motor and somatosensory cortices of patients with glioblastoma," Neural Plasticity, vol. 2020, 2020.

[145] D. C. Van Essen, S. Jbabdi, S. N. Sotiropoulos, C. Chen, et al., "Mapping connections in humans and non-human primates: Aspirations and challenges for diffusion imaging," in Diffusion MRI (Second Edition) (H. Johansen-Berg and T. E. Behrens, eds.), pp. 337–358, San Diego: Academic Press, 2nd ed., 2014.

[146] C. Reveley, A. K. Seth, C. Pierpaoli, A. C. Silva, et al., "Superficial white matter fiber systems impede detection of long-range cortical connections in Diffusion MR tractography," Proceedings of the National Academy of Sciences, vol. 112, no. 21, pp. E2820–E2828, 2015.

[147] L. Cloutman and M. Lambon Ralph, "Connectivity-based structural and functional parcellation of the human cortex using diffusion imaging and tractography," Frontiers in Neuroanatomy, vol. 6, 2012.

[148] M. Han, G. Yang, H. Li, S. Zhou, et al., "Individualized Cortical Parcellation Based on Diffusion MRI Tractography," Cerebral Cortex, vol. 30, no. 5, pp. 3198–3208, 2020.

[149] R. Klaver, H. E. D. Vries, G. J. Schenk, and J. J. Geurts, "Grey matter damage in multiple sclerosis," Prion, vol. 7, no. 1, pp. 66–75, 2013.

[150] J. A. McNab, J. R. Polimeni, R. Wang, J. C. Augustinack, et al., "Surface based analysis of diffusion orientation for identifying architectonic domains in the in vivo human cortex," NeuroImage, vol. 69, pp. 87–100, 2013.

[151] A. Anwander, A. Pampel, and T. R. Knösche, "In vivo measurement of cortical anisotropy by diffusion-weighted imaging correlates with cortex type," 18th Annual Meeting of International Society of Mag Reson Med, p. 109, 2010.

[152] M. Aggarwal, D. W. Nauen, J. C. Troncoso, and S. Mori, "Probing region-specific microstructure of human cortical areas using high angular and spatial resolution diffusion MRI," NeuroImage, vol. 105, pp. 198–207, 2015.

[153] C. W. Leuze, A. Anwander, P.-L. Bazin, B. Dhital, et al., "Layer-Specific Intracortical Connectivity Revealed with Diffusion MRI," Cerebral Cortex, vol. 24, no. 2, pp. 328–339, 2012.

[154] F. Wang, Z. Dong, Q. Tian, C. Liao, et al., "In vivo human whole-brain Connectom diffusion MRI dataset at 760 μm isotropic resolution," Scientific Data, vol. 8, p. 122, 2021.

[155] N. Palomero-Gallagher and K. Zilles, "Cortical layers: Cyto-, myelo-, receptor- and synaptic architecture in human cortical areas," NeuroImage, vol. 197, pp. 716–741, 2019.

[156] A. M. Dale, B. Fischl, and M. I. Sereno, "Cortical Surface-Based Analysis: I. Segmentation and Surface Reconstruction," NeuroImage, vol. 9, no. 2, pp. 179–194, 1999.

[157] C. J. Bajada, J. Schreiber, and S. Caspers, "Fiber length profiling: A novel approach to structural brain organization," NeuroImage, vol. 186, pp. 164–173, 2019.

[158] C. M. Tax, T. Dela Haije, A. Fuster, C.-F. Westin, et al., "Sheet Probability Index (SPI): Characterizing the geometrical organization of the white matter with diffusion MRI," NeuroImage, vol. 142, pp. 260–279, 2016.

[159] F. Rheault, E. St-Onge, J. Sidhu, K. Maier-Hein, et al., "Bundle-specific tractography with incorporated anatomical and orientational priors," NeuroImage, vol. 186, pp. 382–398, 2019.

[160] S. Schiavi, M. Ocampo-Pineda, M. Barakovic, L. Petit, et al., "A new method for accurate in vivo mapping of human brain connections using microstructural and anatomical information," Science Advances, vol. 6, no. 31, p. eaba8245, 2020.

[161] M. Ocampo-Pineda, S. Schiavi, F. Rheault, G. Girard, et al., "Hierarchical microstructure informed tractography," Brain Connectivity, vol. 11, no. 2, pp. 75–88, 2021.

[162] C. Maffei, C. Lee, M. Planich, M. Ramprasad, et al., "Using diffusion MRI data acquired with ultra-high gradient strength to improve tractography in routine-quality data," NeuroImage, vol. 245, p. 118706, 2021.

[163] L. S. Fekonja, Z. Wang, D. B. Aydogan, T. Roine, et al., "Detecting corticospinal tract impairment in tumor patients with fiber density and tensor-based metrics," Frontiers in Oncology, vol. 10, 2021.

[164] M. Ren, H. Kim, N. Dey, and G. Gerig, "Q-space conditioned translation networks for directional synthesis of diffusion weighted images from multi-modal structural MRI," in Medical Image Computing and Computer Assisted Intervention – MICCAI 2021, (Cham), pp. 530–540, Springer International Publishing, 2021.

[165] R. R. Jha, G. Jaswal, A. Bhavsar, and A. Nigam, "Single-shell to multi-shell dMRI transformation using spatial and volumetric multilevel hierarchical reconstruction framework," Magnetic Resonance Imaging, vol. 87, pp. 133–156, 2022.

[166] R. R. Jha, B. R. Kumar, S. K. Pathak, W. Schneider, et al., "Undersampled single-shell to MSMT fODF reconstruction using CNN-based ODE solver," Computer Methods and Programs in Biomedicine, vol. 230, p. 107339, 2023.

About the author

Andrey Zhylka was born on September 28, 1993, in Minsk, Belarus. In 2011 he entered Belarusian State University (BSU), where he studied at the Faculty of Applied Mathematics and Computer Science (FAMCS), Department of Discrete Mathematics and Algorithmics. There Andrey received a degree of a Specialist in Mathematics and System Programming with honors as well as Master of Physical and Mathematical Sciences in 2017. During his studies Andrey visited Jena University Hospital working on intravascular OCT video segmentation, which was a start of his journey in image analysis. Andrey also contributed to ScaffoldHunter, open-source project maintained by TU Dortmund, implementing data visualization algorithms. In 2014, Andrey started his career as Software Engineer first in "CompatibL" working on client system integration. In 2016, he moved to a position of R&D Software Engineer in Garage department of "Epam Systems". Projects included a wide range of computer vision and signal analysis tasks, including tasks for self-driving car, child face detection, EEG signal analysis. There Andrey was promoted to Senior R&D Software Engineer in 2018. Between autumn 2016 and spring 2018, Andrey also worked as teaching assistant at BSU FAMCS, teaching discrete mathematics and image processing. From May 2018, Andrey was a PhD student at Medical Image Analysis group of Eindhoven University of Technology as a member of TRABIT consortium funded by European Union's Horizon 2020 research and innovation program under the Marie Sklodowska-Curie grant (765148). There he has been working on fiber tractography in Diffusion MRI supervised by Prof. Josien Pluim and Prof. Marcel Breeuwer as well as Dr. Alberto De Luca and Dr. Alexander Leemans from University Medical Center Utrecht. The results of his research are presented in this thesis.

List of Publications

Journals

[J1] A. Zhylka, N. Sollmann, F. Kofler, A. Radwan, A. De Luca, J. Gempt, B. Wiestler, B. Menze, A. Schroeder, C. Zimmer, J.S. Kirschke, S. Sunaert, A. Leemans, S.M. Krieg and J. Pluim. Reconstruction of the Corticospinal Tract in Patients with Motor-Eloquent High-Grade Gliomas Using Multilevel Fiber Tractography Combined with Functional Motor Cortex Mapping. AJNR, 2023.

[J2] C. Maffei, G. Girard, K.G. Schilling, D.B. Aydogan, N. Adluru, A. Zhylka, Y. Wu, M. Mancini, A. Hamamci, A. Sarica, A. Teillac, S.H. Baete, D. Karimi, F.-C. Yeh, M.E. Yildiz, A. Gholipour, Y. Bihan-Poudec, B. Hiba, A. Quattrone, A. Quattrone, T. Boshkovski, N. Stikov, P.-T. Yap, A. de Luca, J. Pluim, A. Leemans, V. Prabhakaran, B.B. Bendlin, A.L. Alexander, B.A. Landman, E.J. Canales-Rodríguez, M. Barakovic, J. Rafael-Patino, T. Yu, G. Rensonnet, S. Schiavi, A. Daducci, M. Pizzolato, E. Fischi-Gomez, J.-P. Thiran, G. Dai, G. Grisot, N. Lazovski, S. Puch, M. Ramos, P. Rodrigues, V. Prčkovska, R. Jones, J. Lehman, S.N. Haber, A. Yendiki. Insights from the IronTract challenge: optimal methods for mapping brain pathways from multi-shell diffusion MRI. NeuroImage, 2022.

[J3] A. Zhylka, A. Leemans, J. Pluim, A. De Luca. Anatomically informed multi-level tractography for targeted virtual dissection. MAGMA, 2022

[J4] A. Zhylka, N. Sollmann, F. Kofler, A. Radwan, A. De Luca, J. Gempt, B. Wiestler, B. Menze, S.M. Krieg, C. Zimmer, J.S. Kirschke, S. Sunaert, A. Leemans and J. Pluim. Tracking the corticospinal tract in patients with brain tumors: Clinical evaluation of novel multi-level fiber tracking (MLFT) and comparison to conventional approaches. Frontiers in Oncology, 2021.

[J5] A. M. Radwan, L. Emsell, J. Blommaert, A. Zhylka, S. Kovacs, T. Theys, N. Sollmann, P. Dupont, S. Sunaert. Virtual brain grafting: Enabling whole brain parcellation in the presence of large lesions. NeuroImage, 2021.

[J6] L. Ning, E. Bonet-Carne, F. Grussu, F. Sepehrband, E. Kaden, J. Veraart, S.B. Blumberg, C. S. Khoo, M. Palombo, I. Kokkinos, D.C. Alexander, J. Coll-Font, B. Scherrer, S.K. Warfield, S.C. Karayumak, Y. Rathi, S. Koppers, L. Weninger, J. Ebert, D. Merhof, D. Moyer, M. Pietsch, D. Christiaens, R. Azeredo Gomes Teixeira, J.-D. Tournier, K.G. Schilling, Y. Huo, V. Nath, C.

Hansen, J. Blaber, B.A. Landman, A. Zhylka, J.P.W. Pluim, G. Parker, U. Rudrapatna, J. Evans, C. Charron, D.K. Jones, C.M.W. Tax. Cross-scanner and cross-protocol multi-shell diffusion MRI data harmonization: Algorithms and results. NeuroImage, 2020.

[J7] S. Otto, K. Nitsche, C. Jung, A. Kryvanos, A. Zhylka, K. Heitkamp, J.-L. Gutiérrez-Chico, B. Goebel, P.C. Schulze, H.R. Figulla, T.C. Poerner. Endothelial progenitor cells and plaque burden in stented coronary artery segments: an optical coherence tomography study six months after elective PCI. BMC Cardiovascular Disorders volume, 2017.

Conference proceedings

[C1] A. Zhylka, A. Leemans, J. Pluim, A. De Luca. Walking in the Dark: Spherical Deconvolution Methods in Cortical Gray Matter. ISMRM Diffusion MRI Workshop, 2022.

[C2] A. Zhylka, J. Pluim, F. Kofler, A. Radwan, A. De Luca, A. Schroeder, B. Wiestler, J.S. Kirschke, B. Menze, S. Sunaert, A. Leemans, S.M. Krieg, N. Sollmann. Multi-level fiber tractography in brain tumor patients using functional mapping for seeding. ISMRM, 2022.

[C3] C. Maffei, G. Girard, K.G. Schilling, D.B. Aydogan, N. Adluru, A. Zhylka, Y. Wu, M. Mancini, A. Hamamci, A. Sarica, D. Karimi, F.-C. Yeh, M.E. Yildiz, A. Gholipour, A. Quattrone, A. Quattrone, P.-T. Yap, A. De Luca, J. Pluim, A. Leemans, V. Prabhakaran, B.B. Bendlin, A.L. Alexander, B.A. Landman, E.J. Canales-Rodríguez, M. Barakovic, J. Rafael-Patino, T. Yu, G. Rensonnet, S. Schiavi, A. Daducci, M. Pizzolato, E. Fischi-Gomez, J.-P. Thiran, G. Dai, G. Grisot, S. Puch, M. Ramos, N. Lazovski, P. Rodrigues, V. Prchkovska, R. Jones, J. Lehman, S. Haber, A. Yendiki. IronTract challenge: Simple post-processing enhances the accuracy of diffusion tractography. ISMRM, 2021.

[C4] S. Shit, J.C. Paetzold, A Sekuboyina, I. Ezhov, A. Unger, A. Zhylka, J.P.W. Pluim, U. Bauer, B.H. Menze. clDice – a novel topology-preserving loss function for tubular structure segmentation. CVPR, 2021.

[C5] A. Zhylka, N. Sollmann, A. De Luca, D. Krahulec, M. Breeuwer, A. Leemans, J. Pluim. Multi-level fiber tracking: evaluation on clinical data. ISMRM, 2020.

[C6] A. Zhylka, A. Leemans, J. Pluim, A. De Luca. Anatomically informed multi-level fiber tractography for improved sensitivity of white matter bundle reconstruction in diffusion MRI. ISMRM, 2020.

[C7] A. Zhylka, A. Leemans, J. Pluim, A. De Luca. On fiber orientation distribution peak selection for diffusion MRI tractography. ESMRMB, 2019.

[C8] L. Ning, E. Bonet-Carne, F. Grussu, F. Sepehrband, E. Kaden, J. Veraart, S.B. Blumberg, C.S. Khoo, M. Palombo, J. Coll-Font, B. Scherrer, S.K. Warfield, S. C. Karayumak, Y. Rathi, S. Koppers, L. Weninger, J. Ebert, D. Merhof, D. Moyer, M. Pietsch, D. Christiaens, R. Teixeira, J.-D. Tournier, A. Zhylka, J. Pluim, G. Parker, U. Rudrapatna, J. Evans, C. Charron, D.K. Jones, C.W.M. Tax. Muti-shell Diffusion MRI Harmonisation and Enhancement Challenge (MUSHAC): Progress and Results. MICCAI, 2018.

Acknowledgements

Alright, you finally reached the end of this book and now is the time for a bit of reflection. While you could look up the lists of the co-authors of the papers that shaped this work, there are by far many more people who contributed to my life during PhD years and left either explicit or implicit footprint on how this work turned out (and I just hope I don't forget anyone).

Josien Pluim, thank you for your advice and support with all the projects and ideas whether those were related or unrelated to PhD. Thank you for always checking that I am on track and know where I am going with my research. I really appreciated all the weekly meetings that would go on regardless of how much I had to report, which, I believe, brought a great deal of discipline into my work. I hope I will once master your skill of helping me find the answer by simply asking for explanation. I am very grateful to you for being kind, caring, supportive and approachable in more personal matters.

Alberto De Luca, thank you for taking such an active role in guiding me despite not being my official co-promotor in the beginning. I really enjoyed working and discussing projects with you. I am very grateful for all your extensive and attentive feedback. Looking forward to doing even more projects together. Also, thank you very much for bringing the recipes from home for me, they are amazing and I will cherish them forever.

Alexander Leemans, thanks to you I am now always thinking about a toy example first. Additionally, thanks to your feedback and guidance my project management as well as visualization skills are by far better than they used to be. I will probably hear your voice of reason in my head whenever I am tempted to take maybe exciting to me but unreasonable way of doing experiments. I am also very grateful to you for expressing your patience and kindness when they were needed.

Marcel Breeuwer, thank you for all our talks about the future perspective and options in and outside academia and all your effort in providing insights into industrial life. On a more personal note, I really enjoyed all the lunch and non-work-related chats. I am amazed by your storytelling skills. Of course, thank you for your vocal teacher recommendation. And I still hope to hear you singing as well as make some music with you.

Professor Jean-Philippe Thiran, Doctor Remco Duits, Professor Paul Boon, thank you very much for accepting to be part of my PhD committee and assessing this work.

and squat together (I think, it was one of the first things you mentioned to me), create a rock band with Alexiy in the name and make an album as we already have a cover photo! Jokes aside, I am very happy to have you as a friend and very much grateful for all the advice and experience you shared with me. Especially, the best kibbeling location on the Tuesday market ;)

Koen Eppenhof, thank you for helping me out in the first days, weeks and months of my PhD by giving advice, sharing experience and telling jokes I wasn't always immediately sure were jokes. Also, I will never forget how you became my "girlfriend for a second" to tell me not to work at night. And yes, I will just leave it here without any further explanation.

Friso Heslinga, you are probably one of the most open-minded and empathetic people I know. Thank you for all the conversations we had whether it was about politics, policies or just personal stuff.

Suzanne Wetstein, the fittest person in the group. I was always amazed with your discipline with the meal preparation before competitions. Thank you for all the lunch- and coffee-break chats.

Maxime Lafarge, an example of how to handle things with great care whether it is work to be done or words to be spoken. I wish I asked you a bit more about the way you work.

Seb Harrevelt, I hope you will never lose your drive for hobbies and new projects. It was really nice being your neighbour when sitting in the lab, especially when we discussed MR Physics homework.

Evi Huijben, Iris Kolenbrander, Dennis van de Sande, for a short while I shared the office with each of you. I am thankful to each of you for the company and occasional banter. Evi, sorry if I annoyed you with too much talking (which was often nonsense), thank you for your patience.

Navchetan Awasthi, thank you for all the COVID-time walks and talks at TU/e campus. We should finally catch up again.

Hassan Keshvarikhojasteh, we only spent short time in the office together, but I know you love motivational quotes. Here is one for you: "Sing like no one is listening. Love like you've never been hurt. Dance like nobody is watching."

Alexander Raaimakers, Maureen van Eijnatten, Veronika Cheplygina, Pim Moeskops, thank you for all the work and non-work related chats.

Rina van Dijck-Postma, you have a heart of gold. I am extremely grateful for all your help and patience with my endless questions that started even before I arrived. I am also very much grateful for all the support I received from you. I wish you only the best in life.

Erica Jansen, Sylvia van Beek-Verschure, thank you for all the help with administrative questions and occasional chocolates.

Martijn Stoorvogel, Leanne Zikken, Luuk Jacobs, thank you for being courageous students who chose my BEP projects and pulled them off really well while it was requiring a bit of extra skill. I really enjoyed your dedication and wish you

success in your future endeavours.

As in the good old days I would still travel for the offline meetings with Alexander and Alberto (can you even imagine?), I got to meet the nice people of UMC Utrecht some of which I would like to mention here.

Szabolcs David, oh, those conversations that started by you saying: "So, tell me what you are doing..." It was nice to bounce the story against an "opponent". Although I may not have thought so by the end of those conversations, I do appreciate them. Also, thank you for always being ready with an advice on how to go around ExploreDTI or anything else really.

Samuel St-Jean, another person who would often ask me if I had questions. Thank you for advice and bringing up some very useful references.

Mike van Rijsel, Jurica Sprem, Hui Shan Chan, thank you for accepting me in your office in UMC Utrecht and thank you for all the casual chit chat and jokes. Also, thanks to Mike I did not have to suffer through the last episode of Game of Thrones on my own.

I was extremely lucky to be part of a great consortium that brought together amazing people: Athena Taymourtash, Amnah Mahroo, Carmen Moreno Genis, Daniel Krahulec, Ezequiel de la Rosa, Francesco La Rosa, Ines Meyer, Ivan Ezhov, Luca Canalini, Lucas Fidon, Thomas Yu, Stefano Cerri, Suprosanna Shit, Sveinn Pálsson. I really enjoyed all the schools and occasional meetings we had and really hope that TRABIT will have at least one more offline gathering just for the sake of it.

Unfortunately, not everything goes along a nice timely plan. Finalizing the thesis appeared to be one of those things. Therefore, Theo Ruers, Jonas Teuwen, thank you for trusting in me and giving me the position in your groups while allowing to finish the PhD. I am not sure I can imagine how much more stressful it would be to wrap up my thesis otherwise.

With NKI being my main occupation for the last year while I was also finishing the thesis, I am very thankful to have such nice colleagues in Surgical Department (Behdad, Dick, Dinusha, Cyrille, Freija, Harald, Jasper, Karin, Keowa, Laura, Leanne, Lisanne, Lisanne, Lynn, Lotte, Marijn, Mark, Mark, Matteo, Ryan, Stefan, Tiziano, Wout), AI for Oncology group (Ajey, Andreas, Eric, George, Joren, Jonatan, Luuk, Marek, Nikita, Ray, Samuele, Shannon, Vanessa, Yoni) and Radiotherapy (Bas). I should add extra layer of gratitude to Luuk, Tiziano, Matteo, Mark, Jasper and, of course, Dick, all of whom endured me talking about all the writing a bit more.

Oleksandra Ivashchenko, thank you for giving me the right advice in the right time, otherwise I would have missed a great opportunity. Also, thank you for letting me take your office spot, which is sort of still yours (the name on the door hasn't been changed). It is always nice to chat and I can only hope to have at least half of the energy and discipline you have.

Alexandra Radaeva, if not for your suggestion and help I would probably not

have been able to pursue PhD without extra trouble and delays. I am also grateful to you for being a great friend and supporting me through the years.

Diana Bocancea, thank you for recommending me the sci-diku-imageworld mailing list. If not for it I might not have found this PhD position. Also, thank you for all the chats about PhD life and life in general.

Oleksandr Tomashchuk, despite all the nice chats, walks, dinners and coding evenings, first of all I have to thank you for inviting me for your mom's varenyky. Hence, the gratitude extends to your mother as well :) But, of course, thank you for being a great friend and all the things mentioned above.

Anastasia, Andriy, Andriy, Kateryna, Nikita, Sergii, Uliana, our musical adventures were rather short but brought a lot of joy to me. I hope we gather again someday.

John en Ton van Haasteren, dank jullie voor de gezeligde tijd, drankjes in de voortuin, grapjes, muziek advies, "koekjes" dag en pannenkoekenhuis bezoeken. John, ook hartelijk dank voor uw hulp en zorg.

Найбільша можлива подяка від мене моїм батькам, Анжелі і Ігорю Жилка, і мої сестрі, Юлії Жилка. Я дуже вдячний за всю любов, турботу, підтримку і поради, які я міг отримати в любий момент, не зважаючи на відстань і час дня. І дуже вдячний батькам за то, яким ви мене виховали, що ви в мене вложили і які можливості дали. Без цього всього я би ніколи не зміг бути там, де я зараз є.

Khrystyna Faryna, I am very happy and thankful that we are together. You filled my life with energy and happiness making all the challenges dim. My life is so much brighter thanks to you.

P.S. I should probably also thank my guitars, amps and pedals for preserving my mental stability.